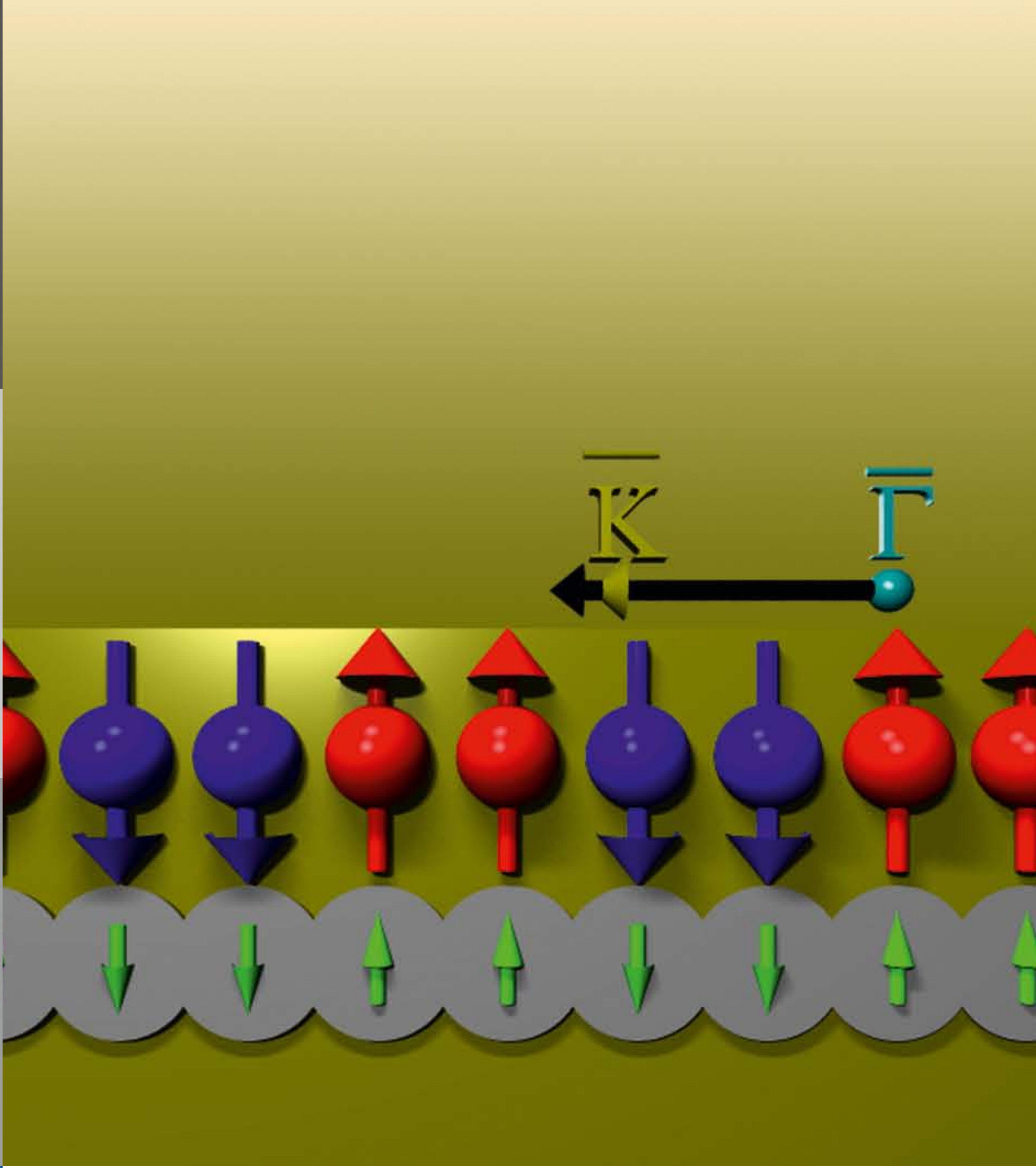

Ab *initio* investigations of magnetic properties of ultrathin transition-metal films on *4d* substrates

Ali Al-Zubi

Mitglied der Helmholtz-Gemeinschaft

JÜLICH
FORSCHUNGSZENTRUM

Schriften des Forschungszentrums Jülich
Reihe Schlüsseltechnologien / Key Technologies Band / Volume 16

Forschungszentrum Jülich GmbH
Institute for Advanced Simulation (IAS)
Quantum Theory of Materials (IAS-1)

Ab *initio* investigations of magnetic properties of ultrathin transition-metal films on *4d* substrates

Ali Al-Zubi

Schriften des Forschungszentrums Jülich
Reihe Schlüsseltechnologien / Key Technologies Band / Volume 16

ISSN 1866-1807 ISBN 978-3-89336-641-5

Bibliographic information published by the Deutsche Nationalbibliothek.
The Deutsche Nationalbibliothek lists this publication in the Deutsche
Nationalbibliografie; detailed bibliographic data are available in the
Internet at http://dnb.d-nb.de

Publisher and Distributor:	Forschungszentrum Jülich GmbH Zentralbibliothek 52425 Jülich Phone +49 (0) 24 61 61-53 68 · Fax +49 (0) 24 61 61-61 03 e-mail: zb-publikation@fz-juelich.de Internet: http://www.fz-juelich.de/zb
Cover Design:	Grafische Medien, Forschungszentrum Jülich GmbH
Printer:	Grafische Medien, Forschungszentrum Jülich GmbH

Schriften des Forschungszentrums Jülich
Schlüsseltechnologien / Schlüsseltechnologien Band / Volume 16

D 82 (Diss., RWTH Aachen, Univ., 2010)

ISSN 1866-1807
ISBN 978-3-89336-641-5

Abstract

In this thesis, we investigate the magnetic properties of $3d$ transition-metal monolayers on $4d$ transition-metal substrates by means of state of the art first-principles quantum theory. In contrast to previous investigations on noble metal substrates, the strong hybridization between $3d$ metals and the substrate is an additional parameter determining the properties. In order to reveal the underlying physics of these systems we study trends by performing systematic investigations across the transition-metal series. Case studies are presented for which Rh has been chosen as exemplary $4d$ substrate. We consider two substrate orientations, a square lattice provided by Rh(001) and a hexagonal lattice provided by Rh(111).

We find, all $3d$ transition-metal (V, Cr, Mn, Fe, Co and Ni) monolayers deposited on the Rh substrate are magnetic and exhibit large local moments which follow Hund's rule with a maximum magnetic moment for Mn of about $3.7\,\mu_B$ depending on the substrate orientation. The largest induced magnetic moment of about $0.46\,\mu_B$ is found for Rh atoms adjacent to the Co(001)-film.

On Rh(001) we predict a ferromagnetic (FM) ground state for V, Co and Ni, while Cr, Mn and Fe monolayers favor a $c(2 \times 2)$ antiferromagnetic (AFM) state, a checkerboard arrangement of up and down magnetic moments. The magnetic anisotropy energies of these ultrathin magnetic films are calculated for the FM and the AFM states. With the exception of V and Cr, the easy axis of the magnetization is predicted to be in the film plane.

With the exception of Fe, analogous results are obtained for the $3d$-metal monolayers on Rh(111). For Fe on Rh(111) a novel magnetic ground state is predicted, a double-row-wise antiferromagnetic state along the $[11\bar{2}]$ direction, a sequence of ferromagnetic double-rows of atoms, whose magnetic moments couple antiferromagetically from double row to double row. The magnetic structure can be understood as superposition of a left- and right-rotating flat spin spiral.

In a second set of case studies the properties of an Fe monolayer deposited on varies hexagonally terminated hcp (0001) and fcc (111) surfaces of $4d$-transition metals (Tc, Ru, Rh, to Pd) are presented. The magnetic state of Fe changes gradually from noncollinear 120° Néel state for Fe films on Tc, and Ru, to the double-row-wise antiferromagnetic state on Rh, to the ferromagnetic one on Pd and Ag. The noncollinear state is a result of antiferromagnetic intersite exchange interactions in combination with the triangular lattice provided by the hexagonal surface termination of the (111) surfaces. A similar systematic trend is observed for a Co monolayer on these substrate, but shifted towards ferromagnetism equivalent to one element in the periodic table.

Also the magnetic properties of Co chains on stepped Rh(111) surfaces is investigated. It is shown that the easy axis of the magnetization changes from out-of-plane in case of a Co monolayer to in-plane for the atomic chain.

The trends are explained on the basis of the Heisenberg model with exchange parameters whose sign and value change systematically as function of the band filling across the transition-metal series. The Heisenberg model was extended by a Stoner-like term to

include the induced magnetization of the $4d$ substrate.

The results are based on the density functional theory in the vector-spin-density formulation employing the spin-polarized local density and generalized gradient approximation. The self-consistent relativistic total energy and force calculations have been carried out with the full-potential linearized augmented plane wave (FLAPW) method in the film geometry. The concept of total-energy calculations with incommensurable spin-spirals of wave vectors along the high-symmetry lines in the two-dimensional Brillouin zone was applied to search for the magnetic ground states.

"A human being is part of the whole called by us universe, a part limited in time and space. We experience ourselves, our thoughts and feelings as something separate from the rest. A kind of optical delusion of consciousness. This delusion is a kind of prison for us, restricting us to our personal desires and to affection for a few persons nearest to us. Our task must be to free ourselves from the prison by widening our circle of compassion to embrace all living creatures and the whole of nature in its beauty. The true value of a human being is determined by the measure and the sense in which they have obtained liberation from the self. We shall require a substantially new manner of thinking if humanity is to survive." (Albert Einstein, 1954)

Contents

Introduction

During the past two decades, we witnessed a significant theoretical and experimental effort to understand the magnetism of the ultrathin magnetic films epitaxially grown on oriented nonmagnetic substrates. Mainly the weakly interacting coinage metals (Cu, Ag, Au) and some transition metals (TMs), e.g. Pd, have been chosen as substrate in order to minimize the interaction between monolayer and substrate [1, 2]. Cu with an experimental lattice constant of $a_o = 3.61$ Å turned out to be an ideal template for fcc bulk TMs, while Ag ($a_o = 4.09$ Å) and Au ($a_o = 4.08$ Å) are templates to grow the bcc metals.

Significant understanding and guidance of the experiments was provided by the density functional theory (DFT), a material specific first-principles theory with predictive power, which became increasingly applicable due to an international effort in developing appropriate electronic structure methods and the increased availability of computing power. Employing density functional theory, some general trends were identified for $3d$ monolayers (ML) on these substrates: (i) The magnetic moments of the monolayers are considerably enhanced as compared to the equivalent bulk systems and (ii) similar to the bulk cases, Fe, Co, and Ni are ferromagnets (FM) on these substrates, while V, Cr, and Mn prefer a $c(2 \times 2)$ antiferromagnetic (AFM) structure, i.e., a checkerboard arrangement of antiparallel magnetic moments [3, 4, 5], a magnetic structure which cannot be derived from respective bulk phases. Experimentally, Ortega and Himpsel studied $3d$ monolayers on Ag(001) and confirmed the theoretical predictions, especially the magnetism of V on Ag(001) [6].

More recently, the field has taken a different turn moving away from monolayers on weakly interacting substrates to those on $4d$ and $5d$ transition-metal ones. This is motivated by a couple of unexpected findings, which include the prediction of a ferromagnetic phase for the prototype antiferromagnet Cr [7], the prediction [7, 8, 9, 10] and experimental verification of the $c(2\times2)$ AFM phase for Fe [11], the prediction of $c(2\times2)$ AFM Co [7], and the discovery of a homochiral cycloidal magnetic phase for Mn [12, 13] all as monolayers on W(001), as well as frustrated magnetic phases of an Fe monolayer TaW(001) alloy substrate [14].

These findings motivate a more systematic investigation of monolayers on $4d$ and $5d$ substrates in general. In this thesis we investigate $3d$ monolayers on the $4d$ TM substrate Rh(001) and Rh(111). Rh has a large Stoner enhanced susceptibility as shown for Rh films on Fe [15] and FeRh is known to form ordered alloys in the cesium chloride (CsCl-type) structure with subtle magnetic properties [16, 17, 18]. The lattice constant of Rh

($a_o = 3.80$ Å) is in between those of Cu and Ag and thus Rh serves as a potential substrate to grow artificial phases of $3d$ transition-metal films such as fcc-Fe stabilized under tensile strain or bcc-Co under compressive strain. The Rh(001) substrate provides favorable growth conditions for transition-metal films despite a large lattice mismatch of fcc Fe or Co and bcc Fe with Rh of about 6%, 8% and -7%, respectively. For example, no notable intermixing has been encountered at the interface of Fe/Rh(001) during growth of Fe films [19]. Epitaxial, pseudomorphic layer-by-layer growth of one and two layers of Co on Rh(001) was reported by Begley *et al.* [20] and several groups [19, 21, 22, 23] have been able to grow pseudopmorphically even thicker films of face-centered tetragonal Fe on Rh(001). Hayashi *et al.* [22, 23] concluded on the basis of soft X-ray magnetic circular dichroism (XMCD) experiments measured at room temperature that a monolayer and a bilayer of Fe are not ferromagnetic and interpreted them as magnetically dead caused by the large strain exerted in the interface of the thin film and the substrate. Hwang *et al.* [24] found experimentally a suppression of the ferromagnetic order of Fe overlayers on the Rh(001) surface, and he as well as Spisak *et al.* [25] predicted a $c(2 \times 2)$ AFM order for 1 ML Fe on Rh(001) on the basis of DFT calculations.

Experimentally, the magnetic properties of FM monolayers can be investigated with highly developed surface sensitive techniques, such as the spin-polarized scanning tunneling microscope (SP-STM)[26]. A challenge is to study the ground state for complex magnetic structures with atomic resolution such as Fe on W(001) [11] or even anti-ferromagnets like Mn on hexagonal surfaces, due to the topological frustrations on triangular lattices. A measure of the challenge can be estimated from the pioneering experimental study of the magnetic state of a Fe monolayer on Ir(111) surface [27, 28], which revealed a very complex ground state, and was approached theoretically to be described by a 15 atom unit cell, a 7:8 mosaic structure with seven Fe atoms pointing in one quantization axis and eight in the opposite one. The resolution of atomic-scale spin structures by the spin-polarized scanning tunneling microscope was studied theoretically [29, 30] and followed by a new theoretical prediction of a three-dimensional non-collinear ground state of a Mn monolayer on the Cu(111) substrate, called $3\mathbf{Q}$-state [31]. Such non-collinear systems can be studied by employing the classical Heisenberg model, where the atomic spins are considered to be localized at the lattice sites and interact with each other by intersite exchange interaction parameters obtained in part by density functional theory. These exchange interactions are typically long-ranged as we deal here with metals and their Fermi surfaces. The general solution of the classical Heisenberg model for a periodic system are spin-spirals, magnetic moment of equal length on each site, rotating in spin-space by a constant angle from site to site. Calculating the total energy of such spin-spiral states from first-principles can be used to construct a model Hamiltonian with constant local spin moments, where the exchange interaction parameters can be calculated by fitting the total energy dispersion curve to this model Hamiltonian. Though, there are many possible applications for spin-spiral calculations, it was the discovery of a spiral ground state structure in fcc iron [32] and $4f$ and $5f$ metals [33] that gave rise to many theoretical studies [34, 35].

Most likely the magnetic ground state can be found for spin-spiral wave vectors, which lie at the high-symmetry lines of the two-dimensional Brillouin zone. High-symmetry points at the vertices of these lines correspond to well-known magnetic structures such as the ferromagnetic state for the Γ point or a well-known antiferromagnetic structure. Along the high-symmetry lines there are points at which the Heisenberg model is energetically degenerate with respect to a superposition of several, frequently symmetry-related wave vectors, so-called multi-$\mathbf{Q}$ states and then energy gain can be expected by lifting these degeneracies due to higher order spin interactions, such as 4-spins or biquadratic interactions described by the Hubbard model [36, 37, 38, 31]. These higher order interactions modify the energetics of the classical Heisenberg Hamiltonian by a value, which equals to the energy difference between the single- and multi-$\mathbf{Q}$ state. Since first-principles calculations contain in principle all interactions and not only those described by the Heisenberg model, a significant total-energy difference between a single- and multi-$\mathbf{Q}$ is a clear indication that higher order interactions are important and from this energy difference in comparison to the extended Heisenberg model we can extract parameters for these higher order terms, and then use them in the modified model Hamiltonian in predicting the true magnetic ground state from calculated zero-temperature phase diagrams [31, 38].

Indeed, in low dimensions magnetic fluctuations are prone to destroy the long range order. Therefore, the magnetic anisotropy, which particularly large for magnets at surfaces and in low dimensions such as atomic chains plays a crucial role as this interacting stabilizes the long-ranged order against the fluctuations. Experimentally, it is sometimes possible to evaporate the magnetic metal that will be naturally assembled as an atomic-chain at the step-edge. Many theoretical and experimental studies were performed to investigate the magnetic properties of atomic chains deposited on stepped surfaces, using the SP-STM in combination with the XMCD. Therefore, it became possible to arrange atoms in chains along steps of suitable substrates and to analyze their properties [39, 40]. For example, ferromagnetism was observed in one-dimensional mono-atomic metal chains [41], and a giant magnetic anisotropy of single cobalt atoms and nanoparticles [42], an oscillatory magnetic anisotropy in one-dimensional atomic wires of different thickness[43] was reported. In-plane magnetocrystalline anisotropy was observed on Fe/Cu(111) nanostructures grown on stepped surfaces[44, 45], and the observation of spin and charge collective modes in one-dimensional metallic chains[40] was reported. The spin and orbital magnetization was investigated in self-assembled Co clusters on Au(111) step-edge. A strong magnetic surface anisotropy of ultrathin Fe was observed on curved Pt(111)[46] and finally spin and orbital magnetization was explored in self-assembled Co clusters on Au(111)[47].

In Chapter 1 of this thesis we review the density functional theory introduced by Hohenberg and Kohn [48]. It states that the ground-state energy can be uniquely described by an energy functional of the ground-state density of the electrons. Effective approximations to the energy functional are available, which are applicable to the metallic systems studied in this thesis.

Chapter 2 describes shortly the full-potential linearized augmented plane wave (FLAPW) method [49] as implemented in the Jülich developed FLEUR code [50], a versatile electronic structure method, optimally suited to treat thin magnetic films and which solves the density functional equations in the vector-spin density formulation.

In Chapter 3, we describe elementary magnetic models, which provide a basis to the understanding of our results or the guidance of our calculations. To name is the Stoner model [51, 52, 53, 54], which provides an instability criterion for the spontaneous appearance of a magnetic phase, in particular the ferromagnetic phase, by parameters, which are essential to density-functional theory calculations, the nonmagnetic density of states at the Fermi energy which is directly related to the dimensionality of the system and the exchange integral. It provides thus an elementary understanding of the appearance of magnetism in low-dimensions. To name is also the Heisenberg model, which provides the basis for understanding the variety of possible magnetic phases including the noncollinear magnetic phases. In the last part of the chapter, we also lay out the theory of the magnetic anisotropy energy (MAE) of ultrathin films which reduces in low-dimensional systems basically to the magnetocrystalline anisotropy (MCA), because the shape anisotropy becomes very small. Knowing the MCA of a magnetic system is very important, since this quantity determines to a large extent the functionality of the system and at the same time it is responsible stabilizing the long-ranged magnetic order against thermal fluctuations at finite temperatures.

In Chapter 4 we will show our results obtained from collinear DFT calculations of the structural relaxation and the magnetic properties of $3d$ transition-metals monolayers on Rh(001) and Rh(111) substrates, using the FLAPW method. We find that Cr, Mn and Fe prefer a c(2×2)-AFM solution, while V, Co and Ni favor the FM ground state on the Rh(001) surface. I present the calculated MCA values for $3d$ monolayers on the Rh(001) substrate, The results are analyzed according to Bruno's model [55]. We will also show the Rh crystal field and how the $3d$-Rh hybridization effects the values of the MCA and the easy axis of magnetization. In the second part of this chapter I focus on the Rh(111) substrate and I will show that for for Cr and Mn monolayers, the row-wise antiferromagnetic structure has the lowest energy, while for Fe, Co and Ni on Rh(111) the FM solution is more more stable.

In Chapter 5, we focus our study on the ground state of Fe on hexagonal substrates. The starting point is Fe/Rh(111), whose ferromagnetic state is only a small energy (24 meV/Fe) below the antiferromagnetic state and thus close the region of phase transition, as found for Fe/Rh(111) in Chapter 4 . This result is not sufficient to declare the ground state of Fe to be ferromagnetic, in particular since we expect that antiferromagnetic interactions in combination with the triangular lattice of the hexagonal termination of the substrate can give rise to very complicated magnetic structures driven by minimizing the frustration in the exchange parameters. Therefore, we will analyze the magnetic ground state of Fe on the Rh(111) substrate by performing non-collinear spin-spirals total-energy calculations using the FLEUR code [56]. From the spin-spiral calculation, we would straight forwardly conclude that the ground state of Fe is noncollinear with an energy gain of 5 meV/Fe atom with respect to the FM solution. We will also line out that the true ground state of Fe/Rh(111) is not a single- but a double-$\mathbf{Q}$ ground state, stabilized by higher order interactions, and the proposed model Hamiltonian should be modified to include the substrate moments in case of highly polarized substrates. We will show from similarly performed calculations that Fe on Tc(0001) has a 120° Néel ground state and not the row-wise antiferromagnetic state discussed in Chapter 4, obtained from collinear calculations. At the end of the chapter we compare our results with other results obtained for Fe on Ru(0001) [57] and Ag(111) [30].

In the last chapter, we will present our results of Co on hexagonally terminated substrates of $4d$-transition metals. Similar to Fe, we will show that Co might lose its FM state if we change the substrate from the late through the early transition metals. we will additionally show calculated values for the magnetocrystalline anisotropy of ferromagnetic Co and Fe monolayers on hexagonal $4d$ transition-metal substrates. We will show that the MCA of Fe is not strongly affected by the substrate, but the MCA of Co is. This leads us to chose Co as a case of study to analyze the MCA of atomic Co chain on microfaceted Rh$\langle 111\rangle$. We will compare our obtained MCA results of the Co chain on the stepped Rh(664) surface to a previous study of Co chains on Pt$\langle 111\rangle$, and will show that relaxations play a crucial role in determining a reliable prediction of the magnetization direction consistent with experimental results. In particular, it is shown that for Co on Rh(111) the easy axis of the magnetization changes from out-of-plane for the monolayer to in-plane of the atomic chain.

At the end, the thesis is summarized and concluded.

Chapter 1

Density functional theory (DFT)

1.1 Overview

Theoretical physics had enormous development early times of the last century. It started when the particle-wave nature was verified through the work of Albert Einstein and Louis de Broglie and many others. The prediction of chemical or physical properties of material requires quantum mechanical treatment of the many-body system of electrons and nuclei with their basic electrostatic Coulomb interactions. In quantum mechanics, the electrons are described as particles and waves at the same time using the single equation by Erwin Schrödinger in 1926[58]:

$$\hat{H}\Psi(\mathbf{r}_i, t) = E\Psi(\mathbf{r}_i, t) \tag{1.1}$$

where $\hat{H}$ is the Hamiltonian operator, which is the summation of the electrons Hamiltonian $\hat{H}_{el}$, the nuclei Hamiltonian $\hat{H}_{nucl}$ and the electron-nucleus interaction potential term U_{int}. $\Psi(\mathbf{r}_i, t)$ is the many-particle wave function of all particles i at positions $\mathbf{r}_i$ at time t. E is the energy eigenvalue of the many-particle system. The Schrödinger equation becomes:

$$(\hat{H}_{el} + \hat{H}_{nucl} + U_{int})\Psi(\mathbf{r}_i, t) = E\Psi(\mathbf{r}_i, t) \tag{1.2}$$

It is possible to solve equation 1.2 for the H atom, because it has only one proton and one electron. Several approaches can be taken to simplify solving this equation for many-particle systems. One famous approach is the Born-Oppenheimer approach, which separates the kinetic energy of the nucleus with respect to the kinetic energy of the electrons. This approach works because the mass of the proton is about 1836 times the electron mass, and therefore the movement is slow with respect to the electron speed. As a result we only need to solve the Schrödinger equation for N electrons. For electron i at position $\mathbf{r}_i$ from the nuclei α with Z_α at $\mathbf{r}_\alpha$, equation 1.2 becomes

$$\hat{H} = \sum_{i=1}^{N}(-\frac{1}{2}\nabla_i^2) - \sum_{i=1}^{N}\sum_{\alpha}\frac{Z_\alpha}{|\mathbf{r_i} - \mathbf{r}_\alpha|} + \frac{1}{2}\sum_{j\neq i}\frac{1}{|\mathbf{r}_i - \mathbf{r}_j|} \tag{1.3}$$

Atomic units are employed, the length unit is the Bohr radius (a_0=0.5292 Å), the charge unit is the charge of the electron, e ($e = 1.602 \cdot 10^{-19}C$), and the mass unit is the mass of the electron, m_e. The first term in equation (1.3) is the sum of the kinetic energy operators for all electrons in the system. The second term is the sum of the electron-nucleus Coulomb attractions. The third term is the sum of the electron-electron Coulomb repulsions.
For solids N is larger than 10^{23}. This makes the solution of such equation with $3N$ special and N spin variables unobtainable obtainable without using approximations. Many numerical methods and approaches were developed to solve this equation. The most powerful theory was introduced by Hohenberg and Kohn in 1964[48], where they proposed that the ground-state properties of the many-particle system can be determined by the ground-state particle charge density $n(\mathbf{r})$. This means that the degrees of freedom are reduced to be only three instead of $3N$. This theory is called "Density Functional Theory (DFT)", it avoids the complicated many-body wavefunction and uses the electronic density for band-structure calculations. DFT is designed to calculate the total energies for small systems (up to few hundreds of nonequivalent atoms) at zero Kelvin.

1.2 Origin of DFT

In the 1920s, Thomas and Fermi could approximate the electronic distribution of an atom by assuming a uniform distribution of the electrons in a field of an effective potential[59],[60]. They could represent the electronic total energy $\mathbf{E}_{TF}$ as a functional of the uniform electrons' density $n(\mathbf{r})$.

$$E[n(\mathbf{r})] = T_{TF}[n(\mathbf{r})] + E_H[n(\mathbf{r})] + U_{ext}[n(\mathbf{r})] \tag{1.4}$$

where $n(\mathbf{r})$ is the density of electrons in the solid.

$$T_{TF}[n(\mathbf{r})] = C_F \int n(\mathbf{r})^{5/3} d\mathbf{r} \tag{1.5}$$

is the Thomas-Fermi kinetic energy of electrons of density $n(\mathbf{r})$. C_F is a constant,

$$E_H[n(\mathbf{r})] = \frac{1}{2}\int\int \frac{n(\mathbf{r})n(\mathbf{r}')}{|\mathbf{r} - \mathbf{r}'|} d\mathbf{r}d\mathbf{r}' \tag{1.6}$$

is the Hartree energy, or the Coulomb interaction of the electron density with itself, and

$$U_{ext}[n(\mathbf{r})] = -\sum_{\alpha}\frac{Z_\alpha}{r_\alpha}\int n(\mathbf{r})d\mathbf{r} \tag{1.7}$$

is the classical interaction between the electrons and the Coulomb field of the nucleus $v_{ext}(\mathbf{r})$. The electron ground state density minimizes the energy functional $E[n(\mathbf{r})]$ for the ground state of an atom under the constraint

$$N = N[n] = \int n(\mathbf{r})d\mathbf{r} \tag{1.8}$$

where N is the total number of electrons in the atom. The ground-state electron density must satisfy the variational principle

$$\delta E_{TF}[n] - \mu_{TF}(\int n(\mathbf{r})d\mathbf{r} - N) = 0 \tag{1.9}$$

which yields the Euler-Lagrange equation

$$\mu_{TF} = \frac{\delta E_{TF}[n]}{\delta n(\mathbf{r})} = \frac{5}{3}C_F n^{3/2}(\mathbf{r}) - \varphi(\mathbf{r}) \tag{1.10}$$

where μ_{TF} is the Lagrange multiplier,called chemical potential, associated with the constraint in eq. (1.8), and

$$\varphi(\mathbf{r}) = \frac{Z}{r} - \int \frac{n(\mathbf{r}')}{\mathbf{r} - \mathbf{r}'}d\mathbf{r}' \tag{1.11}$$

is the electrostatic potential at point $\mathbf{r}$ due to the nucleus and the entire electron distribution.

In 1964, Hohenberg and Kohn could show that the Thomas-Fermi model is an approximation of an exact theory[48]. They could represent the total energy fully as a functional of the electron density $n(\mathbf{r})$ for a given external potential $v_{ext}(\mathbf{r})$ for N-electron system. Then eq. (1.7) becomes

$$U_{ext}[n] = \int n(\mathbf{r})v_{ext}(\mathbf{r})d\mathbf{r} \tag{1.12}$$

this means that they didn't restrict the external potential $v_{ext}(\mathbf{r})$ to be only the classical Coulomb potential as Thomas and Fermi did. Instead, they proposed that $v_{ext}(\mathbf{r})$ is determined by the electron density, within a trivial additive term. Then the total energy of the system becomes

$$E[n] = \int n(\mathbf{r})v_{ext}(\mathbf{r})d\mathbf{r} + E_{HK}[n] \tag{1.13}$$

where

$$E_{HK}[n] = T[n] + E_H[n] + \mathbf{nonclassical\ \ term} \tag{1.14}$$

The energy variational principle is also provided such that for a trail density $\tilde{n}(\mathbf{r}) \geq 0$ and satisfies eq. (1.8), then the corresponded energy $E[\tilde{n}(\mathbf{r})]$ must be the upper limit of the ground state energy E_0

$$E_0 \leq E[\tilde{n}(\mathbf{r})] \quad \textbf{and} \quad \delta E[\tilde{n}(\mathbf{r})] = 0 \tag{1.15}$$

Assuming the $E[n]$ in eq (1.13) is differentiable, the ground-state density must also satisfy the stationary principle in eq. (1.9) according to the variational principle (1.15). The Euler-Lagrange equation (1.10) becomes

$$\mu = v_{ext}(\mathbf{r}) + \frac{\delta E_{HK}[n]}{\delta n(\mathbf{r})} \tag{1.16}$$

The great advantage of this theory is the reduction of the degrees of freedom from 3N, if the energy is represented as a functional of wave function $E[\Psi]$, to only 3 degrees of freedom since the electron density depends only on space vector $\mathbf{r}$. Because of that, a huge step was performed toward productive calculations in computational physics.

Hohenberg and Kohn didn't treat the kinetic energy term in Thomas and Fermi model, they only reformulated the total energy as functional in density which minimizes the energy functional in an external potential and describes all electronic properties of the system. The difficulty which was and remained is in calculating the kinetic energy of the interacting electrons. Many approximations were done, but they didn't give enough accuracy which encourages further hard work on that. The solution came one year after Hohenberg and Kohn published there article about DFT. In 1965 Kohn and Sham were able to solve of one part the problem by assuming a non-interacting electron system, with kinetic energy $T_{KS}[n]$ which can be accurately computed and covers a large part of the exact $T[n]$. This is explained in the next section.

1.3 The Kohn-Sham equations

Kohn and Sham proposed a kinetic energy, that can be calculated accurately, by introducing wavefunctions of non-interacting electrons into the problem[61]. It is assumed that these wavefunctions lead to the same ground state density as the many body wavefunction Ψ. The correction to this kinetic energy can be handled separately through an exchange correlation energy term. Equation (1.13) becomes

$$E[n] = T_{KS}[n] + \int n(\mathbf{r}) v_{ext}(\mathbf{r}) d\mathbf{r} + E_H[n] + E_{XC}[n] \tag{1.17}$$

where

$$T_{KS}[n] = \sum_i^N \langle \psi_i | -\frac{1}{2}\nabla^2 | \psi_i \rangle \tag{1.18}$$

is the kinetic energy introduced in terms of single particle orbitals ψ_i. Since T_{KS} is density functional, satisfying Pauli principle, this leads that

$$n(\mathbf{r}) = 2\sum_{i}^{N} |\psi_i|^2 \tag{1.19}$$

The functional $E_{XC}[n(\mathbf{r})]$ in equation 1.17 is the exchange-correlation energy. It includes the non-classical of the Coulomb repulsion term in eq. (1.14) and the kinetic energy difference $T[n] - T_{KS}[n]$. From these equations one can write the Kohn-Sham Hamiltonian of N-noninteracting electrons as an effective single particle Schrödinger equation

$$\{-\frac{1}{2}\nabla^2 + v_{eff}(\mathbf{r})\}\psi_i(\mathbf{r}) = \epsilon_i \psi_i(\mathbf{r}) \tag{1.20}$$

where v_{eff}, the effective Kohn-Sham potential, is defined by

$$v_{eff}(\mathbf{r}) = v_{ext}(\mathbf{r}) + \frac{\delta E_H}{\delta n} + \frac{\delta E_{XC}}{\delta n} = v_{ext}(\mathbf{r}) + \frac{1}{2}\int \frac{n(\mathbf{r}')}{|\mathbf{r} - \mathbf{r}'|} d\mathbf{r}' + v_{xc}(\mathbf{r}) \tag{1.21}$$

1.4 Spin Density Functional Theory

Most atoms, magnetic solids, many surfaces, thin films or nanostructures on surfaces. exposed to an external magnetic field posses a non-zero ground state magnetization. In order to describe these systems and characterize them completely, DFT Kohn-Sham formalism can be extended to take into account the magnetization density, $m(\mathbf{r})$, explicitly. This was started by von Barth and Hedin in 1972[62]. For such systems the density can be replaced by a hermitian 2×2 matrix $\underline{n}(\mathbf{r})$

$$\underline{n}(\mathbf{r}) = \frac{1}{2}(n(\mathbf{r})\underline{\mathrm{I}} + \underline{\sigma}.\mathbf{m}(\mathbf{r})) \tag{1.22}$$

where $\underline{\mathrm{I}}$ is a 2×2 unit matrix, $\underline{\sigma}$ is the Pauli spin space matrix. This density matrix will correspond to an effective potential matrix, which includes the scalar electric potential and the magnetic effective vector potential

$$\underline{v}_{eff}(\mathbf{r}) = v_{eff}(\mathbf{r})\underline{\mathrm{I}} + \mu_B \underline{\sigma}.\mathbf{B_{eff}}(\mathbf{r}) \tag{1.23}$$

where

$$\mathbf{B_{eff}}(\mathbf{r}) = \mathbf{B_{ext}}(\mathbf{r}) + \mathbf{B_{xc}}(\mathbf{r}) \ \text{ with } \ \mathbf{B_{xc}}(\mathbf{r}) = \frac{\delta E_{xc}[n, \mathbf{m}]}{\delta \mathbf{m}} \tag{1.24}$$

The one particle Schrödinger equation (1.20) becomes what is called the "Schrödinger-Pauli equation".

$$\{-\frac{1}{2}\nabla^2 + \underline{v}_{eff}(\mathbf{r})\} \begin{pmatrix} \psi_i^{\uparrow}(\mathbf{r}) \\ \psi_i^{\downarrow}(\mathbf{r}) \end{pmatrix} = \epsilon_i \begin{pmatrix} \psi_i^{\uparrow}(\mathbf{r}) \\ \psi_i^{\downarrow}(\mathbf{r}) \end{pmatrix} \tag{1.25}$$

If it is sufficient to propose that the magnetic field is parallel to the z-axis, this leads to diagonalize the Hamiltonian in eq. (1.25) into two spin components of the basis set ψ_i. This means that spin-up and spin-down problems become decoupled and can be solved independently. On the other hand, all physical observables become functionals of the spin-up and spin-down electron density, satisfying equation (1.19).

1.5 Approximations made to the exchange-correlation term E_{XC}

To get an exact solution, it would be necessary to find the exchange-correlation term exactly. This means one should determine the exact exchange-correlation potential, v_{xc}. This problem lead to many approximations to v_{xc} depending on the treated electronic systems. The most widely used approximation for v_{xc} is founded on the assumption that the charge density $n(\mathbf{r})$ is slowly varying and can be approximated locally by a homogeneous electron gas (HEG). Then the local contribution to the exchange-correlation energy should be identical to the contribution from a uniform electron gas of the same electron and magnetization densities. This leads to the most widely used approximation in DFT, the Local Spin Density Approximation (LSDA), which yields

$$E_{XC}[n, |\mathbf{m}|] \approx E_{XC}^{LSDA}[n, |\mathbf{m}|] = \int n(\mathbf{r})\epsilon_{xc}(n, |\mathbf{m}|)d^3\mathbf{r} \tag{1.26}$$

where $\epsilon_{xc}(n)$ is the exchange-correlation energy density per electron as a function of the uniform electron gas density n with a collinear magnetization density $|\mathbf{m}(\mathbf{r})|$. There are many approximate expressions for $\epsilon_{xc}(n, |\mathbf{m}|)$. The exchange-correlation in LSDA can be decomposed linearly into an exchange and correlation part:

$$E_{XC} = E_X + E_C \tag{1.27}$$

The HEG exchange part is known analytically, while the correlation part is not known except for very high or low densities[63],[64]. Because of that, many approximations for the LSDA correlation functionals have been proposed[65],[66],[67], often based on quantum Monte-Carlo studies, that have been parametrized.

In the local spin density approximation the exchange-correlation potential v_{xc}, the functional derivative of E_{XC}^{LSDA} with respect to the density $n(\mathbf{r})$, takes the form

$$v_{xc}^{LSDA}(\mathbf{r}) = \frac{\delta E^{LSDA}[n, |\mathbf{m}|]}{\delta n} = \epsilon_{xc}(n, |\mathbf{m}|) + n(\mathbf{r})\frac{\partial \epsilon_{xc}(n, |\mathbf{m}|)}{\partial n} \tag{1.28}$$

This leads to a local exchange-correlation magnetic field

$$B_{xc}^{LSDA}(\mathbf{r}) = n(\mathbf{r})\frac{\partial \epsilon_{xc}(n, |\mathbf{m}|)}{\partial |\mathbf{m}|}\hat{\mathbf{m}}(\mathbf{r}) \tag{1.29}$$

The LSDA is a local approximation, considering a constant local electron density per unit volume, and does not take the density variation into account. It was proved that it is more accurate to introduce new approximation by expressing the exchange-correlation energy as a function of the local density for each spin, $n_\uparrow(\mathbf{r})$, $n_\downarrow(\mathbf{r})$, their gradients $\nabla n_\uparrow(\mathbf{r})$, and $\nabla n_\downarrow(\mathbf{r})$. This approximation is called "Generalized Gradient Approximation" (GGA). The exchange-correlation energy in GGA is expressed as

$$E_{XC} \approx E^{GGA}[n_\uparrow, n_\downarrow] = \int f(n_\uparrow, n_\downarrow, \nabla n_\uparrow, \nabla n_\downarrow) d^3\mathbf{r} \tag{1.30}$$

Using this approximation, Perdew and Wang could derive an accurate and simple analytic representation of the HEG's correlation energy[68],[69]. More developments were done on GGA to increase its accuracy. LSDA and GGA are the most widely used approximations for homogeneous electronic systems like metals. By that, DFT provides a reliable relationship between $n(\mathbf{r})$ and the ground-state energy. The Kohn-Sham formalism, particularly the LSDA or GGA, is not designed to describe excited state properties. In particular, the eigenvalues ϵ_i, whose differences are often interpreted as single particle excitation energies, yield band gaps for insulators which are smaller than those found by experiment. In addition, some quantities which can be computed from LSDA ground state properties may be in error. For example, LSDA usually overestimates the cohesive energy of solids. This is thought to occur because the LSDA does a poor calculation of the total energy in isolated atoms. The Kohn-Sham formalism often fails to adequately describe highly correlated systems such as the Mott insulators. Such problems tell us that we should be very careful in using DFT on systems with known properties before we attempt to predict properties of new materials. For example LDA+U method is used to treat strongly correlated systems using an unrestricted screened Hartree-Fock treatment for some localized orbital states and neglects the fine details of the spatial variations of the Coulomb potential[70].

Numerically, DFT usage can be described as follows: Given the positions and charges of the nuclei in the system, one can solve for the ground state charge density $n(\mathbf{r})$, which minimizes the total energy (eq. 1.17) by making an initial guess for $n(\mathbf{r})$. Then equation (1.21) and (1.28), if LDA is used as example, to calculate the Kohn-Sham potential, and then solve the Schrödinger equation (1.1), subject to the boundary conditions of the problem to obtain a new charge density 1.22. In principle this new charge density could be used to start the cycle over again. In practice this is numerically unstable, so the new and old charge densities are mixed. This mixing can be as simple as a linear combination of the old and new charge densities, or more complicated as the use of the Broyden method [71], which accelerates convergence. The mixed charge density is used to calculate a new Kohn-Sham potential in equation (1.21) and the process begins again. After a number of iterations the input and output charge densities will be numerically almost equal, the total energy will become converged, and the solution is self-consistent.

Chapter 2

The FLAPW method

In DFT there are several methods to solve Kohn-Sham equations and determine the material electronic structure. Basis-set based methods can be classified into three major approaches to calculate the Schrödinger-like equation[72]: Plane wave, Localized atomic(-like) orbitals, and atomic sphere methods. Plane waves play an important role in all widely used methods, and still is the basis of choice for many new developments. Atomic sphere methods are efficient approaches. The efficiency comes from the representation of the atomic-like features, which vary rapidly close to each nucleus and smoothly, between the atoms. Close to the nucleus, the basis sets are presented as smooth functions which are "augmented" near each nucleus by solving the Schrödinger-like equation in the sphere at each energy, and then match it to the outer wave function, usually plane wave. Then the method is called "Augmented Plane Wave" (APW) approximation. This approach was introduced by Slater in 1937[73]. The eigen-states of an independent-particle Schrödinger equation is expanded in terms of basis functions each is represented according to two characteristic regions illustrated in figure 2.1.

2.1 The generalized eigenvalue problem

The region around each atom in figure 2.1 is presented as sphere, or "muffin-tin", where the potential around each atom is similar to the potential of the atom. On the other hand, the potential is smooth in the interstitial region between the atoms. One approach is to expand the unknown one-electron wave function $\psi(\mathbf{r})$ in a set of predefined basis functions $\varphi(\mathbf{r})$. A quite general expression for such an expansion, for a system with translational symmetry with reciprocal lattice vector $\mathbf{G}$ and Bloch vector $\mathbf{k}$, would be

$$\psi_{\nu,\mathbf{k}}(\mathbf{r}) = \sum_j c_{\nu j\mathbf{k}} \varphi_{j\mathbf{k}}(\mathbf{r}). \tag{2.1}$$

where ν is a band index, the sum on j is finite in practice and the set of functions $\{\varphi_{j\mathbf{k}}(\mathbf{r})\}$ are in general neither orthonormal nor complete unless plane waves are used as basis

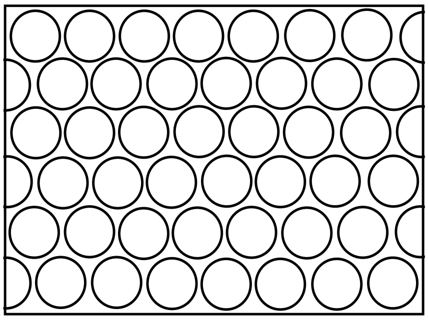

Figure 2.1: The division of space in the APW method. The muffin-tin spheres (MT) are surrounded by the interstitial region (I).

functions. The expansion coefficients $c_{ij\mathbf{k}}$ are determined from the secular equation, via the Rayleigh-Ritz principle [74]:

$$\sum_j [H_{jj'}(\mathbf{k}) - \epsilon_{\nu\mathbf{k}} S_{jj'}(\mathbf{k})] c_{\nu j\mathbf{k}} = 0, \tag{2.2}$$

where

$$H_{jj'}(\mathbf{k}) = \int_\Omega \varphi_{j\mathbf{k}}(\mathbf{r}) [\frac{-\nabla^2}{2} + V_{eff}^{\uparrow(\downarrow)}] \varphi_{j'\mathbf{k}}(\mathbf{r}) d^3r \tag{2.3}$$

are the elements of the Hamilton matrix and

$$S_{jj'}(\mathbf{k}) = \int_\Omega \varphi_{j\mathbf{k}}(\mathbf{r}) \varphi_{j'\mathbf{k}}(\mathbf{r}) d^3r \tag{2.4}$$

are the so-called overlap matrix elements. The integrals are evaluated over the volume of the unit cell (Ω). The type of functions $\{\varphi_{j\mathbf{k}}\}$ chosen, may or may not be energy-dependent, determines the detailed solution of the secular equation. The eigenvalues always follow from the condition

$$\det |H_{jj'}(\mathbf{k}) - \epsilon_{\nu\mathbf{k}} S_{jj'}(\mathbf{k})| = 0. \tag{2.5}$$

If plane waves are chosen as basis functions. They are orthogonal, diagonal in momentum and any power of momentum and the implementation of planewave based methods is rather straightforward because of their simplicity.

The APW is powerful approach but requires a solution on non-linear equations due to the matching between augmented functions the plane waves. This problem is explained in the next section, and it will be shown how it is useful to linearize the equations around reference energies, that one can solve this problem and get a solution on linear equations. One of the most important outcomes of linearization is the development methods like the LAPW and the Linearized Muffin-Tin Orbitals (LMTO) method [49, 75].

2.2 From augmented planewaves (APW) to Linearized (L)APW

In the APW approach, the planewaves that solve the Schrödinger equation in a constant potential are used in the interstitial region, while spherical harmonics times a radial function, that comes from the solution of the Schrödinger equation in a spherical potential inside the muffin-tins. The single particle wavefunctions $\psi_{i,\mathbf{k}}(\mathbf{r})$ are expanded in terms of the following basis functions:

$$\varphi_{\mathbf{G}}(\mathbf{k},\mathbf{r}) = \begin{cases} e^{i(\mathbf{G}+\mathbf{k})\cdot\mathbf{r}} & \text{interstitial region} \\ \sum\limits_{lm} A_L^{\mu\mathbf{G}}(\mathbf{k}) u_l(r|E_l) Y_L(\hat{\mathbf{r}}) & \text{muffin-tin sphere } \mu \end{cases}, \tag{2.6}$$

where $\mathbf{k}$ is the Bloch vector, $\mathbf{G}$ is a reciprocal lattice vector, L abbreviates the quantum numbers l and m and u_l is the regular solution of the radial Schrödinger equation to the energy E_l that corresponds to the eigenvalue of the wavefunction described with these basis functions:

$$\left\{-\frac{1}{2}\frac{\partial^2}{\partial r^2} + \frac{1}{2}\frac{l(l+1)}{r^2} + V(r) - \varepsilon_{\nu\mathbf{k}}\right\} r u_l(r) = 0. \tag{2.7}$$

E_l is an energy parameter and $V(r)$ is the spherical component of the potential. The coefficients $A_L^{\mu\mathbf{G}}(\mathbf{k})$ are determined from the requirement that the value of the wavefunctions have to be continuous at the boundary of the muffin-tin spheres.

In that sense, the APW's form a set of continuous basis functions that cover all space, where each function consists of a planewave in the interstitial region plus a sum of functions, which are solutions of the Schrödinger equation to a given set of angular momentum quantum numbers lm and a the energy E, inside the muffin-tin spheres. Several disadvantages are faced in this approach. If the E_l were kept fixed, used only as a parameter during the construction of the basis, the Hamiltonian could be set up in terms of this basis. This would lead to a standard secular equation for the band energies.

Unfortunately, it turns out, that the APW basis does not offer enough variational freedom if the E_l are kept fixed. An accurate description can only be achieved if they are set to the corresponding band energies. Requiring the E_l's to equal the band energies, which can no longer be determined by a simple diagonalization of the Hamiltonian matrix. Since the u_l's depend on the band energies, the solution of the secular equation becomes a nonlinear problem, which is computationally much more demanding than a secular problem. It is difficult to extend the APW method beyond the spherically averaged muffin-tin potential approximation, because in the case of a general potential the optimal choice of E_l is no longer the band energy. For a given choice of E_l, the radial functions u_l vanish at the muffin-tin radius, the boundary conditions on the spheres cannot be satisfied, i.e. the planewaves and the radial functions become decoupled. It can cause numerical difficulties if u_l becomes very small at the sphere boundary.

An additional term was introduced in the basis within the muffin-tin spheres in a method called the linearized augmented planewave method (LAPW) [76]. Extra variational freedom is added to the basis, so that it is not necessary to set the E_l equal to the band energy. This is done by including the derivative of the radial solution of the Schrödinger equation with respect to the energy. The construction, then, can be regarded as a linearization of the APW. In APW, the u_l's depend on the band energies and can thus be understood as functions of r and ϵ. Hence, u_l can be expanded into a Taylor-series around E_l,

$$u_l(\epsilon, r) = u_l(E_l, r) + \dot{u}_l(E_l, r)(\epsilon - E_l) + O[(\epsilon - E_l)^2]. \tag{2.8}$$

Here $\dot{u}_l$ denotes the energy derivative of u_l, $\partial u_l(\epsilon, r)/\partial\epsilon$, and $O[(\epsilon - E_l)^2]$ denotes errors that are quadratic in the energy difference. Therefore, an error of order $(\epsilon - E_l)^2$ in the wavefunction is introduced in the LAPW method. According to the variational principle the error in the calculated band energies is of the order $(\epsilon - E_l)^4$. Due to this high order, the linearization works very well even over rather broad energy regions. A single set of energy parameters is sufficient for the whole valence band in most cases. Sometimes the energy region has to be split up in two (very rarely more) windows with separate sets of energy parameters. The LAPW basis functions are of the form

$$\varphi_{\mathbf{G}}(\mathbf{k}, \mathbf{r}) = \begin{cases} e^{i(\mathbf{G}+\mathbf{k})\cdot\mathbf{r}} & \text{interstitial region} \\ \sum\limits_L [A_L^{\mu\mathbf{G}}(\mathbf{k}) u_l(r) + B_L^{\mu\mathbf{G}}(\mathbf{k}) \dot{u}_l(r)] Y_L(\hat{\mathbf{r}}) & \text{muffin-tin sphere } \mu \end{cases} \tag{2.9}$$

with the extra term $B_L^{\mu} \dot{u}_l(r) Y_L(\hat{\mathbf{r}})$ compared to the APW method. The additional coefficient is determined by requiring that not only the value of the basis functions, but also their derivatives with respect to r are continuous at the sphere boundaries. In any case is useful to require normalization

$$\langle u_l | u_l \rangle = \int_0^{R_{MT}} u_l^2(r) r^2 dr = 1. \tag{2.10}$$

Here R_{MT} is the muffin-tin sphere radius. Taking the derivative of (2.10) with respect to the energy it can easily be shown, that u_l and $\dot{u}_l$ are orthogonal. $\dot{u}_l$ is calculated from a Schrödinger-like equation, derived by taking the energy derivative of (2.7),

$$\left\{-\frac{1}{2}\frac{\partial^2}{\partial r^2}+\frac{1}{2}\frac{l(l+1)}{r^2}+V(r)-E_l\right\} r\dot{u}_l(r)=ru_l(r). \tag{2.11}$$

Still the solution of this equation has to be made orthogonal to u_l, since any linear combination of $\dot{u}_l$ and u_l also solves the equation. Once the u_l and $\dot{u}_l$ made orthogonal the basis functions inside the spheres form a completely orthogonal basis set, since the angular functions $Y_{lm}(\hat{\mathbf{r}})$ are also orthogonal. However, the LAPW functions are in general not orthogonal to the core states, which are treated separately in the LAPW method. This fact can cause problems in the presence of high lying core states. A detailed discussion of these problems and strategies to circumvent them can be found in the book by Singh [77], which includes a very comprehensive review of many aspects of the LAPW method.

With the construction of the LAPW basis the computational difficulties of the APW method are solved although we loose accuracy. Since it is no longer necessary to set the energy parameters equal to the band energies, the later can be determined by a single diagonalization of the Hamiltonian matrix. The LAPW method can be extended to non-spherical muffin tin potentials with little difficulty, because the basis offers enough variational freedom. This leads then to the full-potential linearized augmented planewave method (FLAPW). If u_l is zero at the sphere boundary, its radial derivative and $\dot{u}_l$ are in general nonzero. Then the boundary conditions can always be satisfied.

The nonlinearity inherent to the APW method can only be circumvented at the expense of a larger eigenvalue problem, because the requirement of continuous derivatives of R_{MT} makes the basis shift. Within LAPW (and also within APW) the basis functions in the interstitial are represented by planewaves. The functions inside the muffin tins are coupled to the planewaves via the boundary conditions, and can only be varied indirectly by a variation of the planewave coefficients. Clearly, with a finite number of planewaves, at maximum the same number of functions inside the spheres can be varied independently. Hence, to make use of the of the extra variational freedom, that the LAPW basis set allows compared to the APW basis, i.e. to vary the u_l's and the $\dot{u}_l$'s independently, more planewaves have to be used.

2.3 The Full-Potential LAPW

In the older applications of APW and LAPW methods, the potential in the unit cell $V(\mathbf{r})$ was approximated by

$$V(\mathbf{r})=\begin{cases} V_I^0 = const. & \text{interstitial region} \\ V_{MT}^0(r) & \text{muffin-tin spheres,} \end{cases} \tag{2.12}$$

using a constant potential in the interstitial region and a spherically symmetric potential inside each sphere. The LAPW method yields accurate results (energies) for close-packed metal systems. For crystals with open structures such as silizides, perovskites, surfaces or clusters, the restrictions to the potential (so-called shape-approximations) become difficult to justify. The full-potential LAPW method (FLAPW) [78, 49] is proposed by no shape-approximations in the interstitial region and inside the muffin-tin spheres. The constant interstitial potential V_I^0 is replaced by the warped potential $\sum V_I^{\mathbf{G}} e^{i\mathbf{G}\cdot\mathbf{r}}$ and to the spherical muffin-tin potential the non-spherical terms are added,

$$V(\mathbf{r}) = \begin{cases} \sum\limits_{\mathbf{G}} V_I^{\mathbf{G}} e^{i\mathbf{G}\cdot\mathbf{r}} & \text{interstitial region} \\ \sum\limits_{L} V_{MT}^{L}(r) Y_L(\hat{\mathbf{r}}) & \text{muffin-tin spheres.} \end{cases} \tag{2.13}$$

The charge density, $\rho(\mathbf{r})$, is represented in the same way as the potential:

$$n(\mathbf{r}) = \begin{cases} \sum\limits_{\mathbf{G}} n_I^{\mathbf{G}} e^{i\mathbf{G}\cdot\mathbf{r}} & \text{interstitial region} \\ \sum\limits_{L} n_{MT}^{L}(r) Y_L(\hat{\mathbf{r}}) & \text{muffin-tin spheres.} \end{cases} \tag{2.14}$$

The wavefunctions between the plane waves in the interstitial region and the radial muffin-tins' are different. This means they have to be matched in a way that the basis functions and their derivatives are continuous at the sphere boundaries. Within FLAPW the electron wavefunctions are expanded differently in the interstitial region and the muffin-tins. Each basis function consists of a planewave in the interstitial, which is matched to the radial functions and spherical harmonics in the muffin-tins. The coefficients, $A_L^{\mu\mathbf{G}}(\mathbf{k})$ and $B_L^{\mu\mathbf{G}}(\mathbf{k})$ in eq.(2.9), of the function inside the spheres are determined from the requirement, that the basis functions and their derivatives are continuous at the sphere boundaries. These coefficients play an important role. In this section we will therefore discuss how the matching conditions can be solved and what properties they induce. In many systems where the FLAPW method can be applied, some atoms are symmetry equivalent, i.e. these atoms can be mapped onto each other by a space group operation $\{\mathbf{R}|\tau\}$. Such a group of atoms is called an atom type, represented by one of the atoms. Let $\{\mathbf{R}^\mu|\tau^\mu\}$ be the operation that maps the atom μ onto its representative. This atom can now be assigned a local coordinate frame S^μ, where the origin of S^μ is at the atoms position $\mathbf{p}^\mu$.

The local frame is chosen such that the unit vectors of the local frame S^μ are mapped onto those of the global frame by $\mathbf{R}^g$ ($\mathbf{R}^\mu S^\mu = S^g$). The local frame of the representative atom S^α is only translated with respect to the global frame, i.e. the same rotation $\mathbf{R}^\mu$ maps S^μ onto S^α. The potential (and other quantities) inside the muffin-tins can now be written in terms of the local coordinate system. Due to the symmetry we find $V_{MT^\alpha}(\mathbf{r}^\alpha) = V_{MT^\mu}(\mathbf{r}^\mu)$, where $\mathbf{r}^\alpha$ and $\mathbf{r}^\mu$ are expanded in terms of the local frames S^α and S^μ respectively. As a consequence the radial functions $u_l(r)$ and the Hamiltonian matrices are the same for all atoms of the same type. This way symmetry is exploited to save memory and computing time (during the calculation of the t-matrices).

Any planewave can be expanded into spherical harmonics via the Rayleigh expansion,

$$e^{i\mathbf{K}\mathbf{r}} = 4\pi \sum_L i^l \; j_l(rK) \; Y_L^*(\hat{\mathbf{K}}) \; Y_L(\hat{\mathbf{r}}), \tag{2.15}$$

where $r = |\mathbf{r}|$, $K = |\mathbf{K}|$ and $\mathbf{K}$ abbreviates $(\mathbf{G} + \mathbf{k})$. Looked at from the local frame $\mathbf{K}$ and $\mathbf{p}^\mu$ appear rotated, besides the origin of the local frame is shifted. Therefore, the planewave has the following form in the local frame:

$$e^{i(\mathbf{R}^\mu\mathbf{K})(\mathbf{r}+\mathbf{R}^\mu\mathbf{p}^\mu)} \tag{2.16}$$

Thus, the Rayleigh expansion of the planewave in the local frame is given by:

$$e^{i\mathbf{K}\mathbf{p}^\mu} \; 4\pi \sum_L i^l \; j_l(rK) \; Y_L^*(\mathbf{R}^\mu\hat{\mathbf{K}}) \; Y_L(\hat{\mathbf{r}}) \tag{2.17}$$

The requirement of continuity of the wavefunctions at the sphere boundary leads to the equation

$$\begin{aligned} &\sum_L A_L^{\mu\mathbf{G}}(\mathbf{k}) \; u_l(R_{MT^\alpha}) Y_L(\hat{\mathbf{r}}) + B_L^{\mu\mathbf{G}}(\mathbf{k}) \; \dot{u}_l(R_{MT^\alpha}) Y_L(\hat{\mathbf{r}}) \\ &= e^{i\mathbf{K}\mathbf{p}^\mu} \; 4\pi \sum_L i^l \; j_l(rK) \; Y_L^*(\mathbf{R}^\mu\hat{\mathbf{K}}) \; Y_L(\hat{\mathbf{r}}), \end{aligned} \tag{2.18}$$

where R_{MT^α} is the muffin-tin radius of the atom type α. The second requirement is, that the derivative with respect to r, denoted by $\partial/\partial r = \,'$, is also continuous

$$\begin{aligned} &\sum_L A_L^{\mu\mathbf{G}}(\mathbf{k}) \; u_l'(R_{MT^\alpha}) Y_L(\hat{\mathbf{r}}) + B_L^{\mu\mathbf{G}}(\mathbf{k}) \; \dot{u}_l'(R_{MT^\alpha}) Y_L(\hat{\mathbf{r}}) \\ &= e^{i\mathbf{K}\mathbf{p}^\mu} \; 4\pi \sum_L i^l \; K j_l'(rK) \; Y_L^*(\mathbf{R}^\mu\hat{\mathbf{K}}) \; Y_L(\hat{\mathbf{r}}). \end{aligned} \tag{2.19}$$

These conditions can only be satisfied, if the coefficients of each spherical harmonic $Y_L(\hat{\mathbf{r}})$ are equal. Solving the resulting equations for $A_L^{\mu\mathbf{G}}(\mathbf{k})$ and $B_L^{\mu\mathbf{G}}(\mathbf{k})$ yields:

$$\begin{aligned} A_L^{\mu\mathbf{G}}(\mathbf{k}) &= e^{i\mathbf{K}\mathbf{p}^\mu} 4\pi \frac{1}{W} i^l \; Y_L^*(\mathbf{R}^\mu\hat{\mathbf{K}}) \\ &\quad [\dot{u}_l(R_{MT^\alpha}) K j_l'(R_{MT^\alpha}K) - \dot{u}_l'(R_{MT^\alpha}) j_l(R_{MT^\alpha}K)] \\ B_L^{\mu\mathbf{G}}(\mathbf{k}) &= e^{i\mathbf{K}\mathbf{p}^\mu} 4\pi \frac{1}{W} i^l \; Y_L^*(\mathbf{R}^\mu\hat{\mathbf{K}}) \\ &\quad [u_l'(R_{MT^\alpha}) j_l(R_{MT^\alpha}K) - u_l(R_{MT^\alpha}) K j_l'(R_{MT^\alpha}K)] \end{aligned} \tag{2.20}$$

The Wronskian W is given by:

$$W = [\dot{u}_l(R_{MT^\alpha}) u_l'(R_{MT^\alpha}) - u_l(R_{MT^\alpha}) \dot{u}_l'(R_{MT^\alpha})] \tag{2.21}$$

Then one can show also that the FLAPW basis functions (eq. 2.9) can be transformed, for systems that possess inversion symmetry, into the following form

$$\varphi_{\mathbf{G}}(\mathbf{k},-\mathbf{r}) = \varphi^*_{\mathbf{G}}(\mathbf{k},\mathbf{r}) = \sum_{lm'} e^{-i\mathbf{K}(\mathbf{p}^{\mu})}\ (-i)^l\ Y_{lm'}(\mathbf{R}^{\mu}\hat{\mathbf{K}})\ Y^*_{lm'}(\hat{\mathbf{r}})\{Au_l(r) + B\dot{u}_l(r)\} \tag{2.22}$$

The Hamiltonian and overlap matrix will have the same property as the FLAPW basis functions in systems that possess inversion symmetry. These two matrices are real symmetric rather than complex hermitian. The Hamiltonian depends explicitly on $\mathbf{r}$ via the potential. The matrix elements are given by:

$$H^{\mathbf{G}'\mathbf{G}}(\mathbf{k}) = \int \varphi^*_{\mathbf{G}'}(\mathbf{k},\mathbf{r})\mathcal{H}(\mathbf{r})\varphi_{\mathbf{G}}(\mathbf{k},\mathbf{r}d^3r \tag{2.23}$$

Substituting $\mathbf{r}' = -\mathbf{r}$ yields:

$$H^{\mathbf{G}'\mathbf{G}}(\mathbf{k}) = \int \varphi_{\mathbf{G}'}(\mathbf{k},\mathbf{r}')\mathcal{H}(\mathbf{r}')\varphi^*_{\mathbf{G}}(\mathbf{k},\mathbf{r}')d^3r \tag{2.24}$$

where (2.22) and $\mathcal{H}(\mathbf{r}) = \mathcal{H}(-\mathbf{r})$ have been used. In addition the Hamiltonian operator is real, i.e. $\mathcal{H}(\mathbf{r}) = \mathcal{H}^*(\mathbf{r})$. Thus, we finally obtain:

$$\begin{aligned} H^{\mathbf{G}'\mathbf{G}}(\mathbf{k}) &= \int \varphi_{\mathbf{G}'}(\mathbf{k},\mathbf{r}')\mathcal{H}^*(\mathbf{r}')\varphi^*_{\mathbf{G}}(\mathbf{k},\mathbf{r}'d^3r \\ &= \left(H^{\mathbf{G}'\mathbf{G}}(\mathbf{k})\right)^*. \end{aligned} \tag{2.25}$$

The same relation holds for the overlap matrix. Because the two matrices are real, this means a great simplification in actual calculation. Then, the diagonalization of a hermitian matrix is no more difficult than in the real case. However, one complex multiplication contains four real multiplications, and therefore the complex problem is more "expensive" than the real, and the diagonalization needs the biggest part of the computing time in each iteration.

2.3.1 Film Calculations within FLAPW

Within the growing number of investigations in the area of thin films and surfaces, the ability to treat two dimensional systems becomes very important nowadays. In this case, either big spins allowed to be used or the basis set need to be reformed due to the broken translation symmetry in the perpendicular direction of the surface. Only the 2-dimensional symmetry parallel to the surface is left to be used to reduce the problem. For 10–15 atomic layers thickness, it is otherwise semi infinite to approximate surfaces by thin films. This approximation, called the thin-slab approximation, can only yield good results if the interaction between the two surfaces of the film is weak enough, so that each of them shows the properties of the surfaces of an ideal semi-infinite crystal.

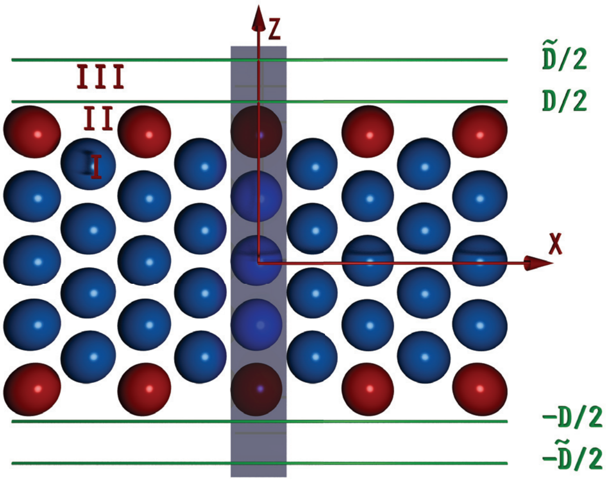

Figure 2.2: The unit cell in film calculations: (I) the muffin-tin spheres; (II) the interstitial region; the film is delimited on both sides by vacuum (III)

In the case of film calculations space is divided into three distinct regions, the muffin-tins, the interstitial and the vacuum region (Fig. 2.2). The interstitial region now stretches from $-\tilde{D}/2$ to $\tilde{D}/2$ in z-direction, which is defined to be the direction perpendicular to the film. The representation of the wavefunctions inside the muffin-tin spheres remains exactly the same as in the bulk case. Since the periodicity along the z-direction is lost, the unit cell extends in principle from $-\infty$ to ∞ in z-direction. Still the wavefunctions in the interstitial can be expanded in terms of planewaves. Therefore, the planewaves have the form

$$\varphi_{\mathbf{G}_\parallel G_\perp}(\mathbf{k}_\parallel, \mathbf{r}) = e^{i(\mathbf{G}_\parallel + \mathbf{k}_\parallel)\cdot \mathbf{r}_\parallel} \; e^{iG_\perp z} \tag{2.26}$$

with

$$G_\perp = \frac{2\pi n}{\tilde{D}} \tag{2.27}$$

where $\mathbf{G}_\parallel$ and $\mathbf{k}_\parallel$ are the 2-dimensional wave- and Bloch vectors, $\mathbf{r}_\parallel$ is the parallel component of $\mathbf{r}$ and $G_\perp$ is the wavevector perpendicular to the film. The basis functions in the vacuum region beyond $(\pm D/2)$ are constructed in the same spirit as the functions in the muffin-tins [79]. They consist of planewaves parallel to the film, and a z-dependent function $u_{\mathbf{G}_\parallel}(\mathbf{k}_\parallel, z)$, which solves the corresponding 1-dimensional Schrödinger equation, plus the energy derivative $\dot{u}_{\mathbf{G}_\parallel}(\mathbf{k}_\parallel, z)$

$$\left\{ -\frac{1}{2}\frac{\partial^2}{\partial z^2} + V_0(z) - E_{vac} + \frac{1}{2}(\mathbf{G}_\parallel + \mathbf{k}_\parallel)^2 \right\} u_{\mathbf{G}_\parallel}(\mathbf{k}_\parallel, z) = 0 \tag{2.28}$$

E_{vac} is the vacuum energy parameter and $V_0(z)$ is the planar averaged part of the vacuum potential. As in the case of $\dot{u}_l$ in the muffin-tins, the function $\dot{u}_{\mathbf{G}_\parallel}(\mathbf{k}_\parallel, z)$ is calculated from a Schrödinger-like equation, which can be obtained by deriving (2.28) with respect to the energy.

$$\left\{-\frac{1}{2}\frac{\partial^2}{\partial z^2} + V_0(z) - E_{vac} + \frac{1}{2}(\mathbf{G}_\parallel + \mathbf{k}_\parallel)^2\right\} \dot{u}_{\mathbf{G}_\parallel}(\mathbf{k}_\parallel, z) = u_{\mathbf{G}_\parallel}(\mathbf{k}_\parallel, z) \tag{2.29}$$

The resulting basis functions have the form

$$\varphi_{\mathbf{G}_\parallel G_\perp}(\mathbf{k}_\parallel, \mathbf{r}) = \left\{A_{\mathbf{G}_\parallel G_\perp}(\mathbf{k}_\parallel) u_{\mathbf{G}_\parallel}(\mathbf{k}_\parallel, z) + B_{\mathbf{G}_\parallel G_\perp}(\mathbf{k}_\parallel) \dot{u}_{\mathbf{G}_\parallel}(\mathbf{k}_\parallel, z)\right\} \; e^{i(\mathbf{G}_\parallel + \mathbf{k}_\parallel)\mathbf{r}_\parallel} \tag{2.30}$$

The coefficients $A_{\mathbf{G}_\parallel G_\perp}(\mathbf{k}_\parallel)$ and $B_{\mathbf{G}_\parallel G_\perp}(\mathbf{k}_\parallel)$ are determined by requiring that the functions are continuous and differentiable at the vacuum boundary. Instead of the energy parameter E_{vac}, a whole series of $G_\perp$-dependent energy parameters, $E^i_{vac} = E^{G_\perp}_{vac} = E_{vac} - \frac{1}{2}G^2_\perp$ can be used to increase the variational freedom in the vacuum basis functions [80].

Finally, the basis set used for thin film calculations with the FLAPW method has the form

$$\varphi_{\mathbf{G}_\parallel G_\perp}(\mathbf{k}_\parallel, \mathbf{r}) = \begin{cases} e^{i(\mathbf{G}_\parallel + \mathbf{k}_\parallel)\mathbf{r}_\parallel} \; e^{iG_\perp z} & \text{Int.} \\ \Big\{A_{\mathbf{G}_\parallel G_\perp}(\mathbf{k}_\parallel) u_{\mathbf{G}_\parallel}(\mathbf{k}_\parallel, z) & \\ +B_{\mathbf{G}_\parallel G_\perp}(\mathbf{k}_\parallel) \dot{u}_{\mathbf{G}_\parallel}(\mathbf{k}_\parallel, z)\Big\} \, e^{i(\mathbf{G}_\parallel + \mathbf{k}_\parallel)\mathbf{r}_\parallel} & \text{Vac.} \\ [\sum_L A^{\mu\mathbf{G}}_L(\mathbf{k}) u_l(r) + B^{\mu\mathbf{G}}_L(\mathbf{k}) \dot{u}_l(r)] Y_L(\hat{\mathbf{r}}) & \text{MT } \mu. \end{cases} \tag{2.31}$$

2.4 The Kohn-Sham-Dirac Equation

Close to the nucleus, where the kinetic energy is large, the relativistic effects are significant. This means the electrons inside the muffin-tins should be treated relativistically, where it is reasonable to treat the interstitial region and the vacuum non-relativistically. This makes the Kohn-Sham equation to be as single particle Dirac equation

$$\left\{c\underline{\alpha} \cdot \mathbf{p} + (\underline{\beta} - \underline{1})mc^2 + V^{eff}(\mathbf{r})\right\} \mathbf{\Psi} = E\mathbf{\Psi} \tag{2.32}$$

$$\underline{\tilde{\alpha}} = \left(\begin{pmatrix} 0 & \underline{\sigma_x} \\ \underline{\sigma_x} & 0 \end{pmatrix}, \begin{pmatrix} 0 & \underline{\sigma_y} \\ \underline{\sigma_y} & 0 \end{pmatrix}, \begin{pmatrix} 0 & \underline{\sigma_z} \\ \underline{\sigma_z} & 0 \end{pmatrix} \right)^{tr} = \begin{pmatrix} 0 & \underline{\tilde{\sigma}} \\ \underline{\tilde{\sigma}} & 0 \end{pmatrix} \tag{2.33}$$

$$\beta = \begin{pmatrix} \underline{I}_2 & 0 \\ 0 & -\underline{I}_2 \end{pmatrix} \tag{2.34}$$

σ_x σ_y σ_z are the Pauli matrices and σ is the vector of Pauli matrices, $\mathbf{p}$ is the momentum operator, and I_n denotes an $(n \times n)$ unit matrix. V^{eff} is the effective potential, that contains electron-nucleon Coulomb potential, Hartree potential and exchange-correlation potential. In the case of non-zero spin-polarization, V^{eff} becomes spin-dependent. Finally, $\mathbf{\Psi}$ is the relativistic four component wavefunction.

The straightforward way to solve this problem would be to expand each of the four components of $\mathbf{\Psi}$ in terms of the FLAPW basis. If all four components were treated with the same accuracy, this would result in a basis set which contains four times as many functions as in the non-relativistic (non-magnetic) case. Numerically, the effort of the Hamiltonian diagonalization scales with the dimension of the matrix to the power of three, this means that the computing time needed for the diagonalization will increase by a factor of 64.

Only the large component of $\mathbf{\Psi}$ is matched in the non-relativistic wavefunctions at the boundary between the muffin-tins and the interstitial region. This is because the small component is already negligible at this distance from the nucleus. The small component cannot be varied independently, because it is attached to the large component. However, this approximation is sensible for two reasons: Firstly even inside the muffin-tin sphere the large component is still much bigger than the small component, and plays the more important role, and secondly the two components are determined by solving the scalar relativistic equations for the spherically averaged potential. Therefore, they are very well suited to describe the wavefunctions.

Hence, the size of the basis set and the Hamiltonian matrix remains the same as in non-relativistic calculations, but the problem has to be solved twice, once for each direction of spin. This amounts to a numerical effort, that is equal to that needed in spin-polarized non-relativistic calculations.

2.4.1 The Scalar Relativistic Approximation

Some approximations can be implemented via the FLAPW to make relativistic calculations more efficient. One of these approximations is the scalar relativistic approximation, which has been suggested by D.D. Kölling and B.N. Harmon [81]. In this approximation, the spin-orbit term is neglected, then the spin and spatial coordinates become decoupled. This reduces the Hamiltonian matrix into two matrices of half the size, which can be diagonalized separately. This approximation saves a factor of four in computing time.

When the electrons are only treated relativistically inside the muffin-tin spheres, the first problem is how to construct the relativistic radial function. This is done by solving the scalar relativistic equation, including only the spherically averaged part of the potential. The solution of Dirac equation (2.32) is discussed in many textbooks like reference [82]. Due to spin-orbit coupling m and m_s are not good quantum numbers any more, and they have to be replaced by the quantum numbers κ and μ (or j and μ), which are eigenvalues of the operators K and the z-component of the total angular momentum j_z (or the total angular momentum $\mathbf{j}$ and j_z) respectively. K is defined by

$$K = \beta(\sigma \cdot \mathbf{l} + 1) \tag{2.35}$$

The solutions of (2.32) have the form

$$\mathbf{\Psi} = \mathbf{\Psi}_{\kappa\mu} = \begin{pmatrix} g_\kappa(r)\chi_{\kappa\mu} \\ i f_\kappa(r)\chi_{-\kappa\mu} \end{pmatrix}, \tag{2.36}$$

where $g_\kappa(r)$ is the large component, $f_\kappa(r)$ is the small component, $\chi_{\kappa\mu}$ and $\chi_{-\kappa\mu}$ are spin angular functions, which are eigenfunctions of $\mathbf{j}$, j_z, K and $\mathbf{s}^2$ with eigenvalues j, μ, κ ($-\kappa$) and $s = 1/2$ respectively. The spin angular functions can be expanded into a sum of products of spherical harmonics and Pauli spinors, where the expansion coefficients are the Clebsch-Gordon coefficients. The radial functions have to satisfy the following set of coupled equations.

$$\begin{pmatrix} -\frac{\kappa+1}{r} - \frac{\partial}{\partial r} & 2Mc \\ \frac{1}{c}(V(r) - E) & \frac{\kappa-1}{r} - \frac{\partial}{\partial r} \end{pmatrix} \begin{pmatrix} g_\kappa(r) \\ f_\kappa(r) \end{pmatrix} = 0 \tag{2.37}$$

with

$$M = m + \frac{1}{2c^2}(E - V(r)). \tag{2.38}$$

To derive the scalar relativistic approximation D.D. Kölling and B.N. Harmon [81] introduced the following transformation.

$$\begin{pmatrix} g_\kappa(r) \\ \varphi_\kappa(r) \end{pmatrix} = \begin{pmatrix} 1 & 0 \\ \frac{1}{2Mc}\frac{\kappa+1}{r} & 1 \end{pmatrix} \begin{pmatrix} g_\kappa(r) \\ f_\kappa(r) \end{pmatrix} \tag{2.39}$$

Using this transformation (2.37) becomes

$$\begin{pmatrix} -\frac{\partial}{\partial r} & 2Mc \\ \frac{1}{2Mc}\frac{l(l+1)}{r^2} + \frac{1}{c}(V(r) - E) + \frac{\kappa+1}{r}\frac{M'}{2M^2c} & -\frac{2}{r} - \frac{\partial}{\partial r} \end{pmatrix} \begin{pmatrix} g_\kappa(r) \\ \varphi_\kappa(r) \end{pmatrix} = 0, \tag{2.40}$$

where M' is the derivative of M with respect to r ($\partial M/\partial r$), and the identity $\kappa(\kappa+1) = l(l+1)$ has been used. Recalling, that κ is the eigenvalue of $K = \beta(\sigma \cdot \mathbf{l} + 1)$ the term $(\kappa+1)M'/2M^2cr$ can be identified as the spin-orbit term. This term is dropped in the scalar relativistic approximation, because it is the only one, that causes coupling of spin up and spin down contributions. The radial functions $g_l(r)$ and $\varphi_l(r)$ (the index κ has been replaced by l) can now be calculated from the following set of differential equations.

$$\begin{aligned} \frac{\partial}{\partial r} g_l(r) &= 2Mc\varphi_l(r) && (2.41) \\ \frac{\partial}{\partial r} \varphi_l(r) &= \left(\frac{1}{2Mc} \frac{l(l+1)}{r^2} + \frac{1}{c}(V(r) - E) \right) g_l(r) - \frac{2}{r}\varphi_l(r) && (2.42) \end{aligned}$$

The energy derivative of these yields a set of equations for $\dot{g}_l(r)$ and $\dot{\varphi}_l(r)$, which are the relativistic analog of $\dot{u}_l(r)$. For numerical reasons the functions $g_l(r)$ and $\varphi_l(r)$ are replaced by $p_l(r) = rg_l(r)$ and $q_l(r) = cr\varphi_l(r)$. In the implementation of FLAPW, the radial wavefunctions are normalized according to

$$\left\langle \begin{pmatrix} g_l \\ \varphi_l \end{pmatrix} \middle| \begin{pmatrix} g_l \\ \varphi_l \end{pmatrix} \right\rangle = \int_0^{R_{MT}} (g_l^2(r) + \varphi_l^2(r)) r^2 dr = 1 \qquad (2.43)$$

The energy derivatives of the radial functions have to be made orthogonal to the radial functions.

$$\left\langle \begin{pmatrix} g_l \\ \varphi_l \end{pmatrix} \middle| \begin{pmatrix} \dot{g}_l \\ \dot{\varphi}_l \end{pmatrix} \right\rangle = 0 \qquad (2.44)$$

Thus, the scalar relativistic FLAPW basis set is

$$\varphi_{\mathbf{G}_\parallel G_\perp}(\mathbf{r}) = \begin{cases} \dfrac{1}{\sqrt{\Omega}} \, e^{i(\mathbf{G}_\parallel + \mathbf{k}_\parallel)\mathbf{r}_\parallel} \, e^{iG_\perp z} & Int. \\ \left\{ A_{\mathbf{G}_\parallel G_\perp} u_{\mathbf{G}_\parallel}(z) + B_{\mathbf{G}_\parallel G_\perp} \dot{u}_{\mathbf{G}_\parallel}(z) \right\} \, e^{i(\mathbf{G}_\parallel + \mathbf{k}_\parallel)\mathbf{r}_\parallel} & Vac. \\ \sum\limits_{\substack{\alpha \\ lm}} A_{lm}^{\alpha\mathbf{Gk}} \begin{pmatrix} g_l(r) \\ \varphi_l(r) \end{pmatrix} Y_{lm}(\hat{\mathbf{r}}) + B_{lm}^{\alpha\mathbf{Gk}} \begin{pmatrix} \dot{g}_l(r) \\ \dot{\varphi}_l(r) \end{pmatrix} Y_{lm}(\hat{\mathbf{r}}) & MT \end{cases} \qquad (2.45)$$

Note that the Pauli-spinors have been omitted, since the spin up and down problems are solved independently within the scalar relativistic approximation. Rewriting (2.40)

$$\mathcal{H}_{SP} \begin{pmatrix} g_l(r) \\ \varphi_l(r) \end{pmatrix} = E \begin{pmatrix} g_l(r) \\ \varphi_l(r) \end{pmatrix} \qquad (2.46)$$

with

$$\mathcal{H}_{SP} = \begin{pmatrix} \dfrac{1}{2M} \dfrac{l(l+1)}{r^2} + V(r) & -\dfrac{2c}{r} - c\dfrac{\partial}{\partial r} \\ c\dfrac{\partial}{\partial r} & -2mc^2 + V(r) \end{pmatrix} \qquad (2.47)$$

a matrix expression for the scalar relativistic Hamiltonian including only the spherically averaged part of the potential can be obtained. For completeness, the radial charge density is defined by

$$\rho_l(r) = \left\langle \left(\begin{array}{c} g_l \\ f_l \end{array} \right) \middle| \left(\begin{array}{c} g_l \\ f_l \end{array} \right) \right\rangle = \int_0^{R_{MT}} (g_l^2(r) + f_l^2(r)) r^2 dr. \tag{2.48}$$

Chapter 3

Magnetism of low dimensional systems

Materials can be classified according to their magnetic susceptibility, which is the measure of the material response to an externally applied magnetic fields. Diamagnetic materials have localized moments which do not contribute in the materials magnetic response, even to an external applied magnetic field, and by that they have negative magnetic susceptibility. Paramagnetic materials are non-magnetic, with zero net magnetization, but can be magnetized by inducing their moments through an external magnetic field. Materials which are spontaneously magnetized without being in an external magnetic field are called magnetic materials. In magnetic materials, the spin split states enhance a net magnetization to occur. They are classified according to their spin moments arrangement, for example, magnetic materials with spins aligned in parallel (ferromagnetic) or anti-parallel (anti-ferromagnetic) to each other are called collinear, while non-collinear magnetic material has its spins aligned by a certain angle with respect to each other in the three dimensional space[83, 84, 85].

Metals exhibits conduction electrons which are delocalized. These itinerant electrons can move nearly free inside the metal. This means that metals might be paramagnetic, or magnetic. Among all the transition metals, only Fe, Co, and Ni are magnetic in their bulk phase, but when we go to lower dimensions, the physics changes and many paramagnetic metals become magnetic[86]. Many theories and models were introduced to understand magnetic materials in low dimensional systems. In this chapter, we chosen to explain the most dominant classical models to describe magnetic interactions: Stoner and the classical Heisenberg model. In the first section of this chapter, we will describe the Stoner model, since it is used to describe the ferro- and anti-ferromagnetic materials in terms of nearest neighbor exchange interactions[86, 51, 52, 54, 53, 87]. Where the classical Heisenberg model will be explained in the second section, since it is normally used to describe magnetic interactions by going beyond the nearest neighbor interactions to describe non-collinear magnetic systems[88, 89, 90, 91, 92]. In the last section of this chapter, we will present the theory of magnetic anisotropy energy (MAE) in low dimensional system, since it is responsible about stabilizing the magnetic order at finite temperatures[86, 93, 94, 55, 95].

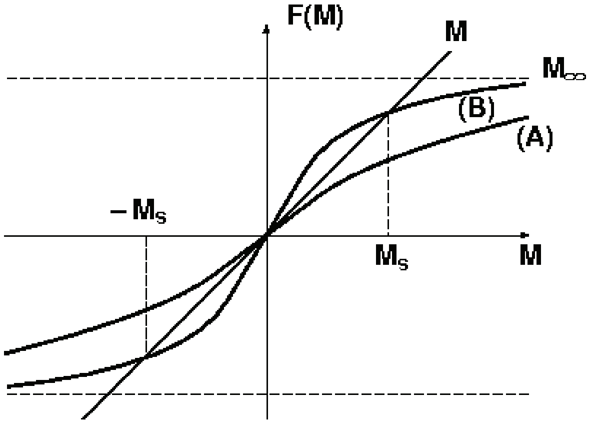

Figure 3.1: Graphical solution of (3.10).

3.1 Stoner Model

The one–particle nature of the Kohn–Sham equation makes it possible to derive a Stoner like theory for ferromagnetism [51, 52, 53, 54]. Within the spin-density functional theory, the magnetization density of solids is usually defined to be the difference between the majority and minority spin densities, $|\mathbf{m}(\mathbf{r})| = n^{\uparrow} - n^{\downarrow}$. It is small compared to the electron density, $n(\mathbf{r}) = n^{\uparrow} + n^{\downarrow}$. Expanding the exchange correlation energy $E_{\mathrm{xc}}(n(\mathbf{r}), m(\mathbf{r}))$ into a Taylor series in terms of the parameter $\xi = m/n$ yields

$$E_{\mathrm{xc}}(n,\xi) = E_{\mathrm{xc}}(n,0) + \frac{1}{2}E''_{\mathrm{xc}}(n,0)\xi^2 + \cdots \tag{3.1}$$

On taking the derivative of the exchange-correlation energy with respect to spin-up and spin-down densities,

$$\begin{aligned} n^{\uparrow} &= (n+m)/2 \simeq n(1+\xi)/2 \\ n^{\downarrow} &= (n-m)/2 \simeq n(1-\xi)/2, \end{aligned} \tag{3.2}$$

the exchange-correlation potential for the two spin directions becomes

$$V_{xc}^{\uparrow(\downarrow)}(\mathbf{r}) = V_{\mathrm{xc}}^{\pm}(\mathbf{r}) = V_{\mathrm{xc}}^{0}(\mathbf{r}) \mp \tilde{V}_{\mathrm{xc}}(\mathbf{r})m(\mathbf{r}) \tag{3.3}$$

(with (+) for ↑ and (−) for ↓), where

$$\begin{aligned} V^0_{\mathrm{xc}} &= \epsilon_{\mathrm{xc}}(n,0) + n\frac{\partial E_{\mathrm{xc}}(n,0)}{\partial n} \\ \tilde{V}_{\mathrm{xc}} &= \frac{1}{n^2}\frac{\partial^2 E_{\mathrm{xc}}(n,0)}{\partial m^2} m. \end{aligned} \tag{3.4}$$

In the Stoner model this potential shift is expressed in terms of a constant:

$$V^{\pm}_{\mathrm{xc}}(\mathbf{r}) = V^0_{\mathrm{xc}}(\mathbf{r}) \mp \frac{1}{2}IM \qquad M = \int_{V_{\mathrm{atom}}} m(\mathbf{r})d\mathbf{r}\ . \tag{3.5}$$

M is the total magnetic moment per atom, and I is the exchange integral (Stoner parameter). Because of this constant shift the spatial shape of the potential remains the same as in the nonmagnetic case. Consequently, the solutions of the Kohn-Sham equations also remain unchanged, only the single particle energies ε_i are shifted by the same amount $\mp IM/2$,

$$\psi^{\pm}_i(\mathbf{r}) = \psi^0_i(\mathbf{r}), \qquad \epsilon^{\pm}_i = \epsilon^0_i \mp \frac{1}{2}IM \tag{3.6}$$

Hence, the whole band structure is spin-split and the shape of the bands remains unaltered. As a result, the local densities of states (LDOS) projected on an atom for the spin-directions, $n^{\pm}(\epsilon)$, are also shifted by $\mp IM/2$.

$$n^{\pm}(\epsilon) = n(\epsilon \pm \frac{1}{2}IM)\ . \tag{3.7}$$

From this property of the DOS a criterion for the existence of ferromagnetism can be derived. Integrating the density of states up to the Fermi energy E_{F} yields the number of electrons N and the total magnetic moment per atom M.

$$N = \int_{\epsilon<E_{\mathrm{F}}} \left[n(\epsilon + \frac{1}{2}IM) + n(\epsilon - \frac{1}{2}IM)\right] d\epsilon \tag{3.8}$$

$$M = \int_{\epsilon<E_{\mathrm{F}}} \left[n(\epsilon + \frac{1}{2}IM) - n(\epsilon - \frac{1}{2}IM)\right] d\epsilon\ . \tag{3.9}$$

The charge neutrality requirement embodied in (3.8) determines the unknown Fermi energy and this, inturn, determines the magnetic moment. Requiring charge neutrality the first equation can be used to obtain the Fermi energy as a function of the magnetization $E_{\mathrm{F}} = E_{\mathrm{F}}(M)$. Substituting this into the second equation leads to a self consistency problem for M.

$$\begin{aligned} M &= F(M), \qquad \text{with} \\ F(M) &= \int_{\epsilon<E_{\mathrm{F}}(M)} \left[n(\epsilon + \frac{1}{2}IM) - n(\epsilon - \frac{1}{2}IM)\right] d\epsilon\ . \end{aligned} \tag{3.10}$$

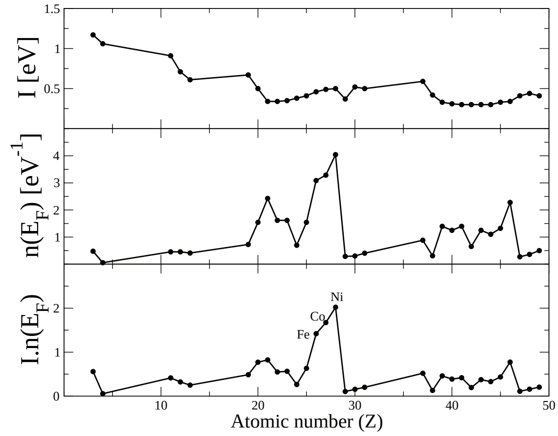

Figure 3.2: Values of the Stoner parameter, (paramagnetic) density of states per atom $n(E_\mathrm{F})$ at the Fermi energy, and $In(E_F)$ as a function of the atomic number Z. Only the elements Fe, Co, and Ni fulfill the Stoner criterion and are ferromagnetic. All results are obtained with the density functional theory in the local density approximation [52, 53].

The function $F(M)$ is odd in M, therefore $F(0) = 0$ and $F(M) = -F(-M)$. It is a monotonically increasing function, i.e. $F'(0) > 0$, and saturates at the largest possible magnetization $\pm M_\infty = F(\pm\infty)$. A graphical solution of (3.10) is illustrated in Fig. 3.1.

Two functions $F(M)$, consistent with the above properties, are plotted. In case A only the trivial nonmagnetic solution $M = 0$ is present, whereas in case B three solutions exist, two of which have non-zero magnetization. From the properties of $F(M)$ follows that (3.10) always has solutions with non-zero magnetization, if the slope of $F'(0) = I\,n(E_\mathrm{F}) > 1$. This is finally the Stoner criterion for ferromagnetism:

$$I\,n(E_\mathrm{F}) \;>\; 1\;. \tag{3.11}$$

The Stoner criterion is an instability condition which expresses the competition between the exchange interaction in terms of the exchange integral I which drives the system into ferromagnetism for large I and the kinetic energy in terms of the DOS, the more kinetic energy the wider the band width or the lower the density of states. A big exchange integral and a large nonmagnetic DOS at the Fermi energy favors ferromagnetism. Figure 3.2 shows the exchange integral I, the local DOS at the Fermi energy $n(E_\mathrm{F})$ derived from nonmagnetic calculations and the product $In(E_\mathrm{F})$ for a number of elemental metals. It shows, that the Stoner condition for ferromagnetism is only fulfilled for Fe, Co, and Ni, precisely those metals that show itinerant ferromagnetism.

3.1.1 Role of coordination number:

The Stoner criterion for ferromagnetism, equation (3.11), depends on the Stoner parameter I and the nonmagnetic density of states at Fermi energy $n(E_{\mathrm{F}})$. The exchange integral I is an atomic property, element specific quantity, and independent of the local environment, the structure and the site of a given atom.

The exchange integrals, of the $3d$, $4d$, and $5d$ transition metals, posses a global trend[52, 53]:

$$I_{3d} > I_{4d} > I_{5d} \tag{3.12}$$

For the d electrons are relevant electrons to study for itinerant magnetism. On the other hand, the density of states depends on the coordination number N_{nn} and the hopping matrix elements h_d between the d electrons. The energy integral over band width, W, of the local DOS of angular momentum quantum number ($l = 2$) for d-electrons is normalized to $2l + 1$:

$$\int_W n_l(\varepsilon) d\varepsilon = 2l + 1 \tag{3.13}$$

As as simplest approximation, it is possible that the local DOS scales inversely proportional to the band width:

$$n(E_{\mathrm{F}}) \approx \frac{1}{W} \tag{3.14}$$

At the atomic limit, the band width converges to zero and the Stoner criterion will be always fulfilled and moments in accordance with Hund's first rule will be found. For transition metals the largest contribution to the local DOS comes from the d electrons, then d-d hybridization determines the shape of the density of states. Therefore, the local DOS can be approximated to

$$n(E_{\mathrm{F}}) \approx n_d(E_{\mathrm{F}}) \approx \frac{1}{W_d} \tag{3.15}$$

By that, the average local band width $\overline{W}_d(\vec{R}_i)$ for an atom i at position $\vec{R}_i$ can be estimated in a nearest neighbor tight-binding model:

$$W_d \approx W_d(\vec{R}_i) = 2\sqrt{N_{nn}(\vec{R}_i)} h_d(R_{nn}) \tag{3.16}$$

From this equation we see that the band width depends on the hopping matrix element h_d of the d-electrons and the number of nearest neighbor atoms, N_{nn}, called the coordination number. The hopping matrix element depends on the overlap of the d wavefunctions. It decreases with increasing lattice constant or distance to the nearest neighbor atom, R_{nn}. For a given lattice constant it increases with the extension of the wavefunction or, equivalently, the number of nodes. In line with the arguments of increasing number of nodes from $3d$- to $5d$-wavefunctions, a clear "macro trend" between the transition-metal series is visible:

$$h_{3d} < h_{4d} < h_{5d} \Rightarrow W_{3d} < W_{4d} < W_{5d} \Rightarrow n_{3d} > n_{4d} > n_{5d} \tag{3.17}$$

An additional "micro trend" does exist in the same transition-metal series: due to the incomplete screening of the Coulomb potential of the nucleus by the d-electrons, the d-wavefunctions at the beginning of the transition-metal series are more extent than at the end of the series. This means that the hopping matrix element at the beginning of the series is larger than at the end, with the consequences for the band width W and the DOS $n(E_{\mathrm{F}})$. From equation (3.16), the smaller the coordination number N_{nn} the smaller the d-d hybridization and the smaller is the band width. The coordination number of an atom in the environment of a fcc crystal, N^{fcc}, is 12, and 8 for an atom in the (001)-surface of the fcc crystal, $N^{(001)}$. For an atom located in a two-dimensional (001) monolayer film, $N^{ML} = 4$, and of an atom in a monoatomic chain, $N^{chain} = 2$. If the nearest neighbor distance R_{nn} and the bonding strength h_d are fixed to be constants, one will obtain the ratio of the band widths to be:

$$W_d^{chain} : W_d^{ML} : W_d^{(001)} : W_d^{fcc} = 0.41 : 0.58 : 0.82 : 1 \tag{3.18}$$

or the local DOS

$$n_d^{chain} : n_d^{ML} : n_d^{(001)} : n_d^{fcc} = 2.45 : 1.73 : 1.22 : 1 \tag{3.19}$$

3.2 Heisenberg Model and Beyond

To predict the magnetic ground state of a magnetic system can be a highly nontrivial problem. In cases, for example, where competing exchange interactions between neighboring atoms cannot be satisfied, the exchange interaction is frustrated which gives rise to a multitude of possible spin-structures. In the past, the magnetism of complex spin structures of itinerant magnets has been almost exclusively discussed within the framework of model Hamiltonians, e.g. the classical Heisenberg Hamiltonian,

$$H_{2\text{-spin}} = -\sum_{\substack{i,j \\ i>j}} J_{ij}\ \mathbf{M}_i \cdot \mathbf{M}_j\ . \tag{3.20}$$

The magnetic moments ($\vec{M} = \mu_B \vec{S}$) localized on the lattice sites i, j are considered as classical vectors $\mathbf{M}$, with the assumption that their magnitudes M are constant. The exchange interaction between the magnetic moments is described by the pair interaction J_{ij}. In localized spin systems the J_{ij} can be safely restricted to the ferromagnetic ($J_1 > 0$) or antiferromagnetic ($J_1 < 0$) nearest-neighbor (n.n.) interaction, i.e. $J_{ij} = 0$ for all i, j, except for $J_{n.n.} = J_1$. Also in itinerant magnets J_1 often dominates over the rest of the further distant pairs. However, an attempt to reproduce the critical Curie temperature,

T_C, solely from J_1 produces results of limited validity as will be seen in next, magnetic anisotropy, section.

Exchange interactions beyond the classical Heisenberg model can be motivated from a perturbation expansion of the Hubbard model [36]. Expanding the Hubbard model into a spin model, replacing the spin operators by classical spin vectors, a second order perturbation expansion reproduces the classical Heisenberg model. The fourth order perturbation treatment (the third order is zero in the absence of spin-orbit interaction) yields two additional terms of different form. One is the four-spin exchange interaction (4-spin):

$$H_{4\text{-spin}} = -\sum_{ijkl} K_{ijkl} \big[(\mathbf{M}_i\mathbf{M}_j)(\mathbf{M}_k\mathbf{M}_l) + (\mathbf{M}_j\mathbf{M}_k)(\mathbf{M}_l\mathbf{M}_i) - (\mathbf{M}_i\mathbf{M}_k)(\mathbf{M}_j\mathbf{M}_l)\big].$$

The 4-spin interaction arises from the hopping of electrons over four sites, i.e. the process 1 → 2 → 3 → 4 → 1. Another term, resulting from the hopping 1 → 2 → 1 → 2 → 1, is the bi-quadratic exchange:

$$H_{\text{biquadr}} = -\sum_{ij} B_{ij}(\mathbf{M}_i \cdot \mathbf{M}_j)^2. \tag{3.21}$$

The exchange parameters J_{ij}, K_{ijkl}, and B_{ij} depend on the details of the electronic structure and it is known [87] that for transition-metals the sign and magnitude are rapidly varying functions of the d-band filling. For Bravais lattice, the solution of Heisenberg model is flat spin-spirals, with propagation vector $\mathbf{Q}$ in the first Brillouin Zone (BZ). Then it becomes convenient to write the spin on N crystal lattice sites in terms of their Fourier components $\vec{M}_{\mathbf{Q}}$

$$H_{2\text{-spin}} = -N \sum_{\mathbf{Q}} J(\mathbf{Q})\ \mathbf{M}_{\mathbf{Q}} \cdot \mathbf{M}_{-\mathbf{Q}}\ . \tag{3.22}$$

By this description, the superposition of two or three $\mathbf{Q}$ spirals, which are separated by one lattice vector, becomes degenerate with each chosen $\mathbf{Q}$-point to construct the new state. In thin films, $M^4\,K_1$ and $M^4\,B_1$ are about one order of magnitude smaller than $M^2 J_1$Then the higher order spin interactions have the effect, depending on the sign and value, of splitting magnetic states which are degenerate when described by the 2-spin Heisenberg model as we will see in chapter (5).

In itinerant magnets, the electrons that are responsible for the formation of the magnetic state do participate in the formation of the Fermi-surface and hop across the lattice. Thus, it is by no means clear how far a short-ranged n.n. interaction or even how far the Heisenberg model, and models beyond that, can go in giving a sufficiently good description of the physics of itinerant magnets at surfaces and films. We believe that the combination of ab-initio calculations and the study of model Hamiltonians provides a powerful approach to investigate the magnetic structures of complex magnetic systems.

3.3 Non-Collinear Magnetism

The energy functional of a general magnetic system can be expressed in two ways, as a functional of the charge density n and the magnetization density vector field $\mathbf{m}$, or as a functional of the hermitian 2×2 density matrix $\underline{\rho}$. The two formulations are completely equivalent. The density matrix is defined by the following equation:

$$\underline{\rho} = \frac{1}{2}\, n\, \mathbf{I}_2 + \sigma \cdot \mathbf{m} = \frac{1}{2} \begin{pmatrix} n + m_z & m_x - i m_y \\ m_x + i m_y & n - m_z \end{pmatrix}. \tag{3.23}$$

where, σ is the Pauli spin space matrix. The potential matrix can be defined in the same way,

$$\underline{V} = V\, \mathbf{I}_2 + \mu_B\, \sigma \cdot \mathbf{B} = \begin{pmatrix} V + \mu_B B_z & \mu_B (B_x - i B_y) \\ \mu_B (B_x + i B_y) & V - \mu_B B_z \end{pmatrix}. \tag{3.24}$$

The components of the density matrix are given in terms of the solutions of the Kohn-Sham equation:

$$\rho_{\alpha\beta} = \sum_{i=1}^{N} \psi^*_{i,\alpha} \psi_{i,\beta}. \tag{3.25}$$

where, $\psi_{i,\alpha} \equiv \begin{pmatrix} \phi_i^{\uparrow}(\mathbf{r}) \\ \phi_i^{\downarrow}(\mathbf{r}) \end{pmatrix}$ are Pauli wave functions that reproduce the electron and the magnetization density.

In an actual implementation of non-collinear magnetism in a computer program these matrix quantities are very useful, though they are less intuitive than the "physical" quantities n, $\mathbf{m}$, V, and $\mathbf{B}$.

Using the potential matrix (3.24), the Kohn-Sham equation becomes

$$\left\{ -\frac{\hbar^2}{2m} \nabla^2\, \mathbf{I}_2 + \underline{\mathbf{V}} \right\} \psi_i = \epsilon_i \psi_i. \tag{3.26}$$

The kinetic energy part of the Hamiltonian is diagonal in the two spin directions. It is only the off-diagonal part of the hermitian 2×2 potential matrix, e.g. $V_{21} = \mu_B (B_x + i B_y)$, that couples the two components of the Pauli spinor ψ_i. If the B-field is collinear, the spin coordinate frame can always be chosen such that the B-field points in the spin z-direction. In this case V_{21}, and thus the off-diagonal part of the Hamiltonian, becomes zero, because B_x and B_y are zero. The notation $V_\uparrow = V + \mu_B B_z$, $V_\downarrow = V - \mu_B B_z$ is commonly used for the diagonal elements of $\underline{V}$ in the collinear case. Since the two spin directions become completely independent, the spin-up and down problem can be solved separately in two steps. Each step can be treated like the non-magnetic problem with the appropriate potential $V_\uparrow$ or $V_\downarrow$. In practice this means that extending a non-magnetic ab-initio program to collinear magnetism is rather straight forward. In addition collinear calculations are by far less costly than non-collinear ones. Since the effort required to diagonalize the Hamiltonian matrix scales with the number of basis functions to the third power, diagonalizing two small matrices for each spin is much faster than diagonalizing one matrix of twice the size. It also requires only 1/4 of the memory to store the matrix. Another advantage arises when the collinear system has inversion symmetry. In that case the Hamiltonian and the overlap matrix become real symmetric rather than complex hermitian. In general non-collinear calculation, the Hamiltonian matrix is always complex, due to the complex Pauli matrix σ_y, i.e. the term $i\mu_B B_y$ in V_{21}. A third point is, that in most cases non-collinearity reduces the symmetry. The consequence is, that the area of the irreducible part of the Brillouin zone increases. The computational effort increases linearly with the number of k-points that have to be taken into account for the Brillouin zone integration. So far most magnetic calculations have been performed for collinear systems, because such calculations are more simple and significantly less time consuming.

3.3.1 The Spin Space Groups

The spin-orbit coupling and the dipole interaction, which is usually treated classically, are the only terms in the Hamiltonian that couple real space and spin space. Only these parts of the Hamiltonian create a relation between the spin and the spatial coordinates. When the spin-orbit coupling and the dipole interaction (both terms are of similar size in the systems under consideration) are neglected, real space and spin space can be regarded as completely independent. For this purpose generalized groups, the spin space groups (SSG)[96], have been introduced [88, 92]. The action of a SSG operator $\{\alpha_S|\alpha_R|\mathbf{t}\}$ on a two-component spinor can be defined by

$$\{\alpha_S|\alpha_R|\mathbf{t}\}\psi(\mathbf{r}) = \mathbf{U}(\alpha_S)\psi(\{\alpha_R|\mathbf{t}\}^{-1}\mathbf{r}) = \mathbf{U}(\alpha_S)\psi(\alpha_R^{-1}\mathbf{r} - \alpha_R^{-1}\mathbf{t}), \tag{3.27}$$

where ψ is a two-component spinor, α_S and α_R are the spin and space rotation, respectively, $\mathbf{t}$ is a non-symmorphic space translation and $\mathbf{U}$ is the spin 1/2 rotation matrix (with Euler angles α, β, γ),

$$\mathbf{U}(\alpha,\beta,\gamma) = \begin{pmatrix} e^{-i\frac{\alpha+\gamma}{2}}\cos(\frac{\beta}{2}) & -e^{-i\frac{\alpha-\gamma}{2}}\sin(\frac{\beta}{2}) \\ e^{i\frac{\alpha-\gamma}{2}}\sin(\frac{\beta}{2}) & e^{i\frac{\alpha+\gamma}{2}}\cos(\frac{\beta}{2}) \end{pmatrix}. \tag{3.28}$$

Under the restriction $\alpha_S = \alpha_R$ we return to the definition of the operations of the usual space group. The operators of the space group are thus a subset of the SSG operators. The condition $\alpha_S = \alpha_R$ implies that the spin and the space coordinates are transformed in the same way. This property is required for operations that leave the Hamiltonian invariant when SOC is taken into account. The relative angle between the lattice and the spin is important in this case. However, when SOC is neglected α_S and α_R can be different. This is a very important feature of the SSG and it is a prerequisite for the treatment of incommensurate spin-spirals within an ab-initio calculation[96].

3.3.2 Spin Spirals

A magnetic structure with moments that are rotated around specific axis (here: z-axis, eq. 3.29) by a constant angle from atom to atom along a certain direction of the crystal is called a spin-spiral. This can be described by a reciprocal lattice vector, the spin-spiral vector $\mathbf{q}$. The rotation angle of the magnetic moment of an atom at the position $\mathbf{R}_n$ is then given by $\varphi = \mathbf{q} \cdot \mathbf{R}_n$. The magnetic moment of an atom at the position $\mathbf{R}_n$ is given by

$$\mathbf{M}^n = M(\cos(\mathbf{q} \cdot \mathbf{R}_n + \phi) \sin\theta, \sin(\mathbf{q} \cdot \mathbf{R}_n + \phi) \sin\theta, \cos\theta), \tag{3.29}$$

where θ is the so-called *cone angle*, a relative angle between the magnetic moment and the rotation axis, assumed in z-direction, and ϕ an eventual phase factor, also called *phase angle*. Fig. 3.3 shows four examples of spin-spirals with spin-rotation axis perpendicular ((a) and (c)) and parallel ((b) and (d)) to the spin-spiral vector $\mathbf{q}$ and different angles between the spin-rotation axis and the magnetic moment.

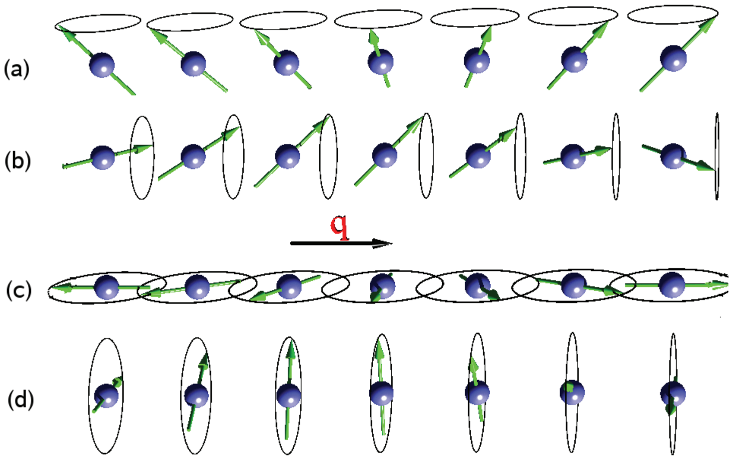

Figure 3.3: Four examples of spin-spirals with spin-rotation axis perpendicular ((a) and (c)) and parallel ((b) and (d)) to the spin-spiral vector $\mathbf{q}$. For each case two spirals with cone angles of $\theta = \pi/2$ and $\theta = \pi/4$ between the magnetic moment and the rotation axes are shown[38].

The spin-spiral vector $\mathbf{Q}$ is a vector in the real space coordinate frame, while the spin-rotation axis is a direction (vector) in the spin-coordinate frame. Since these two coordinate frames become totally independent when spin-orbit coupling is neglected, the angle between the spin-spiral vector $\mathbf{Q}$ and the spin-rotation axis becomes meaningless. In that case the two spirals at the top and the two spirals at the bottom of Fig. 3.3 become completely equivalent. However, the spin spirals with different θ do not become equivalent.

The *cone angle* θ is still a well defined quantity if SOC is neglected, because the rotation axis is a vector (direction) in spin space.

Spin-spirals are frequently called spin density wave, or more specific spiral spin density waves (to distinguish from the longitudinal spin density waves) or frozen magnons. The origin of the last term is that a spin-spiral looks like a “snap shot” of a single magnon at a fixed time. Spin spiral calculations can therefore be used to simulate the effect of temperature on a magnetic system. Another possible application of spin-spirals is the simulation of the long range domain walls including the calculation of the formation energy.

Though there are many possible applications for spin-spiral calculations, it was the discovery of a spiral ground state structure in fcc iron [32] and $4f$ and $5f$ metals [33] that gave rise to many theoretical studies [34, 35]. A very important theorem, which allows the treatment of the spin-spirals in the first-principles calculations without the use of large super-cells, is the generalized Bloch theorem [83, 97]. This theorem, however, can only be proved when SOC is neglected. For this reason the spin-rotation axis can always be considered as parallel to the z-axis of the spin-coordinate frame. Thus, only the m_x and m_y components are rotated, while m_z does not change (eq. 3.29).

3.3.3 Generalized Bloch Theorem

In the case of an incommensurate spin-spiral the periodicity with respect to lattice translations along the direction of $\mathbf{q}$ is lost. This is a major problem for ab-initio methods that rely on the translational periodicity. However, when spin-orbit coupling is neglected, all atoms of the spiral structure are equivalent. The magnitude of the magnetic moment of each atom is the same and they all “see” the same local environment, i.e. the relative angles between the local moment and the moments of the neighbors are equal. Only the angle between the local moment and the lattice changes from site to site, but that is only significant in the presence of SOC. This leads to a generalization of the Bloch Theorem[83, 97].

Let us consider a spin-spiral structure in a crystal without an external magnetic field and take the rotation angle $\varphi = \mathbf{q} \cdot \mathbf{R}_n$ to be counterclockwise. The only term of the Hamiltonian that changes from site to site is the exchange correlation B-field $\mathbf{B}_{xc}$, i.e. the matrix potential $\mathbf{V} = V\mathbf{I}_2 + \mu_B \sigma \cdot \mathbf{B}_{xc}$. Hence, the Hamiltonian satisfies the relation

$$\mathcal{H}(\mathbf{r} + \mathbf{R}_n) = \mathbf{U}(\mathbf{q}\mathbf{R}_n)\mathcal{H}(\mathbf{r})\mathbf{U}^{\dagger}(\mathbf{q}\mathbf{R}_n). \tag{3.30}$$

As pointed out in the previous section the rotation axis can always be taken to be along the spin z-axis. Thus, the spin 1/2 rotation matrix (Eq.3.28) has the form

$$\mathbf{U}(\mathbf{q}\mathbf{R}_n) = \begin{pmatrix} e^{-i\varphi/2} & 0 \\ 0 & e^{i\varphi/2} \end{pmatrix}, \quad \varphi = \mathbf{q} \cdot \mathbf{R}_n. \tag{3.31}$$

Keeping these properties of the Hamiltonian in mind we can define a generalized translation, $\mathcal{T}_n = \{-\mathbf{q}\mathbf{R}_n|\epsilon|\mathbf{R}_n\}$, that combines a lattice translation and a spin rotation. Here ϵ denotes the identity operation. These translations are members of the SSG but not of the usual space group, since the rotation in spin space differs from the rotation in real space. Applying a generalized translation to $\mathcal{H}\psi$ yields

$$\begin{aligned}\mathcal{T}_n\mathcal{H}(\mathbf{r})\psi(\mathbf{r}) &= \mathbf{U}(-\mathbf{q}\mathbf{R}_n)\mathcal{H}(\mathbf{r}+\mathbf{R}_n)\mathbf{U}^\dagger(-\mathbf{q}\mathbf{R}_n)\mathbf{U}(-\mathbf{q}\mathbf{R}_n)\psi(\mathbf{r}+\mathbf{R}_n) \\ &= \mathcal{H}(\mathbf{r})\mathbf{U}(-\mathbf{q}\mathbf{R}_n)\psi(\mathbf{r}+\mathbf{R}_n). \end{aligned} \tag{3.32}$$

Thus, the generalized translation commutes with the Hamiltonian:

$$\mathcal{T}_n\mathcal{H} = \mathcal{H}\mathcal{T}_n \tag{3.33}$$

It can be shown that the generalized translation operations satisfy the relation

$$\mathcal{T}_n\mathcal{T}_m = \mathcal{T}_m\mathcal{T}_n = \mathcal{T}_{n+m} \tag{3.34}$$

In analogy with the proof of Bloch's theorem[84] it follows that the eigenstates can be chosen such that

$$\mathcal{T}_n\psi(\mathbf{k},\mathbf{r}) = \mathbf{U}(-\mathbf{q}\mathbf{R}_n)\psi(\mathbf{k},\mathbf{r}+\mathbf{R}_n) = e^{i\mathbf{k}\cdot\mathbf{R}_n}\psi(\mathbf{k},\mathbf{r}). \tag{3.35}$$

This formulation of the generalized Bloch Theorem is equivalent to the statement that the eigenstates of the Hamiltonian can be written in the form

$$\psi(\mathbf{k},\mathbf{r}) = e^{i\mathbf{k}\cdot\mathbf{r}}\begin{pmatrix} e^{-i\mathbf{q}\cdot\mathbf{r}/2}\alpha(\mathbf{k},\mathbf{r}) \\ e^{+i\mathbf{q}\cdot\mathbf{r}/2}\beta(\mathbf{k},\mathbf{r}) \end{pmatrix}, \tag{3.36}$$

where $\alpha(\mathbf{k},\mathbf{r})$ and $\beta(\mathbf{k},\mathbf{r})$ are functions with translational periodicity, e.g. $\alpha(\mathbf{k},\mathbf{r}) = \alpha(\mathbf{k},\mathbf{r}+\mathbf{R}_n)$. We will prove the equivalence of (3.35) and (3.36) in two steps.

(i) (3.36) ⇒ (3.35)

$$\begin{aligned}\mathcal{T}_n\psi(\mathbf{k},\mathbf{r}) &= e^{i\mathbf{k}\cdot\mathbf{R}_n}\psi(\mathbf{k},\mathbf{r}) \\ &= e^{i\mathbf{k}\cdot(\mathbf{r}+\mathbf{R}_n)}\begin{pmatrix} e^{-i\mathbf{q}\cdot\mathbf{r}/2}\alpha(\mathbf{k},\mathbf{r}+\mathbf{R}_n) \\ e^{+i\mathbf{q}\cdot\mathbf{r}/2}\beta(\mathbf{k},\mathbf{r}+\mathbf{R}_n) \end{pmatrix} \\ &= e^{i(\mathbf{k}\cdot\mathbf{R}_n)}\begin{pmatrix} e^{i(\mathbf{k}-\mathbf{q}/2)\cdot\mathbf{r}}\alpha(\mathbf{k},\mathbf{r}+\mathbf{R}_n) \\ e^{+i(\mathbf{k}+\mathbf{q}/2)\cdot\mathbf{r}}\beta(\mathbf{k},\mathbf{r}+\mathbf{R}_n) \end{pmatrix}\end{aligned} \tag{3.37}$$

(ii) (3.35) ⇒ (3.36)

$$\begin{aligned}\mathcal{T}_n\psi(\mathbf{k},\mathbf{r}) &= e^{i\mathbf{k}\cdot\mathbf{R}_n}\psi(\mathbf{k},\mathbf{r}) \\ &= e^{i\mathbf{k}\cdot(\mathbf{r}+\mathbf{R}_n)}\begin{pmatrix} e^{-i\mathbf{q}\cdot\mathbf{r}/2}\alpha(\mathbf{k},\mathbf{r}) \\ e^{+i\mathbf{q}\cdot\mathbf{r}/2}\beta(\mathbf{k},\mathbf{r}) \end{pmatrix} \\ &= e^{i(\mathbf{k}\cdot\mathbf{R}_n)}\begin{pmatrix} e^{i(\mathbf{k}-\mathbf{q}/2)\cdot\mathbf{r}}\alpha(\mathbf{k},\mathbf{r}) \\ e^{+i(\mathbf{k}+\mathbf{q}/2)\cdot\mathbf{r}}\beta(\mathbf{k},\mathbf{r}) \end{pmatrix}\end{aligned} \tag{3.38}$$

$$\Rightarrow \quad e^{i\mathbf{k}\cdot\mathbf{R}_n}\begin{pmatrix} e^{i(\mathbf{k}-\mathbf{q}/2)\mathbf{r}}\alpha(\mathbf{k},\mathbf{r}+\mathbf{R}_n) \\ e^{i(\mathbf{k}+\mathbf{q}/2)\mathbf{r}}\beta(\mathbf{k},\mathbf{r}+\mathbf{R}_n) \end{pmatrix} = e^{i\mathbf{k}\cdot\mathbf{R}_n}\begin{pmatrix} e^{i(\mathbf{k}-\mathbf{q}/2)\mathbf{r}}\alpha(\mathbf{k},\mathbf{r}) \\ e^{i(\mathbf{k}+\mathbf{q}/2)\mathbf{r}}\beta(\mathbf{k},\mathbf{r}) \end{pmatrix}$$

$$\Rightarrow \quad \alpha(\mathbf{k},\mathbf{r}+\mathbf{R}_n) = \alpha(\mathbf{k},\mathbf{r}), \quad \beta(\mathbf{k},\mathbf{r}+\mathbf{R}_n) = \beta(\mathbf{k},\mathbf{r}). \tag{3.39}$$

The fact that α and β are periodic functions is very important for the implementation of the generalized Bloch theorem into the FLAPW[38] and many other (plane-wave based) methods.

3.3.4 Non-Collinear Magnetism in FLAPW

The first implementation of non-collinear magnetism in the ab-initio calculations [98, 90, 89, 99, 91, 34, 100], allowed only one direction of magnetization per atom, i.e. the direction of the magnetization density $\hat{\mathbf{m}}$ is not allowed to change within one sphere[1], but varies only from sphere to sphere (so-called the atomic sphere approximation for the direction of magnetization). This agrees with the intuitive picture that an atom carries a magnetic moment of a certain size and only the direction of these moments differs between the atoms. Such methods describe only the inter-atomic non-collinearity. However, in general the direction of the magnetization changes continuously from site to site, though, in many cases, the deviations from the main atomic direction are only significant in a region between the atom, where the magnitude of the magnetization is rather small. The first calculation that treated the magnetization as a continuous vector quantity was published by Nordström et al. [101]. They followed the most general approach allowing the magnetization to change magnitude and direction continuously, i.e. even within an atom. Thus, their implementation, that is based on the FLAPW method, allows them to also investigate the intra-atomic non-collinearity, which is important for actinides like Pu.

Our method uses a "hybrid" approach (Fig.3.4) where the magnetization is treated as a continuous vector field in the interstitial and in the vacuum regions, while inside each muffin-tin sphere we only allow for one direction of magnetization.

Inside the muffin-tins, like in the collinear case, it is still possible to work with $V_\uparrow$ and $V_\downarrow$ in the non-collinear case, since we restrict the magnetization to the local quantization quantization axis. Therefore, a local spin-space coordinate-frame is introduced with the z-axis parallel to the local quantization axis. $V_\uparrow$ and $V_\downarrow$ are now spin-up and -down with respect to the local axis. Since both, the potential and the basis functions, are set up in terms of the local spin-coordinate frame, the determination of the basis functions and calculation of the integrals of these functions with the Hamiltonian inside the muffin-tins is completely unchanged. The changes come in, when the basis functions inside the muffin-tins are matched to the plane waves in the interstitial region, because the local spin-coordinate frame S^α is rotated with respect to the global frame S^g.

The FLAPW method uses augmented plane waves as basis functions. Therefore, each basis function for a given k-vector, $\vec{k}$, can be uniquely identified by is wave vector $\mathbf{G}$ and the spin direction. The basis functions in the interstitial region are:

---

[1] Within the muffin-tin spheres, however, magnetization can vary in magnitude

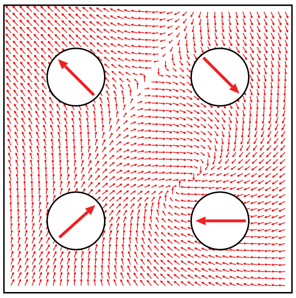

Figure 3.4: Schematic illustration of the representation of the non-collinear magnetization density within the present approach. The magnetization is treated as a continuous vector field in the interstitial region and in the vacuum. Within each muffin-tin the magnetization has a fixed direction and can only vary in magnitude[38].

$$e^{i(\mathbf{k}+\mathbf{G})\mathbf{r}}\chi_\sigma^g \tag{3.40}$$

χ_σ^g is a two component spinor. The index g has been added to notify that χ_σ^g is the representation of this spinor in the global spin frame. This representation of the basis functions is used for both collinear and non-collinear calculations. However, the potential matrix $\underline{V}$, and thus the Hamiltonian, is diagonal in the two spin directions in the collinear case. Therefore, the Hamiltonian can be set up and solved separately for the two spin directions. In the non-collinear case the off-diagonal part of $\underline{V}$ is not zero anymore. Hence, the full Hamiltonian for both spin directions has to be set up and solved in a single step. In the vacuum we also use the global spin frame for the representation of the basis functions. The basis set is only changed in the muffin-tins, because we use a local spin coordinate frame, which is rotated with respect to the global frame. The consequence is that, when the plane waves are matched to the functions in the muffin tin spheres, each spin direction in the interstitial region has to be matched to both, the spin-up and -down basis functions, in the sphere. Thus, the basis set has the following form.

$$\varphi_{\mathbf{G},\sigma}(\mathbf{k},\mathbf{r}) = \begin{cases} e^{i(\mathbf{G}+\mathbf{k})\mathbf{r}}\ \chi_\sigma^g & \text{Int.} \\ \left(A_\sigma^{\mathbf{G}}(\mathbf{k}_\parallel)u_\sigma^{\mathbf{G}_\parallel}(\mathbf{k}_\parallel,z) + B_\sigma^{\mathbf{G}}(\mathbf{k}_\parallel)\dot{u}_\sigma^{\mathbf{G}_\parallel}(\mathbf{k}_\parallel,z)\right) e^{i(\mathbf{G}_\parallel+\mathbf{k}_\parallel)\mathbf{r}_\parallel}\ \chi_\sigma^g & \text{Vac.} \\ \sum\limits_{\sigma^\alpha}\sum\limits_{L}\left(A_{L\sigma\sigma^\alpha}^{\mu\mathbf{G}}(\mathbf{k})u_l^{\sigma^\alpha}(r) + B_{L\sigma\sigma^\alpha}^{\mu\mathbf{G}}(\mathbf{k})\dot{u}_l^{\sigma^\alpha}(r)\right) Y_L(\hat{\mathbf{r}})\ \chi_{\sigma^\alpha} & \text{MT}\mu \end{cases} \tag{3.41}$$

where, $u_l^{\sigma^\alpha}(r)$ is the solution of the radial Schrödinger equation in the “local“ spin-frame σ^α. The sum in the muffin-tins is over the local spin directions and L abbreviates lm. The

A- and B-coefficients depend on the local and the global spin and are obtained from the boundary conditions

$$e^{i(\mathbf{k}+\mathbf{G})\mathbf{r}}\chi_\sigma = \sum_{\sigma^\alpha}\sum_{L}\Big(A^{\mu\mathbf{G}}_{L\sigma\sigma^\alpha}(\mathbf{k})u^{\alpha}_{l\sigma^\alpha}(r) + B^{\mu\mathbf{G}}_{L\sigma\sigma^\alpha}(\mathbf{k})\dot{u}^{\alpha}_{l\sigma^\alpha}(r)\Big)\,Y_L(\hat{\mathbf{r}})\chi^{\alpha g}_{\sigma^\alpha}. \tag{3.42}$$

The local can be transformed to the global spin-coordinate frame S^g by a rotation $\mathbf{R}^\alpha gl$, given by the Euler angles (α, β). In this case, the Euler angles are equivalent to the polar angles of the local quantization axis in the global frame, $\alpha = \varphi,\ \beta = \theta$. The magnetization density and the magnetic field, seen from the global frame, $\mathbf{m}^{\alpha g}(\mathbf{r})$ and $\mathbf{B}^{\alpha g}(\mathbf{r})$, are related to the same quantities seen from the local frame by

$$\begin{aligned}\mathbf{m}^{\alpha g}(\mathbf{r}) &= \mathbf{R}^{\alpha gl}\ \mathbf{m}^{\alpha l}(\mathbf{r})\\ \mathbf{B}^{\alpha g}(\mathbf{r}) &= \mathbf{R}^{\alpha gl}\ \mathbf{B}^{\alpha l}(\mathbf{r}).\end{aligned} \tag{3.43}$$

where the index α indicates, that this corresponds to quantities inside the muffin-tin of atom type α. The Pauli spinors transform according to

$$\chi^{\alpha g} = \mathbf{U}^{\alpha gl}\ \chi^{\alpha l}, \tag{3.44}$$

where

$$\chi^{\alpha l}_{\uparrow} = \begin{pmatrix}1\\0\end{pmatrix}, \quad \chi^{\alpha l}_{\downarrow} = \begin{pmatrix}0\\1\end{pmatrix} \tag{3.45}$$

is their representation in the local spin frame. The matrices $\mathbf{R}^{\alpha gl}$ and $\mathbf{U}^{\alpha gl}$ are given with

$$\mathbf{R}^{\alpha gl} = \begin{pmatrix} \cos\varphi\cos\theta & -\sin\varphi & \cos\varphi\sin\theta \\ \sin\varphi\cos\theta & \cos\varphi & \sin\varphi\sin\theta \\ -\sin\theta & 0 & \cos\theta \end{pmatrix}, \tag{3.46}$$

$$\mathbf{U}^{\alpha gl} = \begin{pmatrix} e^{-i\frac{\varphi}{2}}\cos(\frac{\theta}{2}) & -e^{-i\frac{\varphi}{2}}\sin(\frac{\theta}{2}) \\ e^{i\frac{\varphi}{2}}\sin(\frac{\theta}{2}) & e^{i\frac{\varphi}{2}}\cos(\frac{\theta}{2}) \end{pmatrix}. \tag{3.47}$$

3.4 Magnetic Anisotropy

In an isotropic material, all physical properties are identical for different special directions. When the physical property depends on the crystallographic directions, like velocity of sound or elastic properties, then the material is no more isotropic. Magnetic crystals can be magnetized with minimum energy in a certain direction, called easy axis. On the other hand, it is hard to magnetize the crystal in another certain direction where maximum energy is needed, called the hard axis. The energy needed to change the magnetization direction from the hard to the easy axis is called the magnetic anisotropy energy (MAE).

In general, the MAE will be a complex function of the orientation of the magnetization relative to the crystal axes. In low-dimensional systems twofold symmetries are the most relevant ones and the magnetic anisotropy is then expressed as

$$H_{MAE} = \sum_i \vec{S}_i \cdot \vec{\vec{K}}_i \cdot \vec{S}_i \tag{3.48}$$

where the tensor of single-site anisotropy constants, $\vec{\vec{K}}_i$, determines the strength of the anisotropy as well as the direction of the easy and hard axes. In perfect thin films and wires the presence of a surface holds then responsible for an uni-axial anisotropy energy normal to the surface, i.e. all components of $\vec{\vec{K}}_i$ are zero except $K_i^{zz} = K\delta^{zz}$ for isotropic films and $K_i^{xx} = 1/2K\delta^{xx}\text{and}K_i^{yy} = 1/2K\delta^{yy}$ for isolated wires.

After expressing $\vec{S}_i$ in the form of equation (3.48), the uni-axial MAE takes the angular dependence

$$E_{MAE}(\theta) = -Kcos^2\theta \tag{3.49}$$

θ is the angle between the magnetization and the film or wire normal, and $K = E_{MAE} = E_{MAE}^{(\parallel)} - E_{MAE}^{(\perp)}$ is the uni-axial anisotropy constant given in energy per atom. The magnetization direction is $\perp$ ($\parallel$) to the film plane or wire axis when $K > 0 (K < 0)$. The total MAE of the system, $E_{MAE}^{(tot)} = N_A E_{MAE}$, depends on the number of atoms N_A. For higher symmetries, like surfaces or bulk systems, corresponds to anisotropy contributions which are smaller in energy than the uni-axial anisotropy and are usually neglected. The anisotropy constant depends sensitively on the chemical elements involved, structural details, details of the electronic structure and the dimensionality of the system.

The magnetic dipolar interaction and the spin-orbit interaction are considered to be the microscopic origins of the magnetic anisotropy. The dipolar interaction is of long range and senses the outer boundaries of the sample. This results in the shape anisotropy. Discussing long range contributions, the underlying atomistic lattice describing the crystalline of the system can be neglected and the shape anisotropy is described in terms of a continuum theory. Any contribution to the MAE beyond the continuum theory, taking explicitly the crystallinity of the system into account, is summarized as magnetocrystalline anisotropy energy (MCA). Both the dipolar and the spin orbit interaction contribute to the MCA and the total anisotropy constant K

$$K = K_{shape} + K_{MCA}^{dip} + K_{MCA}^{soc} \tag{3.50}$$

is just a linear superposition of the different contributions. The shape anisotropy constant, K_{shape} in atomic Rydberg units per atom of a perfectly flat ferromagnetic (FM) film of infinite extension, or an infinitely long perfectly cylindrical wire, is given by the local magnetic moment m and the atomic volume V as

$$K_{shape}^{film} = -2\pi\frac{\alpha m^2}{cV} \quad \text{and} \quad K_{shape}^{wire} = -\pi\frac{\alpha m^2}{cV} \tag{3.51}$$

where α is the fine structure constant, $e^2/\hbar c/$, and c is the speed of light. The negative sign means that the shape anisotropy is pulling the magnetization into the film plane or along the wire axis. The shape anisotropy is the most important for bulk samples, thick films, patterned nanostructures and wires. For thin films of few atomic layers and wires and magnetic structures that are not FM, the assumption that the magnetization can be treated by continuous magnetic medium is no longer valid. Then the magnetic dipole-dipole energy has to be evaluated. In transition-metals, the magnetization distribution around the atom is almost spherical and is thus treated to a good approximation as a collection of discrete magnetic dipoles, which are regularly arranged on a crystalline lattice. The dipolar energy E_{dip} per atom experienced by a dipole at site i due to the presence of ferromagnetically aligned dipoles on all other sites j can then be expressed as

$$K_{dip}^{(i)}(\theta) = K_{dip}^{(i)} cos^2(\theta) = \frac{2}{c^2} \sum_{j(j \neq i)} \frac{m_i m_j}{\mathbf{R}_{i,j}^3} (1 - 3cos^2\theta_{ij}) \tag{3.52}$$

θ_{ij} is the angle between the direction of the magnetic moment m of the dipoles at sites i or j given in units of Bohr magneton and the vector $\mathbf{R}_{i,j}$ connecting atoms i and j, it denotes the relative distance between these dipoles or atoms, respectively. The θ-dependence expresses the fact that the dipole-dipole interaction contributes to the magnetic anisotropy. In thin films and wires the anisotropy energy depends on the position of the atom i normal to the surface or wire axis, and on the film thickness or wire diameter (in difference to K_{shape} where all atoms have the same value). For crystalline thin wires and films the sum in equation (3.52) can be evaluated straight forwardly with fast converging summation techniques [102, 103]. Draaisma and de Jonge[93] worked out in detail the layer dependent dipolar anisotropy $K_{dip}^{(i)}$. In general, the outer atoms experience values of K_{dip} that are smaller than those of the inner layers which finally approach K_{shape}. The inner atoms reach 95% of K_{shape} after about 15 Åbelow the surface. The exact details depend on the crystal structure and surface orientation, e.g. a reduction between 25% and 45% of K_{shape} was reported for a (001) oriented fcc or bcc monolayer. The deviation of K_{dip} from K_{shape} gives the dipolar contribution to the MCA K_{MCA}^{dip} in equation (3.50), which occurs here due to the presence of a surface or interface and is sometimes also called the surface contribution of the dipolar anisotropy. If the MAE is expressed in terms of energy densities ϵ, $E_{MAE} = V\epsilon$. This K_{MCA}^{dip} is expressed in terms of an areal density. The dipolar energy contributes also to the MCA of bulk systems or thick films or wires, if the underlying lattice structure has a twofold symmetry. For this three-dimensional case more sophisticated summation techniques such as the Ewald summation method[104] is required to obtain reliable results for equation (3.52).

The spin-orbit interaction, treated typically by a Pauli-type addition to the Hamiltonian as:

$$H_{soc} = \frac{\mu_B}{2mc} \sigma \cdot (\mathbf{E}(\mathbf{r}) \times \mathbf{p}) = \frac{\mu_B}{2mc} \sigma \cdot (\bigtriangledown V(\mathbf{r}) \times \mathbf{p}) \tag{3.53}$$

provides the essential contribution to the MCA. This Pauli approximation is derived from the Dirac equation, and is normally sufficient for treating relativistic effects in transition-metal magnets. For a radially symmetric potential, equation (3.53) can be rewritten as:

$$H_{soc} = \frac{\mu_B}{2mc}\frac{1}{r}\frac{dV(\mathbf{r})}{dr}\sigma \cdot (\mathbf{r} \times \mathbf{p}) = \frac{\mu_B}{2mc}\frac{1}{r}\frac{dV(\mathbf{r})}{dr}(\sigma \cdot \mathbf{L}) = \frac{\mu_B}{2mc}\xi(\mathbf{r})\sigma \cdot \mathbf{L} \tag{3.54}$$

where $\vec{L}$ is the angular momentum operator. Since the radial derivative of the potential in a crystal will be largest in the vicinity of a nucleus, then the major contribution to the spin-orbit interaction will come from this region. For small r the potential will be Coulomb-like ($V = -\frac{Z}{r}$), therefore the radial expectation value of $\xi(\vec{r})$ leads to a material dependent spin-orbit coupling constant ξ, which is proportional to Z^2. The MCA dominates in low dimensions over the shape anisotropy and the anisotropy depends crucially on the symmetry of the system. In a solid, the symmetry is determined by the crystal field, then the spin-orbit coupling will introduce orbital moments and magnetocrystalline anisotropy by coupling the states which do not carry orbital moments such that the combination form an orbital moment, eg. a $d_{xy} + d_{x^2-y^2} \rightarrow m = \pm z$.

In second-order perturbation theory, the expectation value of the orbital moment operator $\mu_B\mathbf{L}$ can be written as:

$$m_l = \mu_B \left\langle \vec{L} \right\rangle = \mu_B \sum_{i,j} \frac{\langle\psi_i|\mathbf{L}|\psi_j\rangle \langle\psi_j|H_{soc}|\psi_i\rangle}{\epsilon_i - \epsilon_j} f(\epsilon_i)[1 - f(\epsilon_j)] \tag{3.55}$$

where f is the Fermi function insuring that the wavefunction ψ_i is occupied and ψ_j is unoccupied. In metals, several bands crossing the Fermi level E_F. The sum of all contributions from bands near E_F determine the orbital moment. Van der Laan[105] showed that when the majority and minority bands are well separated by the exchange interaction, the spin-orbit coupling changes the total energy of the system in second-order perturbation theory as:

$$\delta E = \sum_{i,j} \frac{\langle\psi_i|H_{soc}|\psi_j\rangle \langle\psi_j|H_{soc}|\psi_i\rangle}{\epsilon_i - \epsilon_j} f(\epsilon_i)[1 - f(\epsilon_j)] \approx -\frac{\xi}{4\pi\mu_B}\widehat{m}_s \cdot [\mathbf{m}_l^{\downarrow} - \mathbf{m}_l^{\uparrow}] \tag{3.56}$$

where $\widehat{m}_s$ is the direction of the spin moment, and $m_l^{\downarrow}$ ($m_l^{\downarrow}$) is the orbital moment vector for spin-down (up) bands. If the spin-up band is completely filled, then the energy change δE is proportional to the size of the orbital moment and the magnetocrystalline anisotropy energy. This means that the difference of δE for two different magnetization directions will be proportional to the difference in the orbital moments. This relation between orbital moment anisotropy and MCA was first derived by Bruno[55].

The spin moment increases in low-dimensional systems because of reduced coordination number (see subsec. 3.1.1). This increase will enable the formation of large orbital moments, as can be seen from most atoms. In figure 3.5 some representative values of

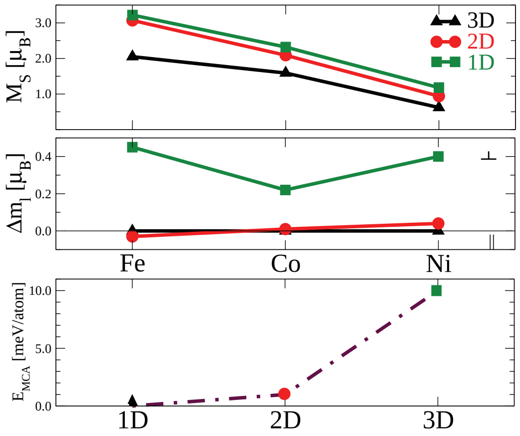

Figure 3.5: Local spin m_s and difference between ($\perp$) and ($\|$)orbital magnetic moments Δm_l in units of μ_B of Fe, Co and Ni atoms in bulk materials (3D), unsupported thin films (2D) and wires (1D). For the bulk crystals the variation of the orbital moment with the direction is small, but for films and wires the differences in orbital moments parallel ($\|$) and perpendicular ($\perp$) to film-plane or wire-axis are given.Positive Δm_l means the perpendicular ($\perp$) are larger than the ($\|$) orbital moments. The $|E_{MCA}|$ indicates the order of magnitude of the magnetocrystalline anisotropy energy for different dimensions. The results were obtained in the generalized gradient approximation to the density functional theory[86].

spin and orbital momentum have been collected. These calculations yield very small orbital moments: 0.05 μ_B, 0.08 μ_B and 0.05 μ_B for bcc Fe, hcp Co, and fcc Ni, and about twice the value if the orbital polarization (OP) proposed by Brooks[106] is included. It is known that the orbital moments are quenched in the bulk due to the strong hybridization with neighboring atoms. Larger orbital moments are obtained for the (111) oriented unsupported 3d monolayers. For Fe, Co and Ni the values are 2-3 times larger than the corresponding bulk values. Thus, in monolayer films the quenching of the orbital moments is less pronounced due to the reduced hybridization.

However, it is important to realize that these enhanced orbital moments are still an order of magnitude smaller than the corresponding free atom values, as given by Hund's second rule. Consequently, for atomic scale, magnetic structures such as wires, small clusters and adatoms strong changes in the orbital moment occurs which leads to large values of the magnetocrystalline anisotropy energy. In practice, these films are deposited on substrates, which will once quench the values, especially for the orbital moments. But the spin-polarization of the substrate can lead to additional large contributions to the magnetocrystalline anisotropy energy in particular for substrates with large Z, such as Pt or Ir.

First principles calculations based on the LSDA or GGA underestimate the orbital

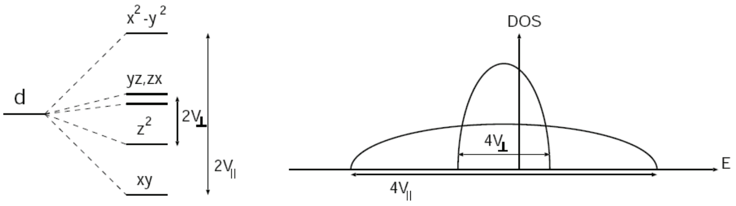

Figure 3.6: *d*-level splittings shown in the left figure at a given **k**-point due to a crystal field in a square monolayer results in a density of states, shown on the right[86].

moments. In the literature several methods have been discussed how this deficiency can be overcome[106, 94, 107]. For example, the orbital moments of the bulk magnets are about twice the value if Brooks' orbital polarization is applied[95, 108]. The effect of OP is much more drastic in low dimensions[109].

Stör introduced a simple model to to interpret ab initio results on thin films using unsupported (001) oriented d-metal monolayer[110]. Assume that the d-band is substantially exchange split and more than half filled, so that only the (partially filled) minority band has to be considered. The d-orbitals at each atom site experience in the a crystal field V in the monolayer plane. This leads to a splitting of these levels. If the surface normal is assumed to be in z-direction, the d_{xy} and $d_{x^2-y^2}$ levels will experience a stronger field than the out-of-plane directed d_{zx}, d_{yz} and d_{z^2} orbitals. The crystal field leads to a splitting of $2V_\parallel$ for the in-plane oriented orbitals and $2V_\perp$ for the out-of-plane oriented ones. In band-picture, these splittings can be translated into band widths W, which will then be twice as large (cf. Figure 3.6). Normally, $V_\parallel$ will be larger than $V_\perp$, so that $R = V_\perp / V_\parallel < 1$. However, if the monolayer is sandwiched between two slabs of nonmagnetic material the situation could be changed. If the minority band is half filled -like in the case of Co-; the d_{xy} and $d_{x^2-y^2}$ states will split symmetrically by $\pm V_\parallel$ around the Fermi level, the (d_{zx}, d_{yz}) and d_{z^2} states by $\pm V_\perp$. In a band-picture, these splittings will of course depend on the considered $\vec{K}_\parallel$ point. Now we can use perturbation theory equation (3.55) to calculate the orbital moments

$$m_l^\parallel = \frac{\xi \mu_B}{2V_\parallel}\left(\frac{3}{R} + \frac{2}{R+1}\right) \qquad \text{and} \qquad m_l^\perp = 4\frac{\xi \mu_B}{2V_\perp} \tag{3.57}$$

from this equation, only the in-plane orbital moments, $m_l^\parallel$, depends on the splitting of the out-of-plane oriented states, where the out-of-plane moment, $m_l^\perp$, is only quenched by the in-plane crystal field $V_\parallel$. This is clear since $m_l^\perp$ corresponds to an in-plane motion of the electron, i.e. hopping between the d_{xy} and $d_{x^2-y^2}$ states that are separated by $V_\parallel$. Using equation 3.56, the magnetocrystalline anisotropy energy becomes:

$$K_{MCA} = E_{MCA}^\parallel - E_{MCA}^\perp = \frac{\xi}{4\mu_B}(m_l^\parallel - m_l^\perp) = -\frac{\xi^2}{8V_\parallel}\left(\frac{3}{R} + \frac{2}{R+1} - 4\right) \tag{3.58}$$

This means that as long as $R < 1$ an in-plane magnetization is obtained, while for $R > 1$ an out-of-plane magnetization easy axis is possible.

3.4.1 Magnetic anisotropy and critical temperature:

In ferromagnetic two dimensional systems, we can use the magnetic anisotropy energy ($\mathrm{E}_{\mathrm{MAE}}$) to estimate the two dimensional Néel critical temperature, $T_c^{(2\mathrm{D})}$ from . The simplest statistical-mechanics method to estimate the magnetic transition temperature is the mean-field approximation[111, 112, 113, 114]. This method is, however, unsatisfactory in the case of 2D magnets since it neglects the long-wavelength fluctuations and, therefore, gives a nonzero value of the magnetic transition temperature for isotropic Heisenberg Hamiltonian contradicting to the Mermin-Wagner theorem[115]. Much better suited for the study of the 2D systems is the random phase approximation (RPA)[116, 114]. According to a renormalization group analysis[117], the two dimensional $T_c^{(2\mathrm{D})}$ scales with the three dimensional critical temperature $T_c^{(3\mathrm{D})}$ obtained from the 3D-Heisenberg model, which is normalized by logarithmic factor:

$$T_c^{(2\mathrm{D})} = \frac{2T_c^{(3\mathrm{D})}}{\ln\left(\frac{\pi^2 \mathrm{J}_1}{\mathrm{E}^{\perp}_{\mathrm{MAE}}}\right)} \tag{3.59}$$

This equation contains the strength of the uniaxial anisotropy energy $E^{\perp}_{MAE}$. J_1 is the next nearest neighbor exchange interaction parameter in Heisenberg picture.

Chapter 4

Collinear magnetism of $3d$-monolayers on Rh substrates

4.1 $3d$-Monolayers on (001) oriented substrates

During the past two decades, theoretical and experimental investigations were performed to understand the magnetism of ultrathin magnetic films on (001) oriented nonmagnetic substrates. Mainly the weakly interacting coinage metals (Cu, Ag, Au) and some transition metals (TMs), e.g. Pd, have been chosen as substrate in order to minimize the interaction between monolayer and substrate[1, 2]. Cu with an experimental lattice constant of $a_o = 3.61$ Å turned out to be an ideal template for fcc bulk TMs, while Ag ($a_o = 4.09$ Å) and Au ($a_o = 4.08$ Å) are templates to grow the bcc metals. Employing density functional theory (DFT), some general trends were identified for $3d$ monolayers (ML) on these substrates: (i) The magnetic moments of the monolayers are considerably enhanced as compared to the equivalent bulk systems and (ii) similar to the bulk cases, Fe, Co, and Ni are ferromagnetic (FM) on these substrates, while V, Cr, and Mn prefer a $c(2 \times 2)$ antiferromagnetic (AFM) structure, i.e., a checkerboard arrangement of antiparallel magnetic moments[3, 5], a magnetic structure which cannot be derived from respective bulk phases. Experimentally, Ortega and Himpsel studied $3d$ monolayers on Ag(001) and confirmed the theoretical predictions, especially the magnetism of V on Ag(001)[6].

4.1.1 $3d$ monolayers on Pd, Ag and W (001) substrates:

Here we discuss specific theoretical results obtained of $3d$ monolayer on Pd(001)[3], Ag(001)[4] and W(001)[7] substrates. We will use these results to compare them to our calculational results of for $3d$ monolayers on Rh(001) substrates in next section.

In the $3d$ series the overall trend of the local moments follows Hund's first rule as shown in figure 4.1. The largest local moment of about 4 μ_B was found for Mn and from Mn to Ni the magnetic moment decreases in steps of 1 μ_B. The latter behavior is a consequence of the strong ferromagnetism in these monolayers, because they have one spin band is fully occupied so that the density of states at Fermi level (see sec. 3.1) is small or even zero, then susceptibility of such systems is thus also small or zero because the spin splitting is saturated so that an additional field cannot cause an significant additional magnetic moment[118]. The magnetic moments of Ti, V, and Cr monolayers show a pronounced dependence on the substrate: Ti is magnetic on Ag, but nonmagnetic on Pd; the magnetic moment of V is reduced by more than 1.5 μ_B when changing the substrate from Ag to Pd; and for Cr the magnetic moment changes, in the FM (AFM) configuration, from 3.78 (3.47) μ_B on Ag to 3.87 (3.46) μ_B on Pd.

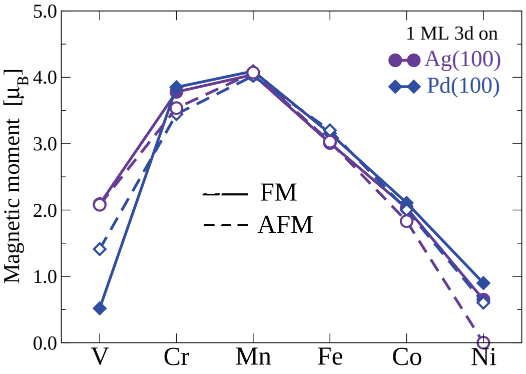

Figure 4.1: Local magnetic moments of $3d$ monolayers on Ag(001) and Pd(001) calculated for the p(1×1) ferro- (solid symbols connected by solid line) and the c(2×2) antiferromagnetic configuration (open symbols connected by dashed line)[3, 5].

Later on, it was experimentally found that Fe has a c(2×2)-AFM ground state on W(001)[11], which was theoretically predicted[8, 9, 10]. A theoretical study to predict the magnetic ground state of $3d$-transition metals on W(001) substrate followed this finding[7]. The magnetic ground state was predicted to be ferromagnetic for V, Cr and Mn while Fe, Co and Ni prefer the c(2×2)-AFM order on W(001) substrate. This trend is opposite trend from what Blügel found in the case of Ag or Pd substrate as shown in figure 4.2. The $3d$ monolayers on W(110)[119] show the same behavior as on noble metal substrates, this clearly gives evidence that results on W(001) are an effect of hybridization with the open (001) surface.

The reason of this opposite trend can be explained as following: In case of strong overlayer-substrate hybridization, the coordination number, symmetry and interlayer distance is decisive in the determination of the magnetic properties of the system. On the other hand there is a difference between a bcc (001) substrate such as W and fcc (001) substrate as Ag. For a bcc substrate each $3d$-transition metal atom has only four nearest W atoms at the interface, while the surrounding atoms in the overlayer are next nearest neighbors. In the fcc substrate each $3d$-transition metal atom has eight nearest neighbors, four $3d$

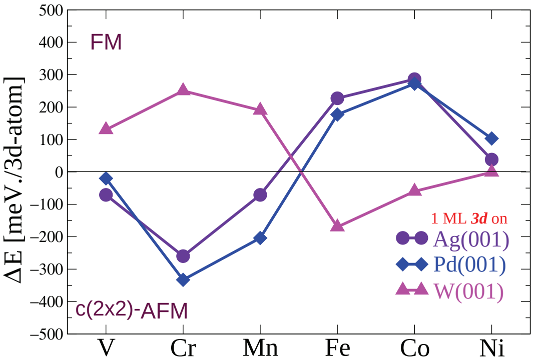

Figure 4.2: Total energy difference $\Delta E = E_{AFM} - E_{FM}$ per $3d$ atom between the c(2×2)-AFM and p(1×1)-FM phase for $3d$ monolayers on Ag(001)(circles), Pd(001) (diamonds) and W(001)(triangles). $\Delta E > 0$ (< 0) means that the ferromagnetic (antiferromagnetic) configuration is the most stable one[3, 5, 7].

atoms within the monolayer and four substrate interface atoms. Considering that the $5d$ orbitals of W are more extended than the $3d$ ones of the overlayer and taking the additional interlayer relaxation into account, we can conclude that here the hybridization between the overlayer and the substrate is more important than the hybridization between the $3d$ atoms in the monolayer plane. Thus, the nature of the $3d$-$4d$ or -$5d$ bond determines the physics.

The strong $3d$-$5d$ hybridization effects also the magnetic moments, displayed in figure 4.3. Similar to fcc substrates the overall trend of the spin moments across the $3d$ series follows Hund's first rule. This atomic-like behavior indicates that the magnetism is dominated by the local intra-atomic contribution. A comparison with unsupported monolayers (UML) using the experimental W lattice constant shows that the magnetic moment of the $3d$ overlayer is reduced due to the interaction with the substrate, which is a consequence of the $3d$-$5d$ hybridization.

The magnetism of the overlayer also polarizes the substrate. For the FM configuration, the W atoms at the interface are antiferromagnetically coupled to the monolayer (apart from the case of Co) and carry a moment which is roughly proportional to that of the $3d$ TM. The induced polarization decreases rapidly with distance from the interface into the bulk and is already one order of magnitude lower at the second W layer. The sign of the magnetization oscillates from one W layer to the next, indicating a layered AFM (LAFM) susceptibility of W(001). For antiferromagnetic monolayers, the W moments in every second layer are suppressed due to symmetry.

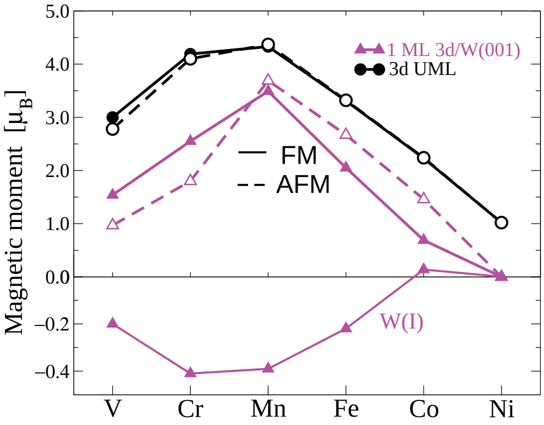

Figure 4.3: Local magnetic moments of 3*d* monolayers on W(001) calculated for the p(1×1) ferro- (solid symbols connected by solid line) and the c(2×2) antiferromagnetic configuration (open symbols connected by dashed line). For the FM case, the magnetic moment of interface W atoms is given by triangles[7].

4.2 Results of 3*d*-Monolayers on Rh(001) Substrate

In this section we will show results of ab initio calculations of 3*d* monolayers on the 4*d* TM substrate Rh(001). Rh has a large Stoner enhanced susceptibility as shown for Rh films on Fe [15] and FeRh is known to form ordered alloys in the cesium chloride (CsCl-type) structure with subtle magnetic properties[16, 17, 18]. The lattice constant of Rh (a_o = 3.80 Å) is in between those of Cu and Ag and thus Rh serves as a potential substrate to grow artificial phases of 3*d* transition-metal films such as fcc-Fe stabilized under tensile strain or bcc-Co under compressive strain. The Rh(001) substrate provides favorable growth conditions for transition-metal films despite a large lattice mismatch of fcc Fe or Co and bcc Fe with Rh of about 6%, 8% and -7%, respectively. For example, no notable intermixing has been encountered at the interface of Fe/Rh(001) during growth of Fe films[19]. Epitaxial, pseudomorphic layer-by-layer growth of one and two layers of Co on Rh(001) was reported by Begley *et al.* [20] and several groups [19, 21, 22, 23] have been able to grow pseudomorphically even thicker films of face-centered tetragonal Fe on Rh(001). Hayashi *et al.*[22, 23] concluded on the basis of soft X-ray magnetic circular dichroism (XMCD) experiments measured at room temperature that a monolayer and a bilayer of Fe are not ferromagnetic and interpreted them as magnetically dead caused by the large strain exceeded in the interface of the thin film and the substrate. Hwang *et al.*[24] found experimentally a suppression of the ferromagnetic order of Fe overlayers on the Rh(001) surface, and he as well as Spisak and Hanfer[25] predicted a $c(2 \times 2)$ AFM order for 1 ML Fe on Rh(001) on the basis of DFT calculations.

In our study, we determined the structural, electronic and magnetic properties of *3d* TM monolayers on Rh(001) by performing the first principles calculations using the full potential linearized augmented plane wave (FLAPW) method in film geometry as implemented in the (`FLEUR`) code (see chapter 2). The generalized-gradient approximation of Perdew, Burke and Ernzerhof was applied (see section 1.5) leading to a Rh bulk lattice constant of 3.819 Å which is only 0.4% larger than the experimental lattice constant of 3.804 Å[120]. The film was modeled by a symmetric seven layer Rh(001) slab covered by a single *3d* monolayer (see figure 2.2), using the calculated in-plane Rh lattice constant. Relaxations were considered for the topmost two layers, i.e., the *3d* ML and the interface ML Rh(I). Both, the FM and the $c(2 \times 2)$ AFM configuration were relaxed. We used about 120 LAPW basis functions per atom with a muffin-tin radius of 1.22 Å for the *3d* monolayer atoms and 1.28 Å for the Rh atoms. The irreducible part of the two-dimensional Brillouin zone (I2DBZ) was sampled with 78 $\mathbf{k}_{\|}$ points for the FM (AFM) configuration.

4.2.1 Relaxations and magnetic moments:

Here we present relaxations results of 1 ML $3d$/Rh(001). The formula we used to calculate the relaxation, Δd_{xy}, between the layer i and j is:

$$\Delta d_{ij} = \frac{d_{ij} - d_o}{d_o} \tag{4.1}$$

where, d_{ij} is the interlayer distance and d_o is the ideal bulk interlayer distance of the substrate. First we relaxed the top most monolayers of the clean Rh(001) surface. The nonmagnetic relaxations of the interlayer spacing between the topmost monolayer and the second layer, Δd_{12}, and the second Rh interlayer spacing, Δd_{23}, were -0.3% and $+0.2\%$ respectively. Our prediction of top most two monolayers' Rh(001) relaxations are in a very good agreement compared to the experimental relaxations:$\Delta d_{12} = +0.5 \pm 1.0$ $(-1.6 \pm 1.6)\%$ and $\Delta d_{23} = 0 \pm 1.5\%$ $(0 \pm 1.6)\%$[121]([122]).

The relaxations of the interlayer spacing between the *3d* monolayer and the topmost substrate layer, Δd_{12}, and the first Rh interlayer spacing, Δd_{23}, are presented in Figure 4.4 for both FM and AFM configurations.

For the FM configuration, we notice that the smallest inward relaxation of the *3d* monolayer occurs for Mn and Fe on Rh(001), where the magneto-volume effect (the atomic volume dependence of the magnetic susceptibility) is strongest, i.e. the large magnetic moments (see Fig. 4.5) of these TM compensate the strong inward relaxation – caused by the larger Rh lattice constant – most efficiently. Of course there are also other factors controlling the Δd_{12} that is, e.g., for V smaller than for Cr although the magnetic moment of the latter is much larger that of vanadium. Here, also the fact that the bulk lattice constant of V is 5% larger than that of Cr has to be considered. With the exception of Ni, in all cases the equilibrium distance between the interface Rh layer and the bulk Rh underneath increases with respect to the substrates bulk interlayer spacing. Moving from left to right through the periodic table, we find that Δd_{23} decreases, supporting the interpretation that the *d*-band filling controls these relaxations[123, 124]. This highlights

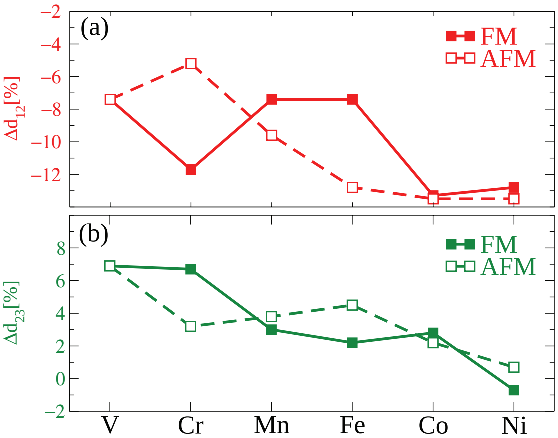

Figure 4.4: Relaxations of the first and second interlayer spacing, Δd_{12} (circles) and Δd_{23} (squares), respectively, for *3d* TM monolayers on Rh(001) for the FM (solid symbols connected by solid lines) and the $c(2 \times 2)$ AFM (open symbols connected by dashed line) configuration. The corresponding changes are given with respect to the substrates bulk interlayer spacing, which is 1.91 Å.

the importance of multilayer relaxations for the early transition monolayers. The same trend can be seen for the monolayers with $c(2 \times 2)$ AFM configuration: while Δd_{12} is also influenced by the magnetic moment of the *3d* monolayer, Δd_{23} depends almost solely on the *d*-band filling.

In Fig. 4.5 the magnetic moments of the *3d* TM monolayers on Rh(001) are compared with the Ag(001) and Pd(001) substrates for the FM and AFM structures at the relaxed interlayer distances. The magnetic moments for on Rh(001) are smaller than those on Ag(001) or Pd(001) for the early TMs, while they are quite similar for the late TMs. This can be understood on the basis of the observation, that the overlap of the *d*-wavefunctions with the substrate is larger for the early than for the late TMs. Therefore, the dependence of the TMs magnetic moments on the chosen substrate is largest at the beginning of the TM series. The largest moment, in all cases, is found for Mn. The V and Ni magnetic moments vanish for the $c(2 \times 2)$ AFM structure. The induced magnetic moment of the Rh interface layer couples antiferromagnetically with Cr and ferromagnetically with Mn, Fe, Co and Ni, while almost no moment is induced by V. The largest induced magnetic moment is caused by the Co monolayer. The induced moments are much larger for Rh than for substrates like Ag(001), highlighting the importance of the substrate for magnetic properties like the magnetocrystalline anisotropy (MCA), which will be discussed later. Of course the AFM ordered TM films induce no magnetic moment in the interface Rh layer, and the induced moments in the deeper layers are considerably smaller (and of opposite orientation).

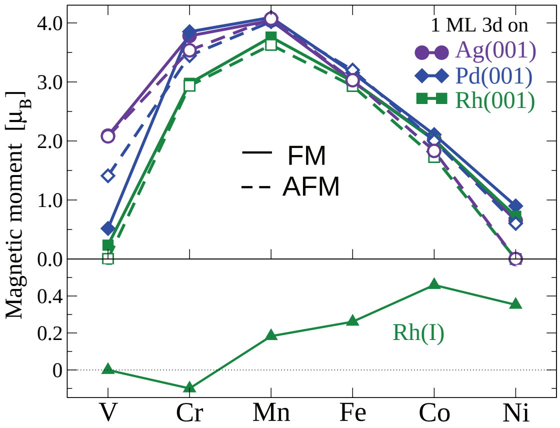

Figure 4.5: Magnetic moments of *3d* TM monolayers on Ag, Pd and Rh(001) surfaces (top) and the interface Rh moments (bottom). The TM moments are denoted by full (empty) symbols for the FM (AFM) solutions. For the FM case the magnetic moment of the interface Rh atoms is given by full green squares. The data for the *3d* TMs on Ag(001) and Pd(001) are taken from Ref.[3] and [5].

4.2.2 Magnetic order:

The total energy difference $\Delta E = E_{\mathrm{AFM}} - E_{\mathrm{FM}}$ between the $c(2 \times 2)$ AFM and the FM configuration is plotted in Fig.4.6 for the *3d* TM monolayers on different substrates. For the Rh(001) substrate, we found a FM ground state for V, Co and Ni, while it is $c(2 \times 2)$ AFM for Cr, Mn and Fe. The data for Ag(001) and Pd(001) are taken from Ref.[3] and [5]. For the V and Ni we see that the energy differences are small, 4 meV and 15 meV respectively. Experimentally, the case of 1 ML V on Ag(001) was discussed controversially, claiming ferromagnetic order [125, 126], or the absence of ferromagnetic order [127], as well as evidence for antiferromagnetic order [6]. Therefore, we checked ΔE carefully as function of several computational parameters, like **k**-point sampling of the temperature broadening at the Fermi level. No change in the magnetic order was found even in the presence of external electric fields. From Fig.4.6 we see for V and Cr a magnetic trend towards FM as we change the substrate from Ag through Pd to Rh, while an increasing tendency towards AFM is observed for Mn and the late TMs. We notice that the magnetic order of the 3d monolayers on Rh(001) changes when relaxations are included, which lead to change in magnetic order for Fe since it is close to the phase transition region. This highlights the importance of relaxations to predict the correct magnetic ground state, especially when the nearest neighbor interactions become weak and higher order interactions cannot be ignored as we will see later.

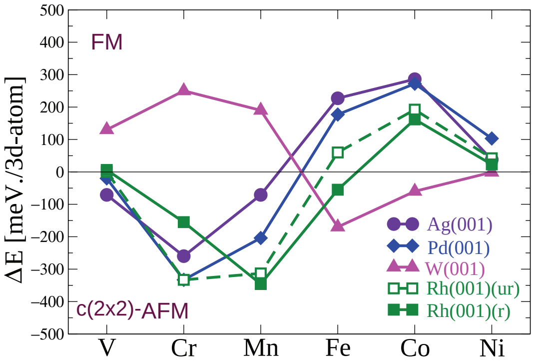

Figure 4.6: The magnetic order of *3d* TMs on Ag (circles), Pd (diamonds) Rh (squares) and W(001) (up triangles): positive $\Delta E = E_{\mathrm{AFM}} - E_{\mathrm{FM}}$ indicates a FM ground state, while negative values denote AFM order. The open squares connected by dashed line represent the magnetic order of unrelaxed *3d* TMs on Rh(001).

For a weakly interacting substrate, like Ag(001), the trends of ΔE can be understood on the basis of the densities of states of the TM monolayers[3]. As we move on to more strongly interacting substrates like Pd or Rh, this sinus-like curve is shifted gradually to the right, i.e. hybridization with the substrate effectively lowers the *d*-band filling in the TM film. This trend is even more pronounced for strongly interacting early TM substrates, like W(001), causing a complete reversal of the magnetic trends[7].

To analyze the role of the hybridization between the Fe ML and the Ag, Pd or Rh substrate, the local density of states (LDOS) for the nonmagnetic (NM) and the FM configuration of one ML Fe on different substrates are shown in Fig.4.7. We see from the NM LDOS, that there is no overlap of the Ag *4d*-band with the Fe DOS, that is pinned at the Fermi level due to its incomplete *3d*-band filling. Therefore, the Fe bandwidth is small and the high DOS at the Fermi level favors ferromagnetism. In contrast there is a strong *3d*-*4d* hybridization between the Fe ML and the Rh(001) substrate. The broadening of the Fe *d*-band reduces the DOS at the Fermi level leading finally to an antiferromagnetic ground state. The case of Fe/Pd(001) is in between these extremes, but still a FM order is obtained as a ground state. From the FM DOS it can be seen that a small FM moment can be induced in the Pd interface that is absent in the case of Fe/Ag(001).

We now compare Fe on Rh(001) to Cr/Rh(001), since the latter has a strong tendency towards a $c(2 \times 2)$ AFM ground state. From the NM LDOS (top of Fig.4.8) we see, that the Fermi level falls in a minimum of the Cr LDOS, favoring the AFM ground state even more than in the case of Fe (see Fig. 4.6). A comparison of the magnetic DOS shows that in Fe/Rh(001) the minority DOS is pinned at the Fermi level, while in the Cr

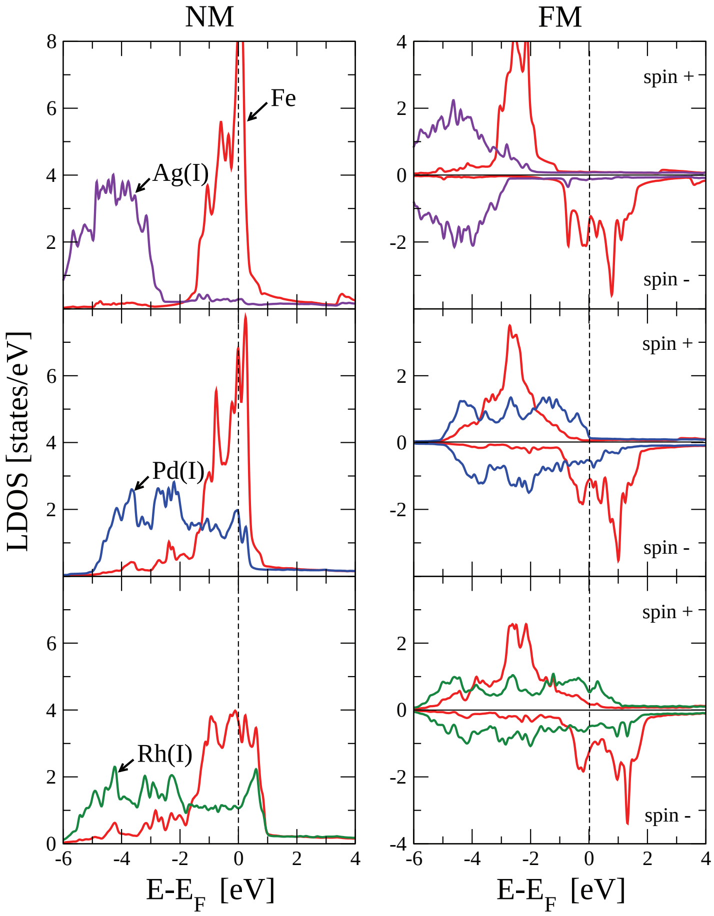

Figure 4.7: Local densities of states (LDOS) for the Fe atoms and the substrate atoms at the interface (I) for the nonmagnetic (NM) and FM configurations of Fe on Ag(001), Pd(001) and Rh(001).

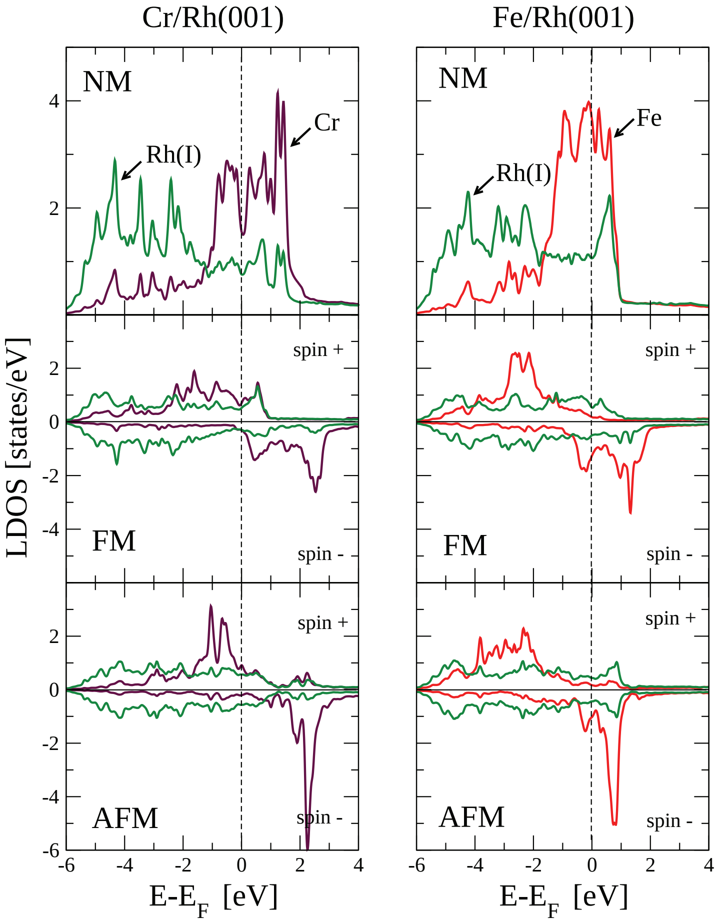

Figure 4.8: LDOS for the NM, FM and AFM configurations of Fe and Cr on Rh(001) surface.

case the position of the majority *d*-band is determined by the band-filling and the whole exchange-split *d*-like DOS is energetically at a much higher position. This modifies the hybridization to the substrate, as can be seen in the relaxations: while Fe and Cr have very similar bulk lattice constants, the relaxation of FM Cr on Rh(001) is much bigger than FM Fe/Rh(001) relaxation (see Fig. 4.4). In the case of the AFM solutions the trend is exactly opposite, i.e. Fe relaxes much stronger than Cr. Additionally, the Rh(I) AFM LDOS majority and minority bands, in both Fe and Cr cases, are completely identical (since there is no induced moments), while its FM LDOS Rh(I) majority and minority bands are distorted. The AFM minority DOS at Fermi is smaller than the FM one in both Fe/Rh(001) and Cr/Rh(001) systems. This indicates that the stability (instability) of the Fe and Cr AFM (FM) solution is related to the bands values at the Fermi level. In the AFM case also the *d*-bandwidth is much smaller than in the FM case. In all these cases the magnetic moments are approximately the same (Fig. 4.5).

4.2.3 Magnetocrystalline anisotropy:

Focusing on the calculation of the E_{MCA}, there are two ways to do that. The first is using the total energy approach, were it should converge for each chosen spin quantization axis and then the energy difference is E_{MCA}. Another way to calculate E_{MCA} is using the force theorem[128] which should be, in principle, applicable up to linear changes in the charge and magnetization densities, as the magnetization is rotated from one direction to another[129]. This theorem states that E_{MCA} is given by the difference in band energies (sum of valence eigenvalues) obtained with spin-orbit coupling for two different spin-quantization axes, using the same self consistent scalar-relativistic potential.

$$E_{MCA}^{FT} = \sum_i^{occ} \epsilon_i^{\perp} - \sum_i^{occ} \epsilon_i^{\parallel} \tag{4.2}$$

From this, E_{MCA} is represented by forming the difference of the sum of the occupied eigenvalues of the Hamiltonian taken for the out-of-plane ($\perp$) and in-plane ($\parallel$) spin directions respectively, provided that the same effective potential is used when the Kohn-Sham equation is solved. This method has the great advantage that only one nonrelativistic self-consistent calculation of the potential must be done. Numerical evidence was provided by O. Eriksson that the MCA of 3d elements are rather well reproduced using the force theorem, and that it gives results similar to total energy calculations[130]. In addition, difference between the total energy and force theorem calculations of the E_{MCA} should be smaller than the numerical accuracy of the total energy calculations. By that, converged potentials are computed within DFT without spin-orbit coupling and then one extra iteration.

Because of the lack of symmetry, a huge number of **k** points necessary to achieve convergence of the integrals in the Brillouin zone (BZ) involved in the calculation of the E_{MCA}. Using self consistent (SC) calculations (Fig. 4.9), we tested the MCA convergence versus the number of k-points up to 1024 $k_{\parallel}$-points in the full 2DBZ. After that we calculated

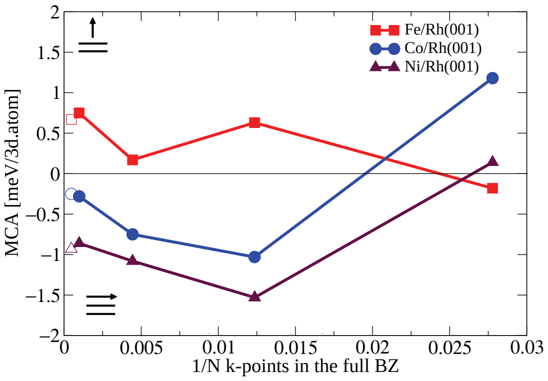

Figure 4.9: Solid symbols are the MCA values of Fe, Co and Ni monolayers on Rh(001) as a function of 1/k obtained from SC calculations. Open symbols represent the force theorem results with 2048 $k_{\|}$-points in the full BZ. MCA>0 (<0) means out-of-plane (in-plane) easy axis.

MCA, using force theorem, with 2048 $k_{\|}$-points and found no change in the easy axis prediction, with 0.1, 0.03 and 0.1 meV/$3d$ difference from the SC results fro Fe, Co and Ni respectively. We did one selected MCA calculation using force theorem with about 4000 $k_{\|}$-points and there was no change compared to the 2048 $k_{\|}$-points MCA value.

We start with the unsupported *3d* monolayers (UML) using the Rhodium lattice constant for FM and c(2×2)-AFM. The results are shown in figure 4.10. For strong ferromagnetic elements (Fe, Co and Ni), it is clear from the figure that the orbital moments are the source of MCA as suggested by Bruno (see sec.3.4). This is obvious since the splitting between the majority and minority local spin moments is strong in these elements in both FM and AFM spin configurations, even if the spin-orbit coupling is included (Fig. 4.12 and 4.11). This gives the rise to a strong orbital moment anisotropy that determines the easy magnetization axis. On the other hand, the situation is not clear, especially for the AFM calculation in case of V and Cr UMLs, were the magnetization easy axes is opposite to the orbital moments anisotropy Δm_l shown in figure 4.10.

In the case of supported monolayers, the E_{MCA} of one ML *3d*/Rh(001) for the FM and AFM configurations is shown in figure 4.13. We cannot trace the substrate effect out of that, since there is an in-plane MCA tendency for V, Cr, Mn and Fe, while there is and out of plane tendency of the MCA for Co and Ni. First we try to explain our MCA results from the orbital moments anisotropy (OMA) in the frame of Bruno model. From the FM results we find good agreement between the MCA and OMA of Co ($-0.041\ \mu_B$) and Ni ($-0.025\ \mu_B$), while we are not able to explain the MCA of V, Cr, Mn and Fe because of their tiny OMAs ($< 0.002\,\mu_B$). From the AFM results, OMAs of Cr ($+0.014\ \mu_B$), Mn ($-0.022\ \mu_B$),

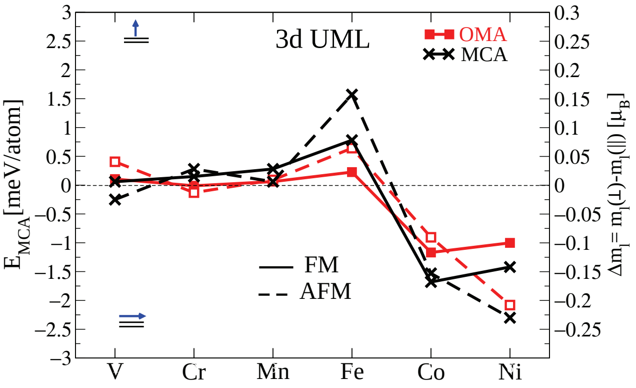

Figure 4.10: Magneto-crystalline anisotropy (MCA) for $3d$ UML is presented as ($\times$) connected by solid (dashed) black line for FM (AFM) configuration. The orbital moments anisotropy (OMA) Δm_l for FM (AFM) case is presented as filled (empty) squares connected by solid (dashed) red line. Note that the scale on the normal (MCA) is different from the opposite (OMA) y-axis.

Fe ($-0.015\ \mu_B$) and Co ($-0.056\ \mu_B$) do fully agree withe the calculated MCA values.

For more understanding of the substrate effect on MCA, we need to check the influence of the crystal field and the hybridization. For the crystal field effect, we calculated the *3d* contribution in the MCA, by excluding the spin orbit coupling of the substrate atoms. We can see that the crystal field prefers the in-plane MCA. To see the effect of the induced moments in the substrate, we calculated the MCA for the $c(2\times2)$ AFM, where there are no induced moments for the substrate interface layer Rh(I). By that we understand that the induced moments, i.e. the hybridization strength, pushes the magnetization to be out of plane. This means that the out of plane tendency is coming from the hybridization between the *3d* ML and the Rh(001) substrate. One should mention that Cr has an opposite trend to what we concluded because it has negative induced moments.

Knowing the MCA value enables us to estimate Néel temperature for ferromagnets with uniaxial anisotropy as explained in subsection 3.4.1. If we want to use equation (3.59), then we need an estimated value of the nearest neighbor exchange interaction constant J_1 obtained from classical Heisenberg model (sec. 3.2). The FM has $-2J_1M^2$ on square lattice and $+2J_1M^2$ for AFM configuration, then the energy difference between FM and AFM is equal to $4J_1$. From the obtained results of the magnetic order from total energy calculations (subsec. 4.2.2), we can estimate Néel temperature for $3d$ monolayers which have uniaxial anisotropy on Rh(001). This implies only on vanadium and Cr since it has FM with out-of-plane MCA. Using equation (3.59) and the bulk experimental Néel temperatures, we

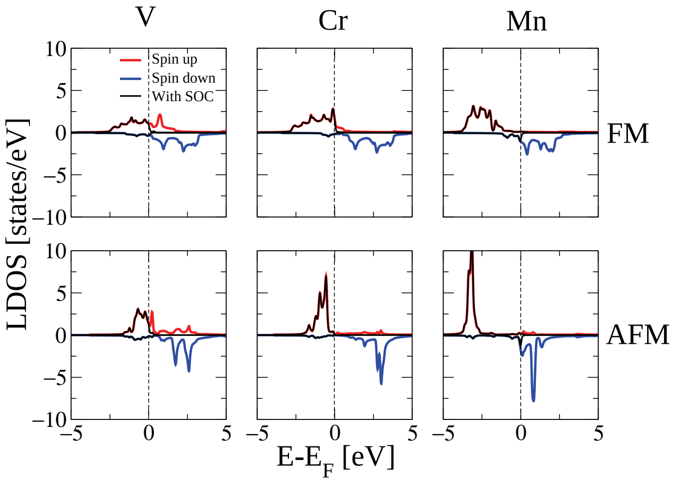

Figure 4.11: Local spin density of states for UMLs of V, Cr and Mn for both FM and AFM configurations. Red (blue) solid line represents majority (minority) spin states without including the spin-orbit coupling interaction. The black solid represents the local density of state for both spin channels with spin-orbit coupling up to the Fermi level.

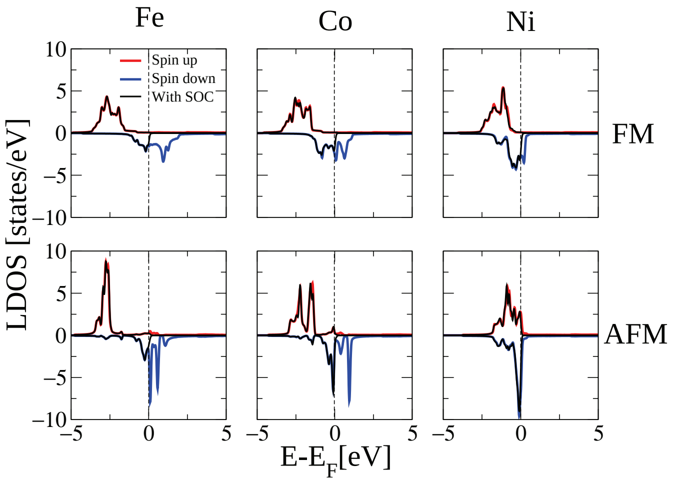

Figure 4.12: Local spin density of states for UMLs of Fe, Co and Ni for both FM and AFM configurations. Red (blue) solid line represents majority (minority) spin states without including the spin-orbit coupling interaction. The black solid represents the local density of state for both spin channels with spin-orbit coupling up to the Fermi level.

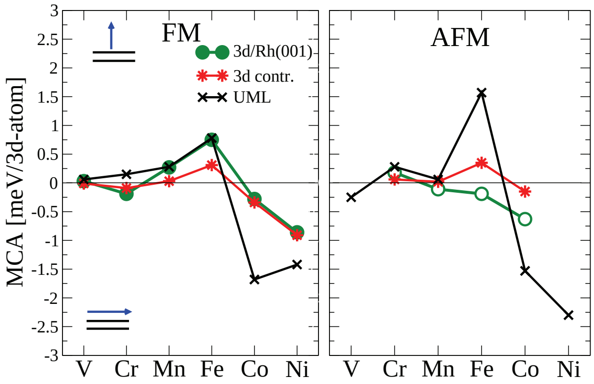

Figure 4.13: Magneto-crystalline anisotropy (MCA) for 1 ML 3*d*/Rh(001). The FM (AFM) case is presented as filled (empty) symbols. (×) are the MCA of the unsupported monolayers, while the (*) represents the *3d* MCA contribution. Positive MCA means an out of plane and negative MCA means in-plane magneto-crystalline anisotropy.

estimate $T_c^{(2D)}$ for V and Cr monolayers on Rh(001) to be 3K and 285K, respectively. We also "can" estimate Fe Néel temperature to be larger than 260 K, keeping in mind that we used the FM out-of-plane MCA value, since there is no theoretical way to estimate Néel temperature for in-plane anisotropies. To justify our estimated Néel temperature of Fe monolayer on Rh(001), we find it close to what was estimated for Fe monolayer on W(001) surface, 240-260 K[131].

In table4.1, we present a summary of all results we obtained for 3*d* monolayers on Rh(001). It includes the 3*d* and Rh(I) relaxations, 3*d* spin moments, 4*d* induced spin moments, magnetocrystalline anisotropy, orbital moments and the total energy differences between the FM and c(2×2)-AFM configurations. We could show that Cr, Mn, Fe do have a c(2×2)-AFM while V, Co and Ni monolayers prefer to order ferromagnetically on Rh(001) substrate. From the calculated MCA values we found that only V and Cr have an out-of-plane magnetization easy axis. We also could interpret our MCA results of the 3*d* unsupported and supported monolayers according to Bruno model by using their orbital moments anisotropies (OMA). Additionally, we tried to understand the influence of the crystal field and the on the 3*d* MCA. We concluded that the crystal field prefers the in-plane, while the out-of-plane tendency comes from the 3*d*-Rh(I) hybridization. From the obtained total energy differences and MCA values we could estimate the critical temperature of V and Cr. In the next section, we will move to describe the magnetic properties of the 3*d*-TMS monolayers on Rh(111) surface.

Table 4.1: Summary of Relaxations, Δd_{12} and Δd_{23}, $3d$ and Rh(I) magnetic moments, MCA, OMA and total energy differences results of $3d$-TMs monolayers on Rh(001) substrate.

	V	Cr	Mn	Fe	Co	Ni
FM:						
Δd_{12} (%)	-7.4	-11.7	-7.4	-7.4	-13.3	-12.8
Δd_{23} (%)	$+6.9$	$+6.7$	$+3.0$	$+2.2$	$+2.8$	-0.7
$3d$ moments [μ_B]	0.23	2.98	3.76	3.01	2.01	0.73
Rh(I) moments [μ_B]	0.00	-0.10	$+0.18$	$+0.26$	$+0.46$	-0.35
MCA [meV/$3d$]	$+0.03$	-0.19	$+0.27$	$+0.75$	-0.28	-0.86
OMA Δm_l [μ_B]	0.00	-0.002	$+0.001$	-0.001	-0.041	-0.025
AFM:						
Δd_{12} (%)	-7.4	-5.2	-9.6	-12.8	-13.5	-13.5
Δd_{23} (%)	$+6.9$	$+3.2$	$+3.8$	$+4.5$	$+2.2$	$+0.7$
$3d$ moments [μ_B]	0.00	2.94	3.63	2.93	1.73	0.00
Rh(I) moments [μ_B]	0.00	0.00	0.00	0.00	0.00	0.00
MCA [meV/$3d$ atom]	-	$+0.18$	-0.11	-0.19	-0.63	-
OMA [μ_B]	0.00	$+0.014$	-0.022	-0.015	-0.056	0.00
$E_{AFM}-E_{FM}$ [meV/$3d$]	$+6$	-155	-346	-55	$+162$	$+23$

4.3 $3d$-Monolayers on Rh(111) Substrate:

Magnetic properties of V, Cr, Mn, Fe, Co and Ni monolayers on the hexagonal Rh(111) surface will be explained in this section. We followed the same procedure as in the previous section (4.2). By studying the magnetic properties of (111)-oriented surfaces, we will see the effect on the magnetic properties when increasing the coordination number in the magnetic layer from 4, in square lattices, to 6 in hexagonal lattices. The (111) results, especially for Fe, will be helpful to investigate its magnetic ground state, especially since we have hexagonal substrates, where frustrations may occur due to their triangular lattices. All calculations were performed in the same way as outlined in sec. 4.2.1. The computational parameters were also not changed, keeping in mind that we have hexagonal k-point mesh, with 36 $k_{\parallel}$-points in the 2DIBZ.

4.3.1 Relaxations and magnetic moments:

The structural relaxations were performed for V, Cr, Mn, Fe, Co, and Ni monolayers on Rh(111) substrate for two magnetic configurations, FM (with one atom/unit cell) and the RW-AFM (with 2 atoms/unit cell) as illustrated in figure 4.14. For Cr (V), there was no stable FM (AFM) collinear solution. The FM and AFM relaxations of $3d$/Rh(111) are presented in figure 4.15 and compared to the $3d$/Rh(001) results.

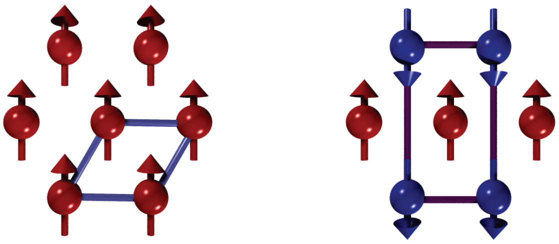

Figure 4.14: FM (left) and RW-AFM (right) unit cells of hexagonal lattices.

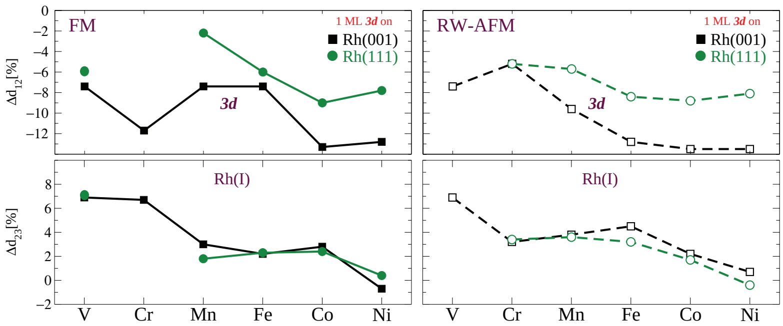

Figure 4.15: Change of the first and second interlayer spacing, Δd_{12} and Δd_{23}, respectively, for *3d* TM monolayers on Rh(111) (circles) and Rh(001) (squares). Solid (dashed) lines indicate the FM (RW-AFM) results. The corresponding changes are given with respect to the substrates bulk interlayer spacing along [111] ([001]), which is 2.21 Å(1.91 Å).

From figure 4.15 we notice that the smallest Δd_{12} inward FM relaxation of the *3d* monolayer occurs again for Mn on Rh(111), as it is for the case on Rh(001). This is due to the strong magneto-volume effect of Mn, which is reflected in the large Mn magnetic moments, which compensate most efficiently the strong inward relaxation caused by the larger Rh lattice constant. For the close packed (111) surfaces, the unit cell volume is smaller, therefore the inter-atomic distances will get smaller, and then their relaxations are expected to be smaller than in the (001) surface. This can bee seen in our comparison between $3d$/Rh(111) and $3d$/Rh(001) FM and AFM relaxations. We notice that there is only small difference of Fe FM relaxations between Rh(001) and Rh(111), compared to almost similar change for Mn, Co and Ni FM relaxations, although Fe has larger magnetic moments than Co and Ni on Rh(111) as well as on Rh(001). This indicates that there are other factors than the magneto-volume effect, which might arise from the hybridization effects between Fe-Rh(111) and Fe-Rh(001) in a similar manner.

For the Rh(111) substrate, the outward FM relaxation of the Δd_{23} interface layer, Rh(I), was largest (smallest) for Co (Ni). In the case of Fe/Rh(111), Δd_{23} was very similar to Fe/Rh(001) in the FM case. The AFM relaxations of Rh(I) where smaller in case of Rh(111) than the ones on the Rh(001) substrate.

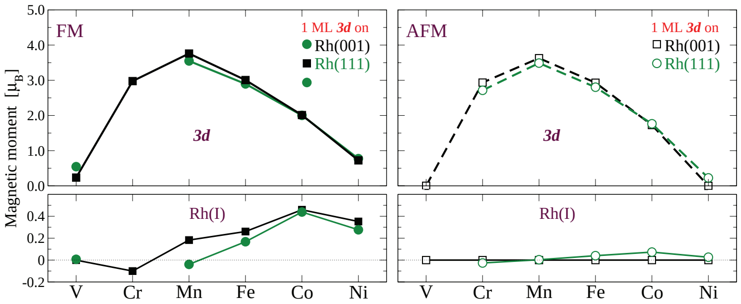

Figure 4.16: Magnetic moments of *3d* TM monolayers on Rh(111) (circles) and Rh(001) (squares) surfaces, and the interface Rh moments. Solid (dashed) lines represents FM (AFM) solutions. There is no FM solution for Cr/Rh(111) and no RW-AFM solution for V/Rh(111).

In Fig. 4.16 the magnetic moments of the *3d* TM monolayers on Rh(111) are compared with the Rh(001) substrates for the FM and AFM solutions at the relaxed interlayer distances. In both solutions, the magnetic moments of the early $3d$ monolayers on Rh(111) are smaller than on on Rh(001). This is in agreement with Stoner model, were magnetism is enhanced with smaller coordination number and larger magnetic moments are expected on (001) than on (111) and the overlap of the *d*-wavefunctions with the substrate is larger for the early than for the late TMs, as we see for Mn. Therefore, the dependence of the TMs magnetic moments on the chosen substrate is largest at the beginning of the TM series. The largest moment, in all cases, is found for Mn. Ni moments didn't vanish for the RW-AFM solution on Rh(111), as for $c(2 \times 2)$-AFM on Rh(001) substrate.

For the ferromagnetic solutions of $3d$/Rh(111), the induced magnetic moment of the Rh interface layer couples antiferromagnetically with Mn and ferromagnetically with Fe, Co and Ni. The large difference between Rh(I) induced moments by Mn is due to the 6% difference between Mn/Rh(111) and Mn/Rh(001) FM relaxations (Fig. 4.15), which shows that the strong magneto-volume effect Mn is more weakly affected on Rh(111) than on the the Rh(001) surface.

In the case of the RW-AFM solution of $3d$/Rh(111), the interface Rh layer has finite induced magnetic moments, while the $c(2 \times 2)$-AFM ordered films induce no magnetic moment. The reason is that the Rh(I) atoms, in case of RW-AFM ordered magnetic films on hexagonal structures, are located below three magnetic atoms with a non-zero net magnetization, where as the Rh(I) atoms have four atoms as neighbors with zero net moments on square lattices. Additionally, the RW-AFM structure is not the only possible anti-ferromagnetic spin configuration on hexagonal substrates due to spin frustrations on triangular lattices as we will see later. Therefore, Rh(I) atoms will always have induced moments in case of any collinear AFM arrangement on hexagonal surfaces, although the are considerably small compared to those where induced ferromagnetically.

Table 4.2: Results of optimized interlayer distance (in Å), obtained from FM (AFM) relaxations, between $3d$ monolayer and Rh(I) of Rh(001) and Rh(111) substrates.

	V	Cr	Mn	Fe	Co	Ni
Rh(001)	1.77 (1.77)	1.69 (1.81)	1.77 (1.73)	1.77 (1.67)	1.66 (1.65)	1.67 (1.65)
Rh(111)	2.07 (-)	- (2.09)	2.16 (2.08)	2.07 (2.02)	2.01 (2.01)	2.03 (2.03)

The largest induced magnetic moments are caused by the Co and Ni monolayers on both Rh surfaces. This is due to their strong ferromagnetism and strongest inward relaxations with smallest interlayer distance from Rh(I) as shown in table 4.2. The induced moments from the FM calculations are larger for Rh(001) than for Rh(111) substrate due to the difference in the coordination number, as well as smaller $3d$-Rh(I) interlayer distance. For the RW-AFM results, the Rh(I) atoms have almost zero magnetic moments induced by Cr or Mn, where they are noticeable for Fe, Co and Ni because of their large inward relaxations on Rh(111) (see fig. 4.15(right))

4.3.2 Magnetic order:

Collinear calculations were performed to calculate the total energy difference $\Delta E = E_{\mathrm{AFM}} - E_{\mathrm{FM}}$ between the RW-AFM and the FM relaxed configurations. The results are plotted in Fig.4.17 for the *3d* TM monolayers on Rh(111)substrate, and compared to Rh(001) substrate results. For the Rh(111) substrate, we found that FM solution is more stable for Fe, Co and Ni, while it is $c(2 \times 2)$ AFM for Mn. As mentioned above, Cr (V) has no stable FM (RW-AFM) solution on Rh(111), therefore we are unable to calculate total energy difference. Except for Fe, the results of Rh(111) substrate show no difference in the $3d$ magnetic order from what we obtained on the Rh(001) substrate.

Using equation (3.11), a stronger tendency towards ferromagnetism is expected for large nonmagnetic LDOS at Fermi level, which means smaller band width (eq. 3.14) and then smaller coordination number (eq. 3.16), keeping the nearest neighbor distance constant. For different magnetic configurations of Fe on Rh substrate, we calculated the local density of states of the Fe monolayer on Rh(111) surface, and then compare the results to Fe density of states on Rh(001) as shown in figure 4.18. From the nonmagnetic calculations, we see that the Fe LDOS –at Fermi level– on Rh(001) is larger than Fe NM LDOS on Rh(111) substrate. These nonmagnetic results of LDOS agrees with the expectation that systems with large coordination number will have wider band width and then smaller nonmagnetic density of states, which is the case for Fe/Rh(111) NM LDOS. But according to the Stoner model, Fe/Rh(001) should be more FM than on Rh(111).

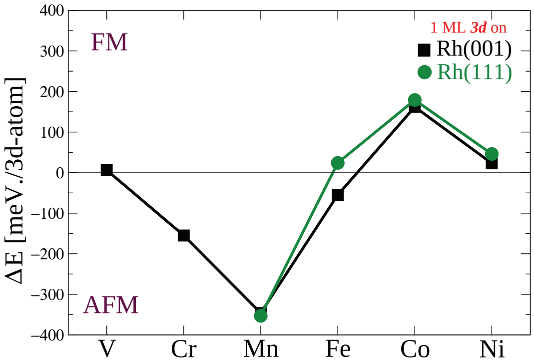

Figure 4.17: Total energy difference for different magnetic order of *3d* TMs on Rh(111) (circles) and Rh(001) (squares) surfaces: positive $\Delta E = E_{\mathrm{AFM}} - E_{\mathrm{FM}}$ indicates that FM is more stable, while negative values denote AFM order.

From the magnetic LDOS, we see that in the case of Fe/Rh(001) Fe has larger FM LDOS AFM, therefore the AFM configuration is more stable, while Fe FM is smaller than the AFM LDOS in the case for Fe/Rh(111) leading to more stability of FM solution.

Finally, we should notice that we calculated Fe ground state on Rh(111) by total energy difference between FM and the RW-AFM configurations, but on hexagonal lattices, the magnetic spins are frustrated if they prefer to align anti-ferromagnetically. In our comparison between Fe/Rh(111) and Fe/Rh(001) we chosen the collinear RW-AFM spins arrangement on Rh(111) surface, which is not the only collinear solution to construct an anti-ferromagnetic structures on hexagonal substrates. There are many collinear and non-collinear spin structures where the spins might align non-ferromagnetically in two or three dimensions, simplest example is the famous 120° Néel magnetic structure on hexagonal lattice. This leads us to further investigations in next chapter to find the true magnetic ground state of Fe on Rh(111) and other hexagonal substrates.

As a conclusion of this chapter, We employed the full-potential linearized augmented plane-wave method to report a systematic density-functional study of the magnetic properties of the 3*d* transition-metal (V, Cr, Mn, Fe, Co and Ni) monolayers deposited on the Rh(001) and Rh(111) substrates. Performing collinear calculations, we relaxed our structures using atomic force calculations, and compared the FM and AFM relaxations on both Rh surfaces. we found, all monolayer films are magnetic. The size of the local magnetic moments across the transition-metal series follows Hund's rule with a maximum magnetic moment of 3.77 μ_B for Mn. The largest induced magnetic moment of about 0.46 μ_B was found for Rh atoms adjacent to the Co-film on Rh(001). When relaxations are included, we predict a ferromagnetic (FM) ground state for V, Co and Ni, while Cr,

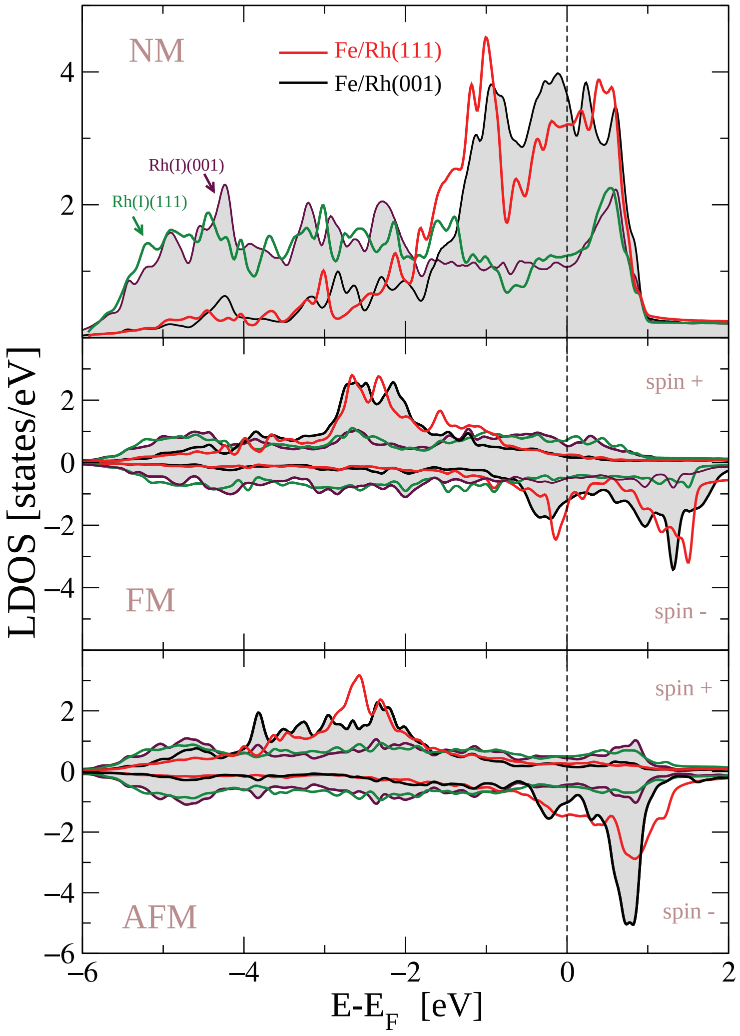

Figure 4.18: Local densities of states (LDOS) for the Fe atoms (red solid line) and the substrate atoms (green solid line) at the interface (I) for the nonmagnetic (NM), FM and AFM configurations of Fe on Rh(111) compared to the Fe LDOS on Rh(001) substrate (gray shaded black and purple lines).

Mn and Fe favor a $c(2 \times 2)$ antiferromagnetic (AFM) state, a checkerboard arrangement of up and down magnetic moments, on Rh(001) substrate. The Rh(111) substrate didn't change the magnetic ground state but for Fe, where it changes from AFM on Rh(001) to FM on Rh(111). The magnetic anisotropy energies of these ultrathin magnetic films are calculated for the FM and the AFM states. With the exception of Cr and V, the easy axis of the magnetization is predicted to be in the film plane. To gain an understanding of the $c(2 \times 2)$ AFM state of Fe/Rh(100), we analyzed this result with respect to the trends of the magnetic order of $3d$ monolayers on other $4d$ substrates, such as Pd(100) and Ag(100). The FM ground state of Fe monolayer on Rh(111) couldn't be explained from the NM density of states and the Stoner model. In next chapter we will show our non-collinear calculations to predict Fe magnetic ground state on different hexagonal substrates. We will use a model Hamiltonian derived from the classical Heisenberg model to extract the exchange interaction parameters. The magnetocrystalline anisotropy (MCA) was calculated only for $3d$/Rh(001). MCA of $3d$/Rh(111) will be discussed separately in the last chapter.

Chapter 5

Fe monolayers on hexagonal nonmagnetic substrates

Describing the magnetic order of the square lattices (001) monolayers, using Heisenberg model equation (3.22) up to the second nearest neighbor interaction (J_1, J_2), is relatively simple. As long as the nearest neighbor interaction is the dominating one, there are only two phases to be considered: the ferromagnetic p(1×1) structure ($J_1 > 0$) the antiferromagnetic c(2×2) superstructure ($J_1 < 0$). If we describe the solution of the Heisenberg model as spin-spirals with a $\mathbf{q}_{\|}$-vector from the first Brillouin zone, the c(2×2) structure corresponds to the M-point in the 2DBZ of the square lattice. If the next-nearest neighbor interaction is antiferromagnetic, $J_2 < 0$, and sufficiently strong, $|J_1| < 2|J_2|$, then the ground state changes to be magnetic structure with a 2D$\mathbf{q}_{\|}$ vector at the $\overline{\mathrm{X}}$-point in the 2DBZ. This means that an anti-ferromagnetic p(2×1) or p(1×2) structure (ferromagnetic rows of atoms along the [001] or [010] direction coupling antiferromagnetically from row to row) becomes the magnetic ground state.

A recent theoretical study was preformed to predict the magnetic ground state of Fe monolayers on a $\mathrm{Ta}_x\mathrm{W}_{1-x}$ alloy if the substrate is tuned by changing the Ta concentration x[14]. Non-collinear magnetic structures at critical Ta concentration were predicted. This means that complex magnetic order can be obtained even in single monolayer (ML) magnetic films on non-magnetic (001) substrates. Furthermore, recently a spin-spiral state was discovered for a Mn ML on W(110) [132] and for a Mn ML on W(001) [12], although the driving force in this case is not a Heisenberg-type interaction but rather Dzyaloshinskii-Moriya type exchange. As a result, one can control the magnetic order of $3d$ monolayer by tuning the substrate.

By that, the investigation of the magnetic order on square lattices started from late (Ag, Pd) and ended with early (W) transition metals substrates as illustrated in figure (5.1). For the hcp elements there is no square lattices which could help to have a complete understanding of the magnetic order trend of $3d$ monolayers on nonmagnetic substrates. Our case of study focuses on Fe because it has intensively been studied theoretically and experimentally.

This leads us to continue investigating the Fe magnetic ground state on hexagonal sub-

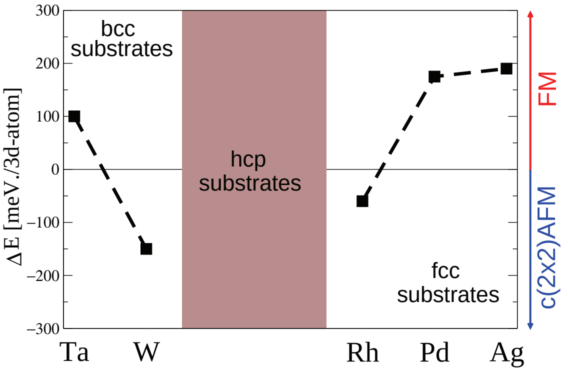

Figure 5.1: Total-energy difference between the FM (ground state if $\Delta E > 0$) and c(2×2)-AFM ($\Delta E < 0$) configuration for Fe MLs on (001) surfaces.

strates. This will increase the understanding of their magnetic trend. Hexagonal surfaces of $4d$- and $5d$-transition metals such as Re, Ru, or Ir have been particularly attractive from an experimental point of view as ultra-thin $3d$-TM films can often be grown pseudomorphically and without intermixing [133, 134, 135, 136, 137]. However, there has been a controversy in the past about reports ultra-thin films on these surfaces [135, 136]. The fundamental key to many unresolved puzzles may be the itinerant character of transition metals resulting in competing exchange interactions beyond nearest-neighbors and higher-order spin interactions beyond the Heisenberg model.

For our case of study, Fe films on Rh(111) substrate, we present in this chapter a systematic study to find and explain the true magnetic ground state. In the first section, we show our results obtained from collinear calculations of Fe ground state on $4d(111)$ TMs, Ag, Pd, Rh, Tc and Ru, and compare them with other results obtained for Fe monolayer on $5d$ TMs. In second section, we show our non-collinear calculations results of Fe monolayer on Rh(111) and Tc(0001) substrate. We will also explain the role of the higher order interactions through a model Hamiltonian which goes beyond the classical Heisenberg model by including the higher order terms originated from the biquadratic and 4-spin interactions as were presented in section (3.2). At the end of the chapter we will show an overall comparison of the predicted Fe ground state on different $4d$ and $5d$ substrates.

5.1 Results of Fe monolayer on different hexagonal substrates from collinear calculations:

From the performed collinear calculations on Fe monolayer on Rh substrate (see previous chapter), it remained unclear whether the FM state is the ground state of an Fe monolayer on Rh(111). In this section we present a theoretical comparison of magnetic properties of Fe monolayer on different $4d$ hexagonal substrates. Since we have Fe results on Pd, Rh and Tc, we will add to our comparison the Ru results obtained in reference [57].

The electronic and magnetic properties were determined based on density-functional theory. Calculations have been carried out in the generalized gradient approximation (GGA) to the exchange-correlation functional [138] using the full-potential linearized augmented plane wave (FLAPW) method, as implemented in the FLEUR code [50, 56]. All calculations have been performed in the scalar-relativistic approximation, i.e. neglecting the effect of spin-orbit coupling. The collinear magnetic states were investigated in systems modeled by 7 layers of $4d$-TM substrate with hcp or fcc stacking covered by a pseudomorphic Fe monolayer on each side of the films. We have used the theoretical lattice constants obtained by GGA calculations (see table5.1), which are in good agreement to the the experimental values. Both, the FM and the RW-AFM configurations were relaxed. We used about 120 LAPW basis functions per atom with a muffin-tin radius of 1.22 Åfor the Fe monolayer atoms and 1.28 Å for the $4d$ substrate atoms. we used 2.17Å value for the cutoff of the plane wave expansion of wavefunctions. The irreducible part of the two-dimensional Brillouin zone (I2DBZ) was sampled with 36 $\mathbf{k}_{\|}$-points to determine the relaxations and the energy differences between the different magnetic configurations with the same two atomic unit cell.

5.1.1 Structural optimization & relaxations:

The relaxations and magnetic moments of Fe monolayers on $4d$-TM substrate are shown in Table 5.1. All relaxations are calculated using equation (4.1). We relaxed the topmost, $3d$ and $4d$(I) layers. The Fe stacking on the $4d$ substrate was checked. Fe prefers to be fcc on Pd and hcp stacking on Rh(111) and Tc(111). It also prefers hcp stacking with Ru(0001) [57]. It is important to mention that relaxing only the top most monolayer is not enough to have good understanding of what affects the interlayer $3d$-$4d$ relaxed distance. For example, in reference [57], relaxations were done only for the Fe monolayer, while the substrates interface layer Ru(I) was not relaxed. Having the same relaxations conditions, we tested Fe on Ru(0001) FM relaxations including the Ru(I) layer. We found that the optimized Fe-Ru(I) interlayer distance, d_{12}, is 2.08 Å instead of 2.18 Å in ref. [57]. This means that, we cannot have quantitatively predict of what affects the $3d$-$4d$ interlayer optimized distance, which is very helpful to trace the magnetic interactions between the $3d$ and $4d$ monolayer. The FM relaxations of Fe monolayer on $4d$ hexagonal substrate obtained from collinear calculations are shown in table 5.1. We don't show here the AFM relaxations, because of frustrations on triangular lattices which makes it difficult to predict which the optimum collinear AFM arrangement for our comparison.

From table (5.1), we see that the relaxations of the $3d$ monolayer were all directed inwards to the substrate. This is due to the large lattice mismatch between the $3d$ and $4d$ bulk lattice constants. From the interlayer distance, d_{12}, between the $3d$ monolayer and the $4d$ interface layer, one can explain the origin of the relaxations of $3d$ on different substrates. Mainly, three major factors that affect Fe interlayer distance on the substrate

Table 5.1: Results for the structural FM relaxations and magnetic moments. a_0 is the calculated in-plane lattice constant using GGA, Δd_{12} are the relaxations of the $3d$ monolayer in (%). Δd_{23} are the relaxations of the interface monolayer in (%). Positive (negative) Δd_{ij} defines if the relaxation direction has an outward (inward) direction. The interlayer distance d_{12} is in Ångstroms. Fe/Ag(111) are taken from Ref. [38]. Experimental in-plane lattice constants are taken from Ref.[120]

	a_0 (exp.)Å	Δd_{12}(%)	Δd_{23}(%)	d_{12} [Å]	m_{Fe} (μ_B)
Fe/Ag(111)	2.93 (2.89)	-8.8	$+0.4$	2.17	3.09
Fe/Pd(111)	2.79 (2.75)	-10.7	$+3.1$	2.04	3.09
Fe/Rh(111)	2.70 (2.69)	-6.0	$+2.3$	2.07	2.89
Fe/Ru(0001)	2.72 (2.70)	-3.4	-1.1	2.06	2.75
Fe/Tc(0001)	2.72 (2.74)	-5.2	-1.2	2.08	2.64

(i. e. relaxations): Geometry, magnetic moments through the magneto-volume effect and the hybridization with the substrate. The geometrical effect can be seen by calculating the Fe-$4d$(I) bulk interlayer distance, d^{bulk}_{Fe-4d} using constant Fe fcc volume along [111]. Due to the difference between Fe and $4d$ lattice constants, we averaged the Fe-$4d$(I) bulk interlayer distance

$$d^{Fe-4d}_{bulk} = \frac{1}{2}(d^{Fe-Fe}_{a_{4d}} + d^{4d-4d}_{a_{4d}}) \tag{5.1}$$

where $d^{Fe-Fe}_{a_{4d}}$ is the Fe-Fe bulk interlayer distance using the $4d$ in-plane lattice constant a_{4d} keeping the Fe bulk volume to be constant, and $d^{4d-4d}_{a_{4d}}$ is the $4d$ bulk interlayer distance. Figure 5.2 shows optimized values of d_{Fe-4d} in relation to the in-plane $4d$ lattice constant. The difference between the optimized interlayer distances and the bulk values (eq. 5.1) represents the magneto-volume and hybridization effects. For large moments, like on Pd and Ag, one would expect large magneto-volume effect as we see an Ag case, but we find smaller optimized d_{12} for Fe-Pd than the bulk value, although Fe has similar calculated spin moments on Pd as on Ag. This can be explained by the fact that hybridization between Fe monolayer and Pd(I) are stronger than between Fe and Ag(I), which defeat the magneto-volume effect. This is consistent with our results from section(4.2.2). For Fe on Rh, we see that there is a competition between the magneto-volume effect and hybridization to optimize the Fe-Rh(I) interlayer distance. For Ru and Tc, which are hcp substrates, the magneto-volume effect is stronger in Ru, due to higher Fe moments, whereas the optimized Fe-Tc interlayer distance can be driven by stronger hybridization between Fe and Tc. In terms of band filling, we see how the d-band filling increases Fe magnetic moments if we tune the substrate from left to right among the $4d$-transition metals series, i. e. from Tc to Ru, Rh, Pd and Ag.

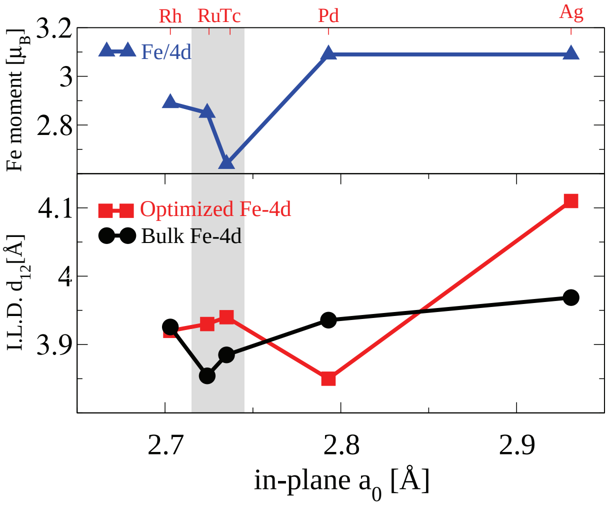

Figure 5.2: The bulk Fe-4*d* interlayer distance according to eq.(5.1) with difference in-plane lattice constants for Tc, Ru, Rh, Pd and Ag (black circles), the optimized Fe-4*d* interlayer distance (red squares), and Fe local spin moments on different substrates. Shaded area includes hcp elements.

5.1.2 Magnetic order:

After having understood the origin of the Fe-4*d*(I) interlayer relaxation for the FM case, it is also important to try to understand Fe magnetic order on those 4*d* hexagonal substrates. Using first-principles collinear calculations, we demonstrate that a hexagonal Fe ML can assume very different magnetic phases on a triangular lattice provided by hcp (0001) and fcc (111) surfaces of 4*d*- and 5*d*-transition metals. Here we show our obtained collinear results of Fe monolayer on Pd(111), Rh(111) and Tc(0001) and compare them to other theoretical and experimental studies were done on Fe monolayer on Ru(0001) [135, 57, 139, 136, 140], Ir(111) [136, 27], Pt(111) [137], Re(0001) and Os(0001) [57].

To calculate the magnetic ground state, we followed the procedure as we did for 3*d*-monolayers on Rh(111) in last chapter (sec. 4.3.2). In figure 5.3, we show the total-energy difference between the FM and the row-wise AFM (RW-AFM) configuration, considering hcp and fcc stacking of the monolayer. Only for substrates at the end of the TM-series, Pd and Pt, the Fe monolayer prefers fcc stacking. On all other substrates Fe prefers an hcp stacking. Only on Rh and Ir the energy difference between fcc and hcp stacking is sufficiently small (9.0 and 7.6 meV/Fe-atom, respectively) to suggest the experimental observation of both types after film growth at room temperature [27, 28]. To see the importance of relaxing both, Fe monolayer and the substrate interface layer, we compared our Fe/Tc(0001) magnetic order with what ref. [57] calculated by relaxing only the Fe monolayer. In our calculations we got a RW-AFM ground state with -114 meV/Fe atom, while in ref. [57] the same ground state but with -82 meV/Fe atom was obtained. This means that there is about 30 meV/Fe atom difference, which is very large if we have smaller energies (as we see in Rh, Ir cases in Fig. 5.3), where we are in the energy range of about 30 meV/Fe atom. This will be discussed more in details in next section.

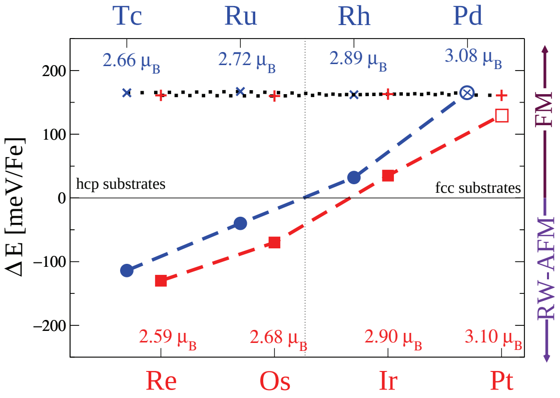

Figure 5.3: Total-energy difference between the FM ($\Delta E > 0$) and RW-AFM ($\Delta E < 0$) configuration for Fe MLs on hcp (0001) and fcc(111) surfaces of $4d$- and $5d$-TMs. Closed and open symbols indicate a favorable hcp or fcc stacking of the Fe ML, respectively. The magnetic moment of the Fe atoms, m_{Fe}, is given. $\Delta E_{\mathrm{AFM-FM}}$ is nearly constant for an unsupported hexagonal Fe ML (UML) with the corresponding in-plane lattice constants (dashed line). Results of Fe on Ru, Re, Os are taken from ref. [57], Fe/Ir(111) from ref. [27] and Fe/Pt(111) from ref. [141]

Our conclusion from Fig. 5.3 is that Fe on substrates from the center of the TM-series, Tc and Re, exhibits a clear antiferromagnetic behavior and the RW-AFM state has the lowest energy. Fe on substrates at the end of the TM-series is ferromagnetic. In between, we observe a gradual change from a strongly AFM to a strongly FM behavior as function of the electron filling of the substrate. It is argued that this change in the magnetic coupling results from the $3d-4d$ and $3d-5d$ hybridization between the Fe ML and the substrate, which is altered by the d-band filling [11, 14]. This argument is supported by the fact (i) that the role of the hybridization is also apparent from the monotonous variation of the Fe magnetic moments as one moves through the TM-series and (ii) the gradual change from FM to AFM coupling cannot be explained on the basis of the changing in-plane lattice constant as the comparison with unsupported MLs on the respective lattice constants shows a rather stable ferromagnetic value of about 160 meV/Fe-atom, c.f. Fig. 5.3.

From the results shown in figure 5.3, we can conclude that the nearest-neighbor exchange interaction, J_1, in the Fe ML changes continuously from antiferro- to ferromagnetic with the filling of the substrate's d-band. The antiferromagnetic exchange interaction is strong and important for Fe on most of these substrates except for Pd and Pt on which Fe is clearly ferromagnetic. The antiferromagnetic interaction on a triangular lattice leads to the frustration of magnetic interactions and is the origin of complex magnetic states. Fe on Re or Tc exhibits strong antiferromagnetic interactions as shown by the large energy gain when assuming a RW-AFM state and the true ground state could be a 120°-Néel state. Due to the small energy difference between the FM and RW-AFM order for Fe on Os, Ru, Rh and Ir many magnetic states have to be considered as possible ground states. Since Fe MLs were studied on Ru(0001)[57], we focus our study on Rh(111) as model systems of complex magnetism on a triangular lattice [27, 28]. For completeness we will also analyze Fe monolayer on Tc(0001) substrate.

5.2 Results of Fe monolayer on different hexagonal substrates from non-collinear calculations:

We concluded in the previous section (5.1.2), that the nearest-neighbor exchange interaction, J_1, in the Fe ML changes continuously from antiferro- to ferromagnetic with filling of the substrate d-band. For an Fe ML on substrates such as Rh, Ru, Re or Ir, J_1 is small, as we will see in this section, and interactions beyond nearest-neighbors or higher-order spin interactions can be relevant.

We also Study the so-called multi-$\mathbf{Q}$ states, which are a superposition of symmetry equivalent spin spirals, that are degenerate in the Heisenberg model but can gain energy, e.g., due to the presence of biquadratic or four-spin interactions [31]. The theory behind that can be explained and understood by constructing a model Hamiltonian using the well known classical Heisenberg model of atomic spins on local lattices sites (eq. 3.22). In this section we will show the model Hamiltonian in case of triangular lattices, and then find out the relationship between single and multi-$\mathbf{Q}$ states in terms of the higher order terms of the biquadratic and 4-spin interactions. After wards we present our computational results for spin spirals of Fe monolayer on Rh(111) and Tc(0001), and then compare them to what have been done in case of Fe monolayer on different $4d$-transition metals hexagonal substrates.

5.2.1 Model Hamiltonian & Heisenberg model for 2D hexagonal lattices:

For an antiferromagnetic material, the spin structures are frustrated if they are put on a triangular lattice. In this case, the nearest neighbor spin interactions predict a 120° Néel ground state if one goes beyond that to see how the long range exchange interaction influences the magnetic ground state, and more complex structures (spin-spirals) can be found. The best way is to describe these systems in terms of exchange parameters using a model Hamiltonian such as the classical Heisenberg model (eq. 3.22), where the quantum

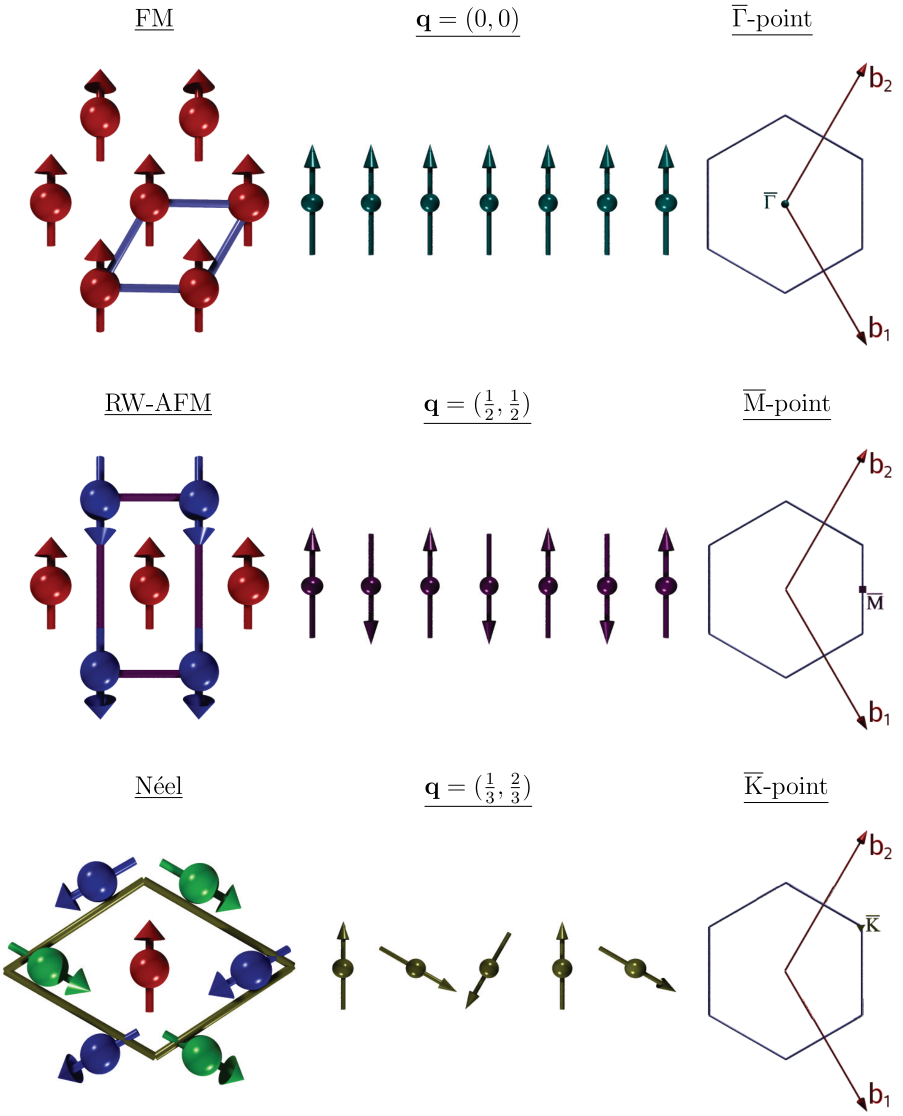

Figure 5.4: FM, RW-AFM and Néel spin configurations in real space and their spin spiral vector in Fourier (reciprocal) space.

nature of the spin is not taken into account [142, 143, 144, 145, 146, 147]. Flat spin spirals are the general solution of the classical Heisenberg model on a periodic lattice, where the exchange constants J_{ij} determine the strength and the type of coupling between local moments at sites i and j pointing along the unit vectors $\hat{\mathbf{M}}_i$ and $\hat{\mathbf{M}}_j$, respectively. Spin spirals are characterized by a wave vector $\mathbf{q}$ and the moment of an atom at site $\mathbf{R}_i$ is given by

$$\mathbf{M}_i(\mathbf{R}_i) = M\big(\cos(\mathbf{q}\cdot\mathbf{R}_i), \sin(\mathbf{q}\cdot\mathbf{R}_i), 0\big) \tag{5.2}$$

where M is the spin moment per atom and the unit vector $\hat{e} = (\cos(\mathbf{q}\cdot\mathbf{R}_i), \sin(\mathbf{q}\cdot\mathbf{R}_i), 0)$. By considering spin spirals along the high symmetry line of the hexagonal two-dimensional irreducible Brillouin zone (2D-IBZ), an important part of the magnetic phase space will be covered. Then, a model Hamiltonian can be expressed in terms of the exchange interaction parameters (see ref. [57, 38])

$$J(\mathbf{q}) = \sum_{\delta} J_{0\delta} e^{-i\mathbf{q}\cdot\mathbf{R}_\delta} \tag{5.3}$$

If the seventh nearest neighbor is taken into account, the total energy can be expressed for any $\mathbf{q}$ along $\overline{\Gamma}$-$\overline{\mathrm{K}}$-$\overline{\mathrm{M}}$ as:

$$\begin{aligned} E(q) = \quad -M^2(\quad & 2J_2 + 2J_6 \\ & +\cos(\pi q)[4J_1 + 4J_5] \\ & +\cos(2\pi q)[2J_1 + 4(J_3 + B_1 M^2) + 4J_7] \\ & +\cos(3\pi q)[4J_2 + 4J_5] \\ & +\cos(4\pi q)[2(J_3 + B_1 M^2) + 4J_4] \\ & +\cos(5\pi q)[4J_4 + 4J_7] \\ & +\cos(6\pi q)[2J_5 + 4J_6] \\ & +cos(7\pi q)[4J_7]) \end{aligned} \tag{5.4}$$

where $q \in$[0,1]. At high symmetry points along $\overline{\Gamma}$-$\overline{\mathrm{K}}$-$\overline{\mathrm{M}}$, we find well-known magnetic states such as the FM state at the $\overline{\Gamma}$-point, the RW-AFM state at the $\overline{\mathrm{M}}$-point, and the 120° Néel state at the $\overline{\mathrm{K}}$ point, see Fig. (5.4).

It can be shown that the model Hamiltonian along $\overline{\mathrm{M}}$-$\overline{\Gamma}$ differs from what we have in equation. (A-20), and can be written in the following form:

$$\begin{aligned} E(q) = \quad -M^2(\quad & 2J_1 + 2(J_3 + B_1 M^2) + 2J_5 \\ & +\cos(\pi q)[4J_1 + 4J_2 + 4J_4 + 4J_7] \\ & +\cos(2\pi q)[2J_2 + 4(J_3 + B_1 M^2) + 4J_4 + 2J_6] \\ & +\cos(3\pi q)[4J_4 + 4J_5 + 4J_7] \\ & +\cos(4\pi q)[2J_6 + 4J_7]) \end{aligned} \tag{5.5}$$

For the single-**Q** we can obtain values for the nearest-neighbor biquadratic interaction, B_1, and four-spin interaction, K_1. The first order contributions of the biquadratic terms, B_1, to the FM, RW-AFM and 3**Q** states are[38]

$$\begin{aligned} E_{\text{biquardr,FM}} &= -6B_1M^4 \\ E_{\text{biquardr,RW-AFM}} &= -6B_1M^4 \\ E_{\text{biquardr,Néel}} &= -\frac{3}{2}B_1M^4 \\ E_{\text{biquardr,3Q}} &= -\frac{2}{3}B_1M^4 \end{aligned} \tag{5.6}$$

while the contributions if the 4-spin interaction exchange constants, K_1, are

$$\begin{aligned} E_{4-\text{spin,1Q}} &= -12K_1M^4 \\ E_{4-\text{spin,3Q}} &= -\frac{4}{3}K_1M^4 \end{aligned} \tag{5.7}$$

The degeneracy of single- and multi-**Q** states within the Heisenberg model is lifted by the higher-order interactions, by calculating the energy differences between suitable single-**Q** and multi-**Q** states. One set of degenerate states are spin spirals at the $\overline{\text{M}}$-points of the 2D-BZ and the 3**Q**-state constructed from the three independent $\overline{\text{M}}$-points [31], then the difference between the single-$\mathbf{Q}_{\overline{\text{M}}}$ and the 3**Q** is a constant as shown in eq. (5.8).

$$E_{3Q} - E_{\text{RW-AFM}} = (16/3)\{2K_1 + B_1\} \tag{5.8}$$

for the difference between the 3**Q** and the single-$\mathbf{Q}_{\overline{\text{M}}}$, which are degenerate in the Heisenberg model.

To calculate B_1 and K_1 we need a second equation, which can be found as following: A superposition of two ±**Q**-points at the high symmetry line, which is degenerate with each of them, called the double-**Q**-state. There are two possible choices, the first one is to take the $\mathbf{Q}_{3\overline{\Gamma\text{K}}/4}$-point, which represents a rotating spirals with $\pm\frac{\pi}{2}$ along $\overline{\Gamma}$-$\overline{\text{K}}$ direction. A superposition of $\pm\mathbf{Q}_{3\overline{\Gamma\text{K}}/4}$ will lead to an double-RW-AFM structure in real space, called *uudd*($3\overline{\Gamma\text{K}}/4$)-state as shown in figure 5.5. A second choice is to take the $\mathbf{Q}_{\overline{\text{M}\Gamma}/2}$-point, which represents also rotating spirals with $\pm\frac{\pi}{2}$ but this time along $\overline{\text{M}}$-$\overline{\Gamma}$ direction. A superposition of $\pm\mathbf{Q}_{\overline{\text{M}\Gamma}/2}$ will lead to an double-RW-AFM structure in real space along $[11\overline{2}]$, called *uudd*($\overline{\text{M}\Gamma}/2$)-state (see fig. 5.5).

This means if we plug $\mathbf{Q}_{3\overline{\Gamma\text{K}}/4} = \frac{3}{4} \times \frac{2}{3}$ in eq. (A-20) we will have

$$E = -M^2(-2J_1 + 2J_2 - 2J_3 - 4J_4) + 2B_1M^4 - 12K_1M^4 \tag{5.9}$$

for the single-$\mathbf{Q}_{3\overline{\Gamma\text{K}}/4}$ and

$$E = -M^2(+2J_1 - 2J_2 - 2J_3 - 4J_4) + 2B_1M^4 - 12K_1M^4 \tag{5.10}$$

if we use $\mathbf{Q}_{\overline{\mathrm{M}\Gamma}/2} = \frac{1}{2}$ in eq. (A-21) for the single-$\mathbf{Q}_{\overline{\mathrm{M}\Gamma}/2}$.

If we use the double-$\mathbf{Q}$ biquadratic and 4-spin terms derived in Ref. [38]

$$E_{\text{biquardr,2Q}} \quad = \quad -2B_1M^4 \quad \text{and} \quad E_{4-\text{spin,2Q}} = -4K_1M^4 \tag{5.11}$$

and then plug them in the *uudd*–model Hamiltonian up to the fourth nearest neighbor, we get

$$E = -M^2(-2J_1 + 2J_2 - 2J_3 - 4J_4) - 2B_1M^4 - 4K_1M^4 \tag{5.12}$$

for the *uudd*$(3\overline{\Gamma K}/4)$-state and

$$E = -M^2(+2J_1 - 2J_2 - 2J_3 - 4J_4) - 2B_1M^4 - 4K_1M^4 \tag{5.13}$$

for the *uudd*$(\overline{\mathrm{M}\Gamma}/2)$-state.

A a result (5.12)-(5.9)=(5.13)-(5.10), which means that we will have the same energy difference between the single- and double-$\mathbf{Q}$-state in both Γ-K-M and Γ-M directions, i. e

$$E_{uudd} - E_{3\overline{\Gamma\mathrm{K}}/4} \quad = \quad E_{uudd} - E_{\overline{\mathrm{M}\Gamma}/2} = 4\{2K_1 - B_1\} \tag{5.14}$$

for the difference between the *uudd* $\left(3\overline{\Gamma\mathrm{K}}/4\right)$ $\left(uudd\left(\overline{\mathrm{M}\Gamma}/2\right)\right)$ and the single-$\mathbf{Q}_{3\overline{\Gamma\mathrm{K}}/4}$ $(\mathbf{Q}_{\overline{\mathrm{M}\Gamma}/2})$ along $\overline{\Gamma}$-$\overline{\mathrm{K}}$-$\overline{\mathrm{M}}$ ($\overline{\mathrm{M}}$-$\overline{\Gamma}$) direction. By that, we are able to calculate B_1 and K_1 from equations (5.14) and (5.8).

Using equations (A-20) and (A-21), different cuts through the zero temperature magnetic phase diagrams can be calculated analytically. The magnetic phase diagram, shown in figure 5.6, are calculated only for the first three exchange interaction terms J_1, J_2 and J_3. I. e., the exchange interactions taken into account are up to the third nearest neighbor. From these phase diagrams, it can be seen that not only collinear but mainly non-collinear magnetic structures exist on 2D hexagonal lattices.

If we calculate the phase diagram in arbitrary units of J_1 (5.6(a)), the Néel ground state is expected for any positive value of J_2 if J_1 is negative. A spin spiral structure is predicted for large positive J_1 if J_2 is smaller than $-J_1$. On the other hand, if the third nearest neighbor interaction term J_3 is included, the possibility of predicting more complex structures increases (c. f. 5.6(b) and (c)). For example, the possibility to have non-collinear magnetic structures is very large if both J_2 and J_3 values are negative and larger than $\approx \frac{|J_1|}{2}$.

In practice, these phase diagrams can be used as a starting point to predict the magnetic order on triangular lattices by tuning the substrate or the overlayer. A very simple, and computationally less expensive approach is to employ the virtual crystal approximation (VCA) [148], in which one studies a crystal with the primitive periodicity, but composed

3-**Q** state: $3Q$ combination

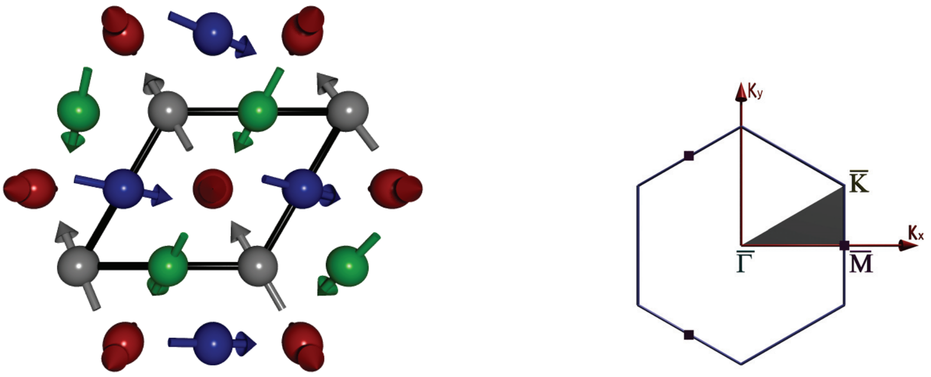

uudd$\left(\frac{3\overline{\Gamma}\,\overline{\mathrm{K}}}{4}\right)$: $2Q$ combination

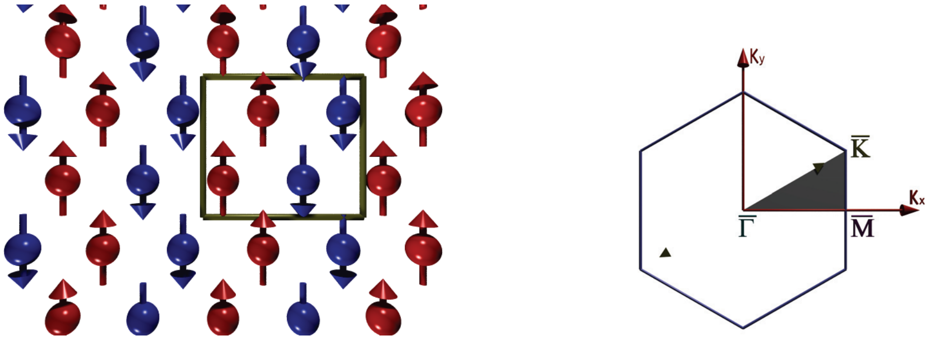

uudd$\left(\frac{\overline{\Gamma}\,\overline{\mathrm{M}}}{2}\right)$: $2Q$ combination

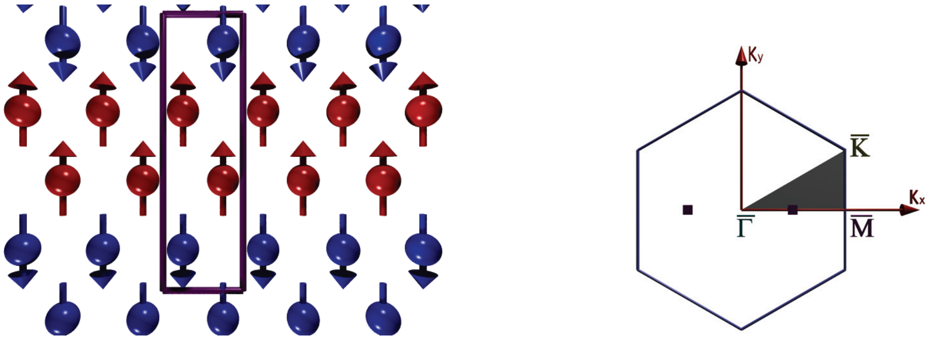

Figure 5.5: Double- and multi-**Q** states spin structures in real space (left) and reciprocal space (right).

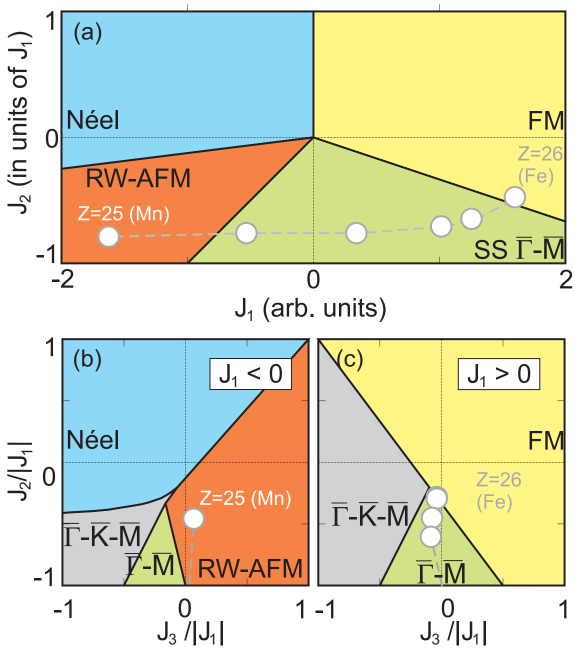

Figure 5.6: Phase diagrams of the classical Heisenberg model for a 2D hexagonal lattice for states on the high symmetry lines. (a) J_1-J_2 plane for $J_3 = 0$. J_2-J_3 plane for (b) $J_1 > 0$ and (c) $J_1 < 0$. White circles are the exchange interaction parameters obtained from fitting the spin spiral curve using eq. (A-20) of free standing Mn/Fe monolayer within the VCA. This plot was calculated by B. Hardrat at University of Hamburg.

of fictitious "virtual" atoms that interpolate between the nuclear number Z of the atoms in the parent compounds, which is possible if Z differs by ±1. This technique is widely used in band-structure calculations. By using this approximation, one can calculate the spin spiral curve for free standing monolayer of Mn, and then do a fractional increase of Mn atomic number to reach Fe atomic number. This means that the energy spin spiral curve is calculated as if we have an $\mathrm{Fe}_{1_x}\mathrm{Mn}_x$ alloy, with x Mn concentration, we can predict all possible magnetic ground states if we tune Mn concentration in the alloy. I. e. we increase the 3d-band filling. This can also be applied if we have a pure magnetic monolayer supported by a tunable substrate, like alloys of different substrates of different atomic numbers like 4d- or 5d-transition metals. From the energy spin spiral curve of free standing Mn/Fe layer using the VCA, the exchange interaction parameters, J_1, J_2 and J_3, are calculated by fitting the energy dispersion curve to equation A-20. Using the values of J, we see that pure Mn ML will have a RW-AFM ground state, while Fe ML prefers FM ground state. We can see that Mn ML might have complex non-collinear magnetic structures the Mn $3d$-band filling is increased. This supports our idea that the exchange interaction parameters can be controlled by tuning the substrate, which might lead to unexpected complex magnetic structures.

5.2.2 Results of Fe monolayer on Rh(111):

In this section, the search for the magnetic ground state of Fe on Rh and Tc will be shown by performing non-collinear spin-spiral calculations along the high symmetry line, $\overline{\Gamma}$-$\overline{\mathrm{K}}$-$\overline{\mathrm{M}}$-$\overline{\Gamma}$, in the hexagonal BZ. The non-collinear magnetic states have been studied employing an asymmetric film consisting of six substrate layers and an Fe monolayer on one side of the film at the distance optimized for the collinear (FM or AFM) state of lowest energy. The spin spirals have been calculated exploiting the generalized Bloch theorem [83]. We have used about 120 basis functions per atom for all calculations and at least 1024 $\mathbf{k}_{\|}$ points in the 2D-BZ for the spin-spiral calculations, 48 $\mathbf{k}_{\|}$ points in one quarter of the 2D-BZ for the *uudd* configurations and 32 $\mathbf{k}_{\|}$ points in the 2D-BZ for the 3**Q**-state requiring a surface unit-cell comprising 4 atoms. All other numerical parameters were kept to be the same as for the collinear calculations in sec. (4.3.1).

The total energy relative to the FM spin configuration of Fe monolayer on Rh(111), is shown in fig. 5.7 as a function of the spin-spiral **q**-vector, using GGA and LDA exchange correlation potentials, along the high symmetry line $\overline{\Gamma}$-$\overline{\mathrm{K}}$-$\overline{\mathrm{M}}$-$\overline{\Gamma}$, and for hcp or fcc Fe-Rh(I) stacking. We see that both stacking sequences share the same global minimum energy. The fcc Fe-Rh(I) is lower than the hcp stacking minimum energy by ~ -5 meV/Fe atom. But the Fe prefers hcp stacking by -9 meV/Fe atom (see subsec. 5.1.2) from the independently FM relaxed solution of each stacking, this means that the real spin spiral curve of the hcp Fe-Rh(I) stacking is lower in energy by -9meV, i. e. the hcp is lower than the fcc stacking global minimum energy by -4 meV/Fe atom, provided that the difference between fcc and hcp Fe-Rh(I) optimized d_{12} was 0.01Å. We checked that, and found the our analogy is true, the hcp at the minimum **q**-point is always lower than the fcc stacking total energy by -4 meV/Fe atom. Because of that, we always use the Fe-Rh(I) hcp stacking results. On the other hand, we compare GGA and LDA results, and we see that both confirm the same result, where Fe monolayer might have a possible spin spiral ground state along $\overline{\Gamma}$-$\overline{\mathrm{K}}$, with -5 (-10) meV/Fe atom in case of GGA (LDA).

A simple approach to estimate the J's, is to exclude the higher order terms in equation A-20, and calculate J_1, J_2 and J_3 from the high symmetry points total energies, $\overline{\Gamma}$, $\overline{\mathrm{M}}$ and $\overline{\mathrm{K}}$, where they are presented in terms of J_1, J_2 and J_3 from equation A-20 as following:

$$\begin{aligned} E_{\overline{\Gamma}} &= -\mathrm{M}^2(6\mathrm{J}_1 + 6\mathrm{J}_2 + 6\mathrm{J}_3) \\ E_{\overline{\mathrm{M}}} &= -\mathrm{M}^2(-2\mathrm{J}_1 - 2\mathrm{J}_2 + 6\mathrm{J}_3) \\ E_{\overline{\mathrm{K}}} &= -\mathrm{M}^2(-3\mathrm{J}_1 + 6\mathrm{J}_2 - 3\mathrm{J}_3) \end{aligned} \tag{5.15}$$

As a simple approximation, if the variation of Fe magnetic moments is considerably small at the high symmetry points, , we can assume an arbitrary value of M=1. We have three

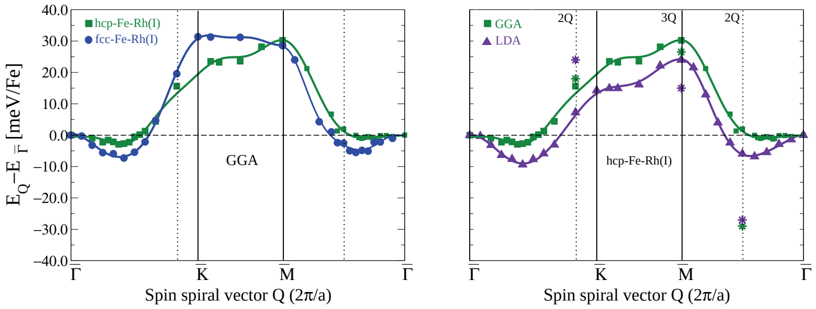

Figure 5.7: Total energy of spin spirals for 1 ML Fe/Rh(111). Solid blue circles (green squares) are the fcc (hcp) Fe-Rh(I) stacking GGA results (left). Solid indigo triangles are the LDA results with hcp-Fe-Rh(I) stacking (right). The green (indigo) stars are the GGA (LDA) double- and multi-**Q** total energies.

equations with three variables. By solving equation (5.15) we get values of J_1, J_2 and J_3 equal to $+5.97(+4.18)$, -2.22 (-1.56), and -3.75 (-2.63) meV/Fe from GGA (LDA) results. If we use these values and insert them in the phase diagram (Fig. 5.6), we find out that Fe has indeed a non-collinear spin spiral ground state along $\overline{\Gamma}$-$\overline{\mathrm{K}}$-$\overline{\mathrm{M}}$-$\overline{\Gamma}$, using both GGA and LDA exchange correlation potentials. This agrees well with what we see in our spin spirals results. In addition to their effect on calculating J_3 value accurately, we know from eq. A-20, that including the higher order terms B_1 and K_1, in Heisenberg model, requires us to go beyond the third nearest neighbor and calculate at least J_4 for qualitative results. In this case to calculate the fourth nearest neighbor we need to it to the whole curve (Fig. 5.7) while to determine B_1 and K_1 equations (5.8 and 5.14) can be used. Calculating the double- and multi-**Q** states will include the higher order interactions in our calculations, and helps to get more accurate J values, and better prediction of the true ground state.

The 3Q state can be constructed in real space by a superposition of three $\overline{\mathrm{M}}$ points on the hexagonal Brillouin zone (see Fig.5.5). The double-Q structure, along $\overline{\Gamma}$-$\overline{\mathrm{K}}$-$\overline{\mathrm{M}}$, is a collinear magnetic structure in real space which can be constructed by a superposition of two spiral **q**-points at $\mathbf{Q}_{3\overline{\Gamma\mathrm{K}}/4}$, i.e. *uudd* $\left(3\overline{\Gamma\mathrm{K}}/4\right)$ in real space (see Fig. 5.5). Because we calculated the spin spirals using at ferromagnetically relaxed positions, we performed real space (collinear) calculations to determine the total energies of the multi-**Q** (double-**Q**) states with the same relaxed atomic positions. By that we got the value illustrated by stars in figure 5.7 using LDA and GGA exchange correlation potentials. If we look at the calculated double-**Q** value, we see that it has higher (lower) energy than the corresponded **q**-point by about $+3$ (-30) meV/Fe atom for the $\mathbf{Q}_{3\overline{\Gamma\mathrm{K}}/4}$ and $\mathbf{Q}_{\overline{\mathrm{M}\Gamma}/2}$ points, respectively, which is surprising since they are expected to gain the same energy due to the including of the higher order terms. The 3**Q** results show -2.5 (-8) meV/Fe atom energy gain below the $\overline{\mathrm{M}}$, the RW-AFM phase, value using GGA (LDA). Then we calculated B_1 and K_1 values using equations (5.8 and 5.14) for the $\mathbf{Q}_{3\overline{\Gamma\mathrm{K}}/4}$ and got $B_1 = -0.6$ and K_1 =0.0 meV/Fe atom, we then added these values to the model Hamiltonian constructed along $\overline{\Gamma}$-$\overline{\mathrm{K}}$-$\overline{\mathrm{M}}$, and used it to fit our calculated energy dispersion curve to calculate the exchange interaction parameters, which are shown in table 5.2.

Table 5.2: GGA and LDA results of Heisenberg exchange constants for the hcp Fe ML on Rh(111) substrate obtained by fitting the total-energy dispersion along $\overline{\Gamma}$-$\overline{\mathrm{K}}$-$\overline{\mathrm{M}}$ and the higher order terms B_1 and K_1

(meV)	J_1	J_2	J_3	J_4	B_1	K_1
GGA	3.8	-0.6	-1.6	0.3	-0.6	0.0
LDA	3.9	-0.7	-1.1	0.4	-1.3	0.5

We see that GGA and LDA values of J_1, J_2 and J_3 are very similar, but different from what we got when we exclude the higher order interaction terms, using Eq. (5.15). These results show how important is to include the higher order terms in the model Hamiltonian to get accurate values of the exchange interaction parameters. If we use the values of $J_3/|J_1|$ and $J_2/|J_1|$ from the shown results in table 5.2, we find that Fe has non-collinear spin spiral along $\overline{\Gamma}$-$\overline{\mathrm{K}}$-$\overline{\mathrm{M}}$ on Rh(111) substrate, but still very close to to FM phase transition, referring to the calculated phase diagrams in figure 5.6. This is consistent with the minimum -5 meV/Fe atom total energy difference below the $\overline{\Gamma}$ point, i.e. the FM solution. From the calculated higher order interactions parameters, we notice that the biquadratic interaction term B_1 is in the same order as the next nearest neighbor term J_2, where as the 4-spin interaction term K_1 is zero. In this case we can interpret our results keeping in mind that if the Fe atoms nearest neighbor interactions are relatively weak compared to next nearest neighbor interactions, the higher order terms are very important and cannot be ignored due to their highly possible contribution of stabilizing non-collinear ground state.

Because of the small ground state total energy difference, the above interpretation is not a final answer since we are not sure if this small energy difference yields the global minimum or not, especially since the difference k-points sampling between the spin spiral, collinear (for double-$\mathbf{Q}$) and the real space (for 3$\mathbf{Q}$) calculations will produce about 5 meV/Fe atom numerical error as it was checked for free-standing Fe monolayer. Because of that, we calculated the total energy of the double-$\mathbf{Q}$ state along the line $\overline{\mathrm{M}}$-$\overline{\Gamma}$, which is constructed by a superposition of two $\mathbf{Q}$ points at $\mathbf{Q}_{\overline{\mathrm{M}\Gamma}/2}$, which represents a collinear magnetic structure in real space called *uudd* $\left(\overline{\mathrm{M}\Gamma}/2\right)$ state (see Fig. 5.5). The GGA (LDA) results show, surprisingly, that the *uudd* $\left(\overline{\mathrm{M}}\,\overline{\Gamma}/4\right)$ gained about -32 (-27) meV/Fe atom below the $\mathbf{Q}_{\overline{\mathrm{M}}/2}$ point, and became a global minimum by -30 (-21) meV/Fe atom relative to FM solution. These results were not expected because *uudd* $\left(\overline{\mathrm{M}\Gamma}/2\right)$ and *uudd* $\left(3\overline{\Gamma\mathrm{K}}/4\right)$ are degenerate according to Heisenberg picture explained in section (3.2), and supposed to provide the same B_1 and K_1 values.

Trying to understand the unexpected obtained results for *uudd* $\left(\overline{\mathrm{M}\Gamma}/2\right)$, we plotted the Fe, the interface layer Rh(I), and the subsurface rhodium layer Rh(I-1) GGA and LDA

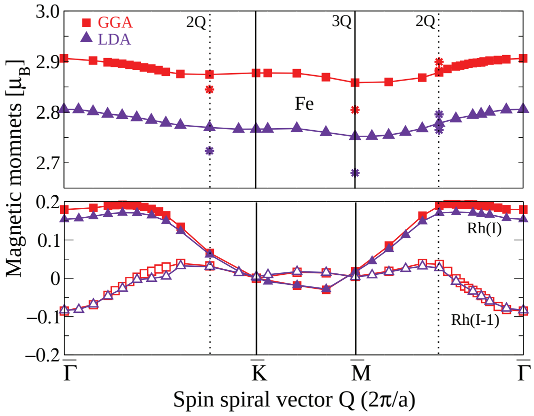

Figure 5.8: Fe, Rh(I) and Rh(I-1) spin moments are presented by magenta circles (violet squares) symbols from GGA (LDA) spin spiral calculations. The Rh subsurface moments are indicated by open symbols and Rh(I) by solid ones.

magnetic moments for each spin spiral point **q**, as shown in figure 5.8. First we see that LDA predicts smaller magnetic moments than GGA for Fe by about constant value ($0.1\mu_B$) at each **q**-point. Also for Rh(I) atoms, LDA predicted smaller Rh induced moments than GGA, especially for spirals between the $\mathbf{Q}_{\overline{\mathrm{M}}/2}$, or $\mathbf{Q}_{\overline{3\Gamma\mathrm{K}}/4}$, and $\overline{\Gamma}$, with smaller difference for the $\mathbf{Q}_{\overline{\mathrm{M}}/2}$ compared to $\mathbf{Q}_{\overline{3\Gamma\mathrm{K}}/4}$ moments. No change in the Rh subsurface induced moments using GGA or LDA is observed.

The very interesting result, which may explain the magnetic ground state of *uudd* $\left(\overline{\mathrm{M}\Gamma}/2\right)$ Fe on Rh(111), can be seen in the rhodium induced magnetic moments at the interface and subsurface. We see large polarization of the Rh(I) at $\mathbf{Q}_{\overline{\mathrm{M}}/2}$ while for $\mathbf{Q}_{\overline{3\Gamma\mathrm{K}}/4}$, smaller polarized Rh induced moments were found, although the Fe moments are similar for both **q**-points. To have full picture about Rh induced moments, we need also to know the induced moments of the double- and multi-**Q** states, which are missing figure 5.8 because Rh(I) has two values of induced moments, for the *uudd* $\left(\overline{\mathrm{M}\Gamma}/2\right)$ configuration, as can be seen in table 5.3.

First we explain the reason of having different induced moments in the Rh(I) layer atoms for *uudd* $\left(\overline{\mathrm{M}\Gamma}/2\right)$, while they are equally induced for *uudd* $\left(3\overline{\Gamma\mathrm{K}}/4\right)$: If we have a side view on both configurations, as illustrated in figure 5.9, we see that each Rh(I) atom is below three Fe atoms and affected by a net Fe magnetization direction of $\pm 1\mathbf{M}_{Fe}$ in the case of *uudd* $\left(3\overline{\Gamma\mathrm{K}}/4\right)$. This is not the case for the *uudd* $\left(\overline{\mathrm{M}\Gamma}/2\right)$ configuration, where Rh(I) atoms are affected once by ±1 net Fe magnetization and another by $\pm 3\mathbf{M}_{Fe}$.

If we now look to the magnetic polarization at Rh(I) and Rh(I-1), both GGA and

Table 5.3: LDA and GGA Fe and Rh(111) induced moments at the interface and the subsurface rhodium layers, Rh(I) and Rh(I-1), for the double- and multi-Q states in units of μ_B using.

	GGA		**LDA**	
	Rh(I)	Rh(I-1)	Rh(I)	Rh(I-1)
uudd $\left(3\overline{\Gamma\mathrm{K}}/4\right)$:	0.11	0.04	0.11	0.04
uudd $\left(\overline{\mathrm{M}\Gamma}/2\right)$:	0.32,0.09	0.04	0.27,0.08	0.03
3**Q**:	0.11	0.02	0.10	0.02

LDA predict again similar double- and multi-**Q** rhodium induced moments for the 3**Q** and *uudd* $\left(3\overline{\Gamma\mathrm{K}}/4\right)$. If we take GGA results of Rh induced moments, we see that the double-**Q** *uudd* $\left(3\overline{\Gamma\mathrm{K}}/4\right)$, has the same polarization between Rh(I) and Rh(I-1) induced moments as the $\mathbf{Q}_{3\overline{\Gamma\mathrm{K}}/4}$-point ($\approx$0.05 μ_B), where the 3**Q** has larger induced moments ($\approx$0.08 μ_B) than the $\mathbf{Q}_{\overline{\mathrm{M}}/2}$ ($\approx$0.02 μ_B) state in the substrate Rh(I) and Rh(I-1) layers. The largest polarization for Rh(I) and Rh(I-1) occurs for the *uudd* $\left(\overline{\mathrm{M}\Gamma}/2\right)$ state, where it has also larger polarization ($\approx$0.32 μ_B) than the $\mathbf{Q}_{\overline{\mathrm{M}}/2}$-point ($\approx$0.16 μ_B), even larger than the polarization at $\overline{\Gamma}$-point ($\approx$0.25 μ_B). From these results, we can now explain why the equality between the degenerate double-**Q** states in equation (5.14) is broken and we cannot use this equations to calculate the higher order terms B_1 and K_1, to use them to fit the energy dispersion curve along $\overline{\mathrm{M}}$-,$\overline{\Gamma}$, using equation (A-21). This means that, if we use equations (5.8 and 5.14) to calculate B_1, we will have B_1 values which, if we use in equation (A-21) to fit the energy dispersion curve, will produce inconsistent J values which cannot be used to predict the true ground state.

.

The reason of this inconsistency is the following: When we used *uudd* $\left(3\overline{\Gamma\mathrm{K}}/4\right)$ results to calculate B_1 and then use it in equation (A-20), we got consistent J, B_1 and K_1 values due to the homogeneous induced moments in the Rh(I), which agrees with what was mentioned in ref.[31], and that the model Hamiltonian for higher order terms is only applicable for constant magnetic moments. This means that we cannot use this model for for highly polarized substrates like Rh(111) substrate to calculate higher order interactions constants, because the substrate moments are not equally induced in all directions, which leads to a failure in calculating the correct exchange interaction parameters and then to wrong prediction of the system ground state from the magnetic phase diagrams. Instead, our results suggest that a term proportional to $\mathbf{M}^2$ or $\mathbf{M}^4$ is missing in the functional, similar to what was proposed in Ref.[149].

To see if we can explain Fe magnetic ground state on Rh(111) using the LDOS, we compare the LDOS of RW-ARM, FM and the *uudd* $\left(\overline{\mathrm{M}\Gamma}/2\right)$ configurations, shown in figure 5.10. If we look at Fe LDOS, we notice that the RW-AFM and the *uudd* $\left(\overline{\mathrm{M}\Gamma}/2\right)$ majority spins are very similar with the FM LDOS majority shifted toward Fermi level (E_F). Most important is the fact that smallest LDOS is obtained for *uudd* $\left(\overline{\mathrm{M}\Gamma}/2\right)$ minority spin states, while FM and the RW-AFM minority spin states remain of similar height at Fermi energy, with sharper FM minority band. The Rh(I) LDOS have opposite trend: The

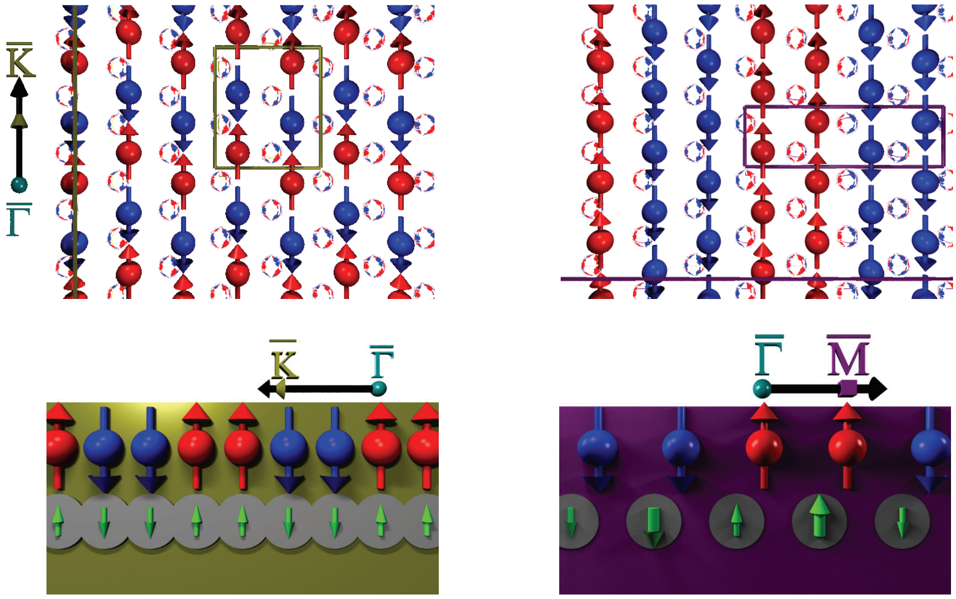

Figure 5.9: Illustration of the reason why do does *uudd* $\left(\overline{\mathrm{M}\Gamma}/2\right)$ have different while *uudd* $\left(3\overline{\Gamma\mathrm{K}}/4\right)$ has equal induced moments in Rh(I) layer of Rh(111) surface.

uudd $\left(\overline{\mathrm{M}\Gamma}/2\right)$ minority band is the largest at E_F, and remains of similar value for the FM and RW-AFM LDOS. The Rh(I) majority bands at E_F, are smallest for the *uudd* $\left(\overline{\mathrm{M}\Gamma}/2\right)$, and largest for the FM LDOS. These results confirms our explanation of the c(2×2)-AFM Fe ground state on Rh(001), where the LDOS minority bands for the c(2×2)-AFM are smaller than the minority states of the FM solution (see sec. 4.2.2).

Up to now, we have no access to experimental studies to verify our calculated results and predictions for Fe monolayer on Rh(111) hexagonal substrates. For Fe/Rh(111) we can compare our prediction of Fe monolayer magnetic ground state on Rh(111), by referring to the experimental verification of Fe complex magnetism on Ir(111) surface[27, 28]. This comparison is very helpful due to the fact that Ir is below Rh in the periodic table, i. e. both have the same *d*-band filling. This means, Ir and Rh are expected to interact in similar way from electronic structure point of view, keeping in mind that Ir has larger spin orbit coupling parameter which magnifies the magnetic anisotropy energy and the Dzyaloshinskii-Moriya interaction and then stabilizes long range magnetic order at non-zero temperatures. Nevertheless, the study of Fe/Ir(111) suggests that multiple-**Q** states can be constructed to reproduce the observed magnetic unit cell, and they might be quit similar to (7:8) mosaic structure, a collinear magnetic structure[27], with 15 atoms in the unit cell. The 4-atomic *uudd* $\left(\overline{\mathrm{M}\Gamma}/2\right)$ unit cell, as we did for Fe/Rh(111), was also calculated and an energy close to the 15-atoms ground state structure was obtained[150]. Since

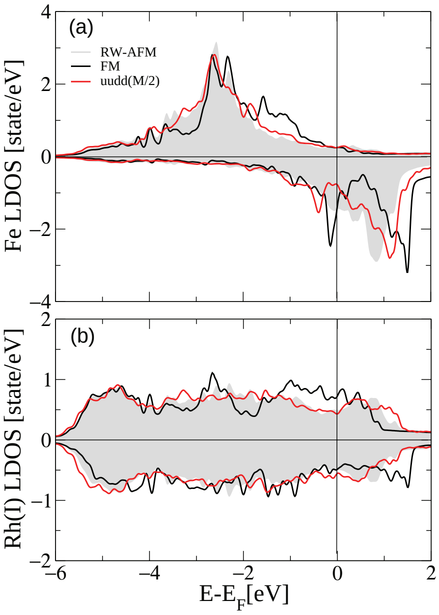

Figure 5.10: LDOS of the RW-AFM (gray shaded), FM (black line) and *uudd* $\left(\overline{\mathrm{M}\Gamma}/2\right)$ (red line) state of (a) Fe monolayer and (b) Rh(I) layer.

the observed magnetic unit cell seems to be large and contains more than 4-atoms per unit cell we constructed by superposition of two **Q** spiral points (see Fig. 5.5). Simple trial is, if we make a super position of another two spiral points at $\mathbf{Q}_{\overline{\mathrm{M}}/2}$, we will have 16-atoms per unit cell, each group of four atoms have the same atomic spin and rotate by $\frac{\pi}{2}$ with respect to each other as illustrated in figure 5.11, with coplanar vortex-like magnetic structure. Using this large unit cell, we performed total energy calculations for Fe UML, and found that the vortex-like structures has +66 meV/Fe atom energy above the FM solution, where the Fe UML 4-atoms *uudd* $\left(\overline{\mathrm{M}\Gamma}/2\right)$ configuration has −7 meV/Fe atom energy less than the the FM solution. This two dimensional possibility is not the only one, but there are another two complex three dimensional possible spin structures can be constructed from the same vortex-like **Q**-points. This was tested for only one Fe UML due to the large computational effort, which makes it very difficult to perform calculations of realistic systems. On the other hand, there are many possible AFM configurations that might be constructed in real space on hexagonal lattices along $[11\overline{2}]$, but not from a linear combination of two **Q**-points on the high symmetry line as the *uudd*-states we studied. We checked one possibility by calculating the total energy of an *uuud*-state along $[11\overline{2}]$ and found that it has lower energy than the collinear FM state of Fe/Rh(111) by −17 meV/Fe atom, but remains higher than the *uudd* $\left(\overline{\mathrm{M}\Gamma}/2\right)$ ground state we found by +13 meV/Fe

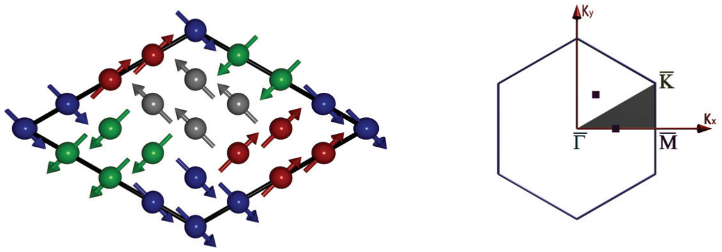

Figure 5.11: Vortex-like structure, with sixteen atoms per unit cell, each four atoms have the same spin rotating by $\frac{\pi}{2}$ with respect to each other(left). The two spin spiral **Q**-points used to construct such a coplanar vortex-like structure (right).

atom.

5.2.3 Results for the Fe monolayer on Tc(0001) substrate:

Employing the same procedure as for Fe/Rh(111), we performed also non-collinear calculations to calculate total energies in terms of spiral vectors for Fe monolayer on technetium (0001) surface, Tc(0001). The aim of that is to have a complete picture about Fe magnetism on different hexagonal substrates, especially after the theoretical study performed to study Fe ground state on Ru(0001) and Re(0001) from non-collinear DFT calculations [57]. Also, the ground state of Fe monolayer on Ir(111) was experimentally investigated and modeled by theoretical non-collinear DFT calculations [27, 28].

We used the experimental Tc lattice constants to calculate the spin spirals using the collinear ground state, RW-AFM, relaxations (Tab. 5.1). All numerical parameters were the same as for Fe/Rh(111). Results of total energies relative to the FM solution, using GGA are shown in figure 5.12(a). The moments of Fe, Tc(I) and Tc(I-1) are also presented in figure 5.12 (b). In addition we performed collinear calculations at the two double-**Q**, *uudd* $\left(\overline{\mathrm{M}\Gamma}/2\right)$ and *uudd* $\left(3\overline{\Gamma\mathrm{K}}/4\right)$ states, to test the validity of equations (5.8 and 5.14), since the equality of the difference between the single- and double-**Q** total energies was broken for Rh(111) case.

We see, from figure 5.12(a), that also here, we have different energy differences between the two double-**Q**s and their single-**Q**, even though these differences are rather small. These results indicate that the higher order interactions are very weak and cannot change the magnetic ground state from what is enforce by the nearest next nearest neighbor interactions. The global minimum energy is at $\overline{\mathrm{K}}$, which means that Fe has a Néel ground state on Tc(0001) with angles of 120° between adjacent spins, with −180 (−60) meV/Fe atom below the FM (RW-AFM) solution. The change of Fe ground state from a RW-AFM to a Néel structure, due to topological frustrations, highlights the importance of taking non-collinear magnetic structures into account. This can be seen from the RW-AFM

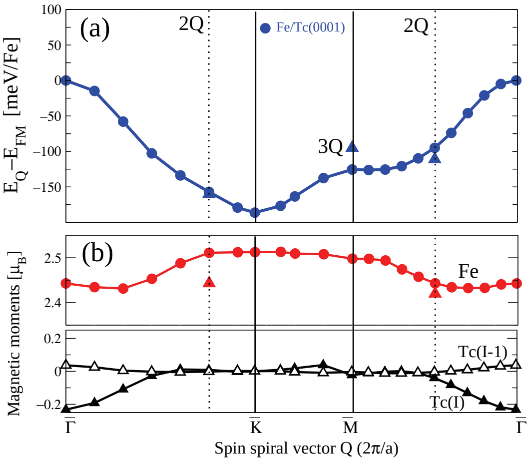

Figure 5.12: (a) Total energy of spin spirals for 1 ML Fe/Tc(0001) are presented by solid squares. (b) Fe magnetic moments and the Rh(I), Rh(I-1) induced moments. The double-**Q** state results are presented by solid triangles.

ground state predicted from collinear calculations including only next nearest neighbor interactions by the choice of two atoms per unit cell. We also can see that Tc surface layers were not strongly polarized, from the Tc(I) and Tc(I-1) induced magnetic moments shown in figure 5.12 (b).

On the other hand, if we look to the magnetic moments from the double-Q calculation, presented in table 5.4, the polarization between Tc(I) and Tc(I-1) is small as it is for the single-**Q** state. Interestingly, the Fe moments are strongly polarized for the *uudd* $\left(\overline{\mathrm{M}\Gamma}/2\right)$ double-**Q** state. We will discuss this result when we compare all Fe/4*d* results at the end of chapter

Table 5.4: GGA Fe and Tc(0001) induced moments at the interface and the subsurface Tc layers, Tc(I) and Tc(I-1), for the double- and single-**Q** states in units of μ_B using.

	Fe	Tc(I)	Tc(I-1)
uudd $\left(3\overline{\Gamma\mathrm{K}}/4\right)$:	2.42,2.43	0.02,0.01	0.0
$\mathbf{Q}_{3\overline{\Gamma\mathrm{K}}/4}$:	2.51	0.01	0.0
uudd $\left(\overline{\mathrm{M}\Gamma}/2\right)$:	2.42,2.35	0.05,0.02	0.01
$\mathbf{Q}_{\overline{\mathrm{M}\Gamma}/2}$:	2.44	−0.04	0.01

Using equations (5.14 and 5.8), from the *uudd* $\left(3\overline{\Gamma\mathrm{K}}/4\right)$ double-**Q** and the multi-**Q** states results, we can now calculate the higher order interaction terms B_1 and K_1. Then we use equation (A-20) to fit the spin spiral results along $\overline{\Gamma}$-$\overline{\mathrm{K}}$-$\overline{\mathrm{M}}$. The GGA results are shown in table 5.5. Referring to the calculated phase diagrams (Fig. 5.6), our calculated J_1, J_2 and J_3 confirm our prediction of Néel ground state of Fe monolayer on Tc(0001) substrate.

Table 5.5: GGA results of Heisenberg exchange constants for the hcp Fe ML on Tc(0001) substrate obtained by fitting the total-energy dispersion along $\overline{\mathrm{M}}$-$\overline{\Gamma}$ and the higher order terms B_1 and K_1

(meV)	J_1	J_2	J_3	J_4	B_1	K_1
Fe/Tc(0001):	-15.6	-1.3	-7.6	-0.7	3.2	1.2

Using the calculated phase diagrams (Fig. 5.6), confirms that Fe has 120° Néel ground state on Tc(0001), if we use the calculated J's values. This is a surprising result, because the stability of the Néel state is dominated by J_1 which is, according to table 5.5, a factor of 10 compared to J_2.

Due to the radioactivity of the substrate, there are no experimental studies to compare our calculated results and predictions for an Fe monolayer on Tc(0001) hexagonal substrate. Since Ru is neighboring element to Tc with one electron more in the $4d$-band, we can justify our results to be consistent with what was experimentally observed for Fe on Ru(0001)[135, 139, 136, 140]. This leads us to the next section where we present an overall comparison of the SS dispersion curves, double- and multi-**Q** states for Fe monolayer on $4d$-TMs hexagonal substrates.

5.2.4 Comparison of Fe magnetic order on $4d$ hexagonal substrates:

If we look back to Fig. (5.3), we can see that the magnetic order of Fe on Rh, Ru, Ir or Re is close to a transition region. In the last subsection, we used first principles DFT calculations to show that Fe possess a collinear double-RW-AFM ground state on Rh(111) substrate, called *uudd* $\left(\overline{\mathrm{M}\Gamma}/2\right)$. This four spin magnetic unit cell was constructed by a superposition of two spin spiral points ($\pm\mathbf{Q}_{\overline{\mathrm{M}}/2}$) at $\pi/2$ rotation angle in Fourier space along the high symmetry line $\overline{\mathrm{M}}$-$\overline{\Gamma}$ of the two dimensional hexagonal IBZ. We also showed that Fe has a Néel ground state on the Tc(0001) substrate. To have a connection between our results, we know that Ru is between Rh and Tc in the $4d$-transition metals series. In this subsection we will use the performed spin spiral calculations for Fe monolayer on Ru(0001) substrate (ref. [57]) to compare to our results, and to try to understand the trend of the Fe ground state if we change the substrate by increasing the $4d$-band filling. In addition, we will try to connect our double-**Q** (*uudd*) results, with what was calculated for Fe/Ru(0001). Then we try to estimate the correction we should add to the model Hamiltonian (eq. A-20 and A-21) we used to calculate the exchange and higher order interactions parameters.

In figure 5.13, we show a comparison of the total energies of spin spirals, double- and multi-**Q** states for Fe monolayer on Ag(111), Rh(111), Ru(0001) and Tc(0001) hexagonal

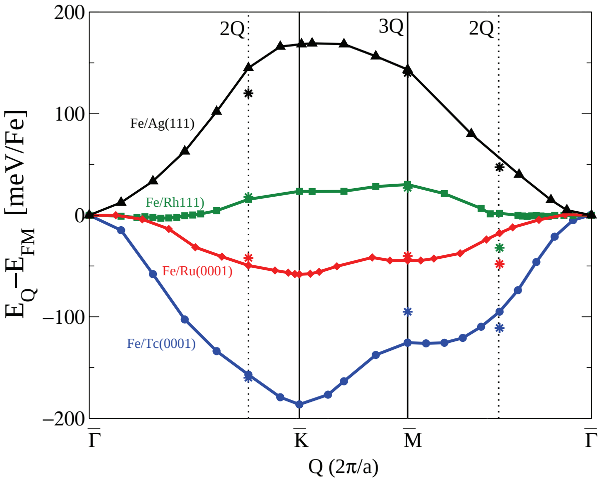

Figure 5.13: (a) Total energy of spin spirals for 1 ML Fe/4d relative to Γ-point. Green (Blue) solid squares (circles) connected by solid lines are our GGA results for Fe on Rh (Tc) hexagonal substrates. Red (Black) solid diamonds (up-triangles) connected by solid line are the GGA results of Fe on Ru (Ag) hexagonal substrates taken from ref. [57] ([30]). Our calculated double- and multi-**Q** states GGA total energies for Fe on Ag, Rh and Tc results are presented by stars. Ru double- and multi-**Q** states GGA results are taken from ref. [57].

substrates. We can see from this comparison how the Fe magnetic ground state changes by increasing the 4d-band filling, i. e. tuning the substrate from Tc through Ag. The strength of the exchange interactions can also bee seen, with the negative nearest neighbors interactions dominate for the early 4d-TMs substrates to stabilize the Néel ground state on Tc and Ru, while at the positive neighbor interactions dominate and stabilize the FM ground state for the Ag or Pd substrate. In between, i. e. only for the Rh substrate, complex magnetism appears, due to the higher interactions, especially when $J_3 \approx -J_1$ as illustrated in figure 5.14.

After inserting the Js into the phase diagram of the 2D Heisenberg model, shown in figure 5.15, we can provide a complete picture of the substrates' impact on the Fe exchange coupling by including spin spiral calculations for an Fe ML on Tc(0001), Ru(0001), Rh(111), and Ag(111). In the J_1-J_2 plane of the diagram, we see that the d-band filling of the substrate drives the system along the line $J_2 \approx 0$ from a Néel configuration on Tc and Ru to the FM solution on Rh and Ag. For small J_1, we need to consider also the phase diagrams in the J_2-J_3 plane showing the spin spiral minimum of Fe on Rh(111) in the $\overline{\Gamma \mathrm{K} \mathrm{M}}$-direction, Fig. 5.15(c), and the 120° Néel state of Tc(0001), Fig. 5.15(b).

For itinerant magnets such as iron, it is not *a priori* clear that the Heisenberg model,

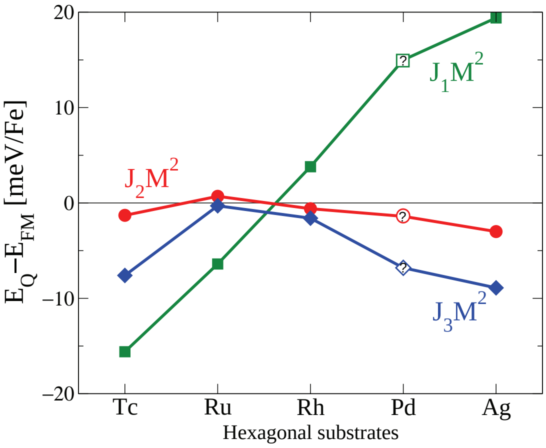

Figure 5.14: Heisenberg exchange interaction parameters $J_1\mathbf{M}^2$ (green squares), $J_2\mathbf{M}^2$ (red circles) and $J_3\mathbf{M}^2$ (blue diamonds) obtained from spin spiral calculations for Fe monolayer on $4d$ hexagonal substrates. Open symbols with (?) indicate that these are expected values. Ru (Ag) results are taken from Ref.[57] ([30]).

which relies on localized magnetic moments, can provide a good description. We have seen this in the *uudd* $\left(\overline{\mathrm{M}\Gamma}/2\right)$ double-$\mathbf{Q}$ structure, where the substrate magnetic moments were not equally induced in Fe/Rh(111). On the other hand Fe moments on Tc(0001) were also not equal. If we compare our the double-$\mathbf{Q}$ results to Fe/Ru(0001) (from ref [57]), then we might have an idea how to modify the Heisenberg model Hamiltonian, to be able to include interaction terms for highly polarized substrates, like Tc, Ru and Rh, which then will increase the accuracy of predicting the magnetic ground state.

In figure 5.16, we compare the energy differences between the single-$\mathbf{Q}$ and the double-$\mathbf{Q}$ *uudd* $\left(\overline{\mathrm{M}\Gamma}/2\right)$ and *uudd* $\left(3\overline{\Gamma\mathrm{K}}/4\right)$ for Fe monolayer on $4d$ hexagonal substrates. From the *uudd* $\left(3\overline{\Gamma\mathrm{K}}/4\right)$ results, we see that adding the substrate to the Fe ML changes almost nothing in the energy differences between single- and the double-$\mathbf{Q}$. The Fe moments were, as expected, increasing with the $4d$ band filling from Tc through Ag.

The situation is different in case of *uudd* $\left(\overline{\mathrm{M}\Gamma}/2\right)$ configuration, where we see the change of moments in Fe film for the case of Tc and Ru, while on Rh, Pd and Ag, there is no variation of Fe moments in the 4-atoms unit cell. On the other hand, the $4d$(I) induced moments are strongly polarized for Rh(I) and Ru(I) layer atoms. Also, there is small (large) difference between the spin spiral single- and the *uudd* double-$\mathbf{Q}_{\overline{\mathrm{M}\Gamma}/2}$ Fe ($4d$(I)) moments while it is larger for the $4d$(I) atoms, as shown in table 5.6. The effect of these changes in Fe and $4d$(I) magnetic moments can be seen in the energy differences, where there is large ($\approx$30) meV/Fe energy gain due to the substrate in the middle of the $4d$-series.

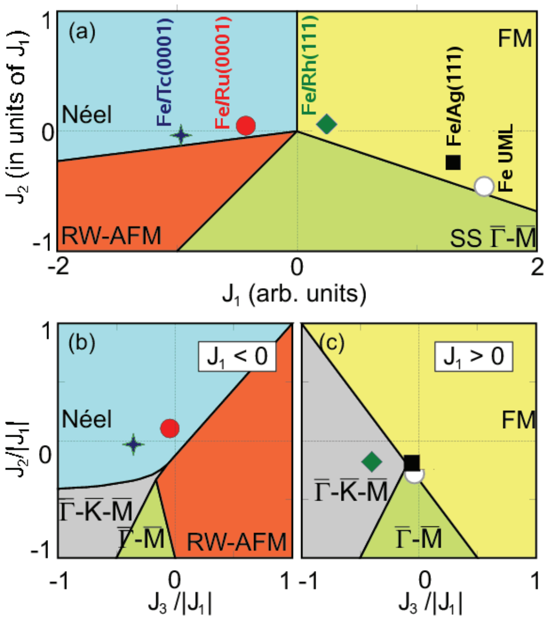

Figure 5.15: Phase diagrams of the classical Heisenberg model for a 2D hexagonal lattice for states on the high symmetry lines. (a) J_1-J_2 plane for $J_3 = 0$. J_2-J_3 plane for (b) $J_1 > 0$ and (c) $J_1 < 0$. (Filled symbols denote values obtained from fits for the Fe ML on $4d$-TM substrates).

From these interesting results, we can modify the Heisenberg model Hamiltonian (eq. 3.22), by adding an additive term, which includes the magnetic moments variation multiplied by a Stoner parameter, I_{Fe} $(+I_{sub})$:

$$H_{\text{2-spin}} = -\sum_{\substack{i,j\\ i>j}} J_{ij}\, \mathbf{M}_i \cdot \mathbf{M}_j + \frac{1}{2}\sum_i I_i \mathbf{M}_i^2 \tag{5.16}$$

with

$$\sum_i I_i \mathbf{M}_i^2 = I_{\mathrm{Fe}} \mathbf{M}_{\mathrm{Fe}^{1\mathbf{Q}}} + I_{\mathrm{sub}} \mathbf{M}_{\mathrm{sub}^{1\mathbf{Q}}} \tag{5.17}$$

for the single-$\mathbf{Q}$ state and

$$\begin{aligned}\sum_i I_i \mathbf{M}_i^2 \quad &= I_{\mathrm{Fe}}[(\mathbf{M}_{\mathrm{Fe}^{1Q}} + \delta\mathbf{M}_{\mathrm{Fe}^{1Q}-\mathrm{Fe}_1^{2Q}})^2 + (\mathbf{M}^2_{\mathrm{Fe}^{1Q}} + \delta^2\mathbf{M}_{\mathrm{Fe}_1^{2Q}-\mathrm{Fe}_2^{2Q}})^2] \\ &+ I_{\mathrm{sub}}[(\mathbf{M}_{\mathrm{sub}^{1Q}} + \delta\mathbf{M}_{\mathrm{sub}^{1Q}-\mathrm{sub}_1^{2Q}})^2 + (\mathbf{M}_{\mathrm{sub}^{1Q}} + \delta\mathbf{M}_{\mathrm{sub}_1^{2Q}-\mathrm{sub}_2^{2Q}})^2]\end{aligned} \tag{5.18}$$

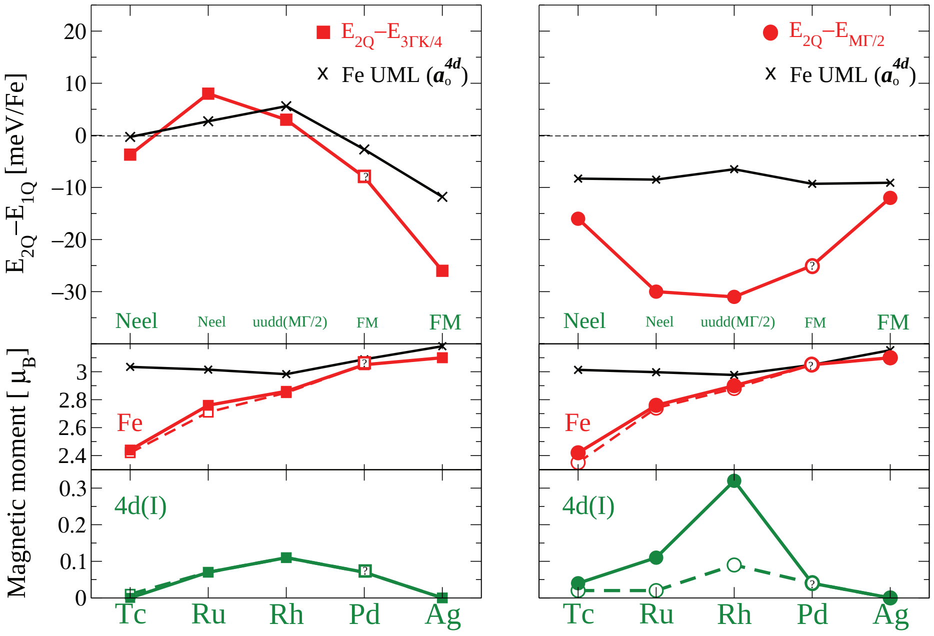

Figure 5.16: Magnetic moments and total energy comparison of $(E_{\mathbf{2}Q} - E_{\mathbf{1}Q})$ between *uudd* $\left(3\overline{\Gamma\mathrm{K}}/4\right)$ (left) and *uudd* $\left(\overline{\mathrm{M}\Gamma}/2\right)$ (right) configurations for Fe monolayer on 4d-TMs substrates. (?) means a result that is expected but not calculated.

Table 5.6: GGA results of Fe and 4d(I) magnetic moments moments from spin spirals calculations at $\mathbf{Q}_{\overline{\mathrm{M}\Gamma}/2}$, and the change in their moments between spin spirals and collinear *uudd* $\left(\overline{\mathrm{M}\Gamma}/2\right)$ calculations, and between the moments in the same double-$\mathbf{Q}$ configuration using results in figure 5.16.

	Tc (μ_S)	Ru (μ_S)	Rh (μ_S)
$\mathbf{M}^{Fe}_{Q_{\overline{\mathrm{M}\Gamma}/2}}$	2.44	2.71	2.88
$\delta\mathbf{M}(\mathrm{Fe}^{1Q}{-}\mathrm{Fe}^{2Q}_1)$	0.0	0.0	0.0
$\delta\mathbf{M}(\mathrm{Fe}^{2Q}_1{-}\mathrm{Fe}^{2Q}_2)$	0.07	0.05	0.02
$\mathbf{M}^{4d(I)}_{Q_{\overline{\mathrm{M}\Gamma}/2}}$	0.04	0.04	0.18
$\delta\mathbf{M}(4\mathrm{d}^{1Q}{-}4\mathrm{d}^{2Q}_1)$	0.01	0.0	0.14
$\delta\mathbf{M}(4\mathrm{d}^{2Q}_1{-}4\mathrm{d}^{2Q}_2)$	0.03	0.09	0.23

for the double-**Q** state.

Here I_{Fe} (I_{sub}) is the Stoner parameter of Fe (substrate), $\mathbf{M}_{\mathrm{Fe}^{1\mathrm{Q}}}$ ($\mathbf{M}_{\mathrm{sub}^{1\mathrm{Q}}}$) is the magnetic (induced) moment of Fe (substrate) calculated from single-**Q** state, $\delta\mathbf{M}_{\mathrm{Fe}^{1\mathrm{Q}}-\mathrm{Fe}_1^{2\mathrm{Q}}}$ ($\delta\mathbf{M}_{\mathrm{sub}^{1\mathrm{Q}}-\mathrm{sub}_1^{2\mathrm{Q}}}$) is the magnetic local (induced) moments difference between Fe (substrate) from single-**Q** and the first Fe (substrate) local (induced) moments from double-**Q** state, and $\delta\mathbf{M}_{\mathrm{Fe}_1^{2\mathrm{Q}}-\mathrm{Fe}_2^{2\mathrm{Q}}}$ ($\delta\mathbf{M}_{\mathrm{sub}_1^{2\mathrm{Q}}-\mathrm{sub}_2^{2\mathrm{Q}}}$) is the difference between the first Fe (substrate) and the second Fe (substrate) local (induced) moments.

Using equation (5.19), the difference between the single- and double-**Q** model Hamiltonian (eq. 5.14) can be expressed as:

$$\begin{aligned} E_{uudd} - E_{3\overline{\mathrm{K}}/4} &= E_{uudd} - E_{\overline{\mathrm{M}}/2} = 4\{2K_1 - B_1\} \\ &+ I_{\mathrm{Fe}}(\delta^2\mathbf{M}_{\mathrm{Fe}^{1\mathrm{Q}}-\mathrm{Fe}_1^{uudd}} + \delta^2\mathbf{M}_{\mathrm{Fe}_1^{uudd}-\mathrm{Fe}_2^{uudd}}) \\ &+ I_{\mathrm{sub}}(\delta^2\mathbf{M}_{\mathrm{sub}^{1Q}-\mathrm{sub}_1^{uudd}} + \delta^2\mathbf{M}_{\mathrm{sub}_1^{uudd}-\mathrm{sub}_2^{uudd}}). \end{aligned} \tag{5.19}$$

From this equation we see, that if the substrate unpolarized, like in *uudd* $\left(3\overline{\Gamma\mathrm{K}}/4\right)$ case, the substrate terms cancel, and almost no change or effect is expected on the Heisenberg model Hamiltonian, by adding the substrate if the Fe moment remains constant. This can bee seen in our results as mentioned above (Fig. 5.16), where adding the substrate to Fe UML did not change the trend of the total energy differences. Where as, if Fe moments change due substrate polarization, as in case of *uudd* $\left(\overline{\mathrm{M}\Gamma}/2\right)$ configuration, the model Hamiltonian is modified and adding the substrate to Fe UML will affect the total energy differences between signaler- and double-**Q**. If we use Fe and Rh(I) *uudd* $\left(\overline{\mathrm{M}\Gamma}/2\right)$ moments (tab. 5.6) in equation (5.19), we find out that the maximum change in the total energy differences, between single- and double-**Q**, will occur if we add Rh substrate to the Fe UML, this is also consistent with our results (Fig. 5.16).

In conclusion of this chapter, we have studied the magnetism of Fe monolayer on $4d$-TM hexagonal substrates. Firstly, we performed structural relaxations for the Fe and $4d$(I) layer to optimize Fe-Rh(I) interlayer distance. We performed total energy collinear calculations to calculated Fe ground state on Rh, Pd, Tc substrates, and compared our results with previous collinear calculations of Fe ground state on Ru, Re, Ir, Pt, Os, to have a complete picture of the effect of the substrate on the Fe ground state. We found that $4d$-TMs substrates produce the similar collinear results like $5d$-TMs. Using total energy differences, We found that Fe collinear ground state is FM on fcc hexagonal substrates (Rh, Pd, Ir, Pt) and RW-AFM on hcp substrates (Tc, Ru, Re, Os). We found a small total energy difference between FM and RW-AFM of Fe monolayer on Ru and Rh (Os and Ir), which indicates that on these substrates Fe is very close to phase transition. From experiments and non-collinear theoretical DFT calculations, Fe monolayer was found to have a Néel ground state on Ru(0001) and a complex magnetic ground state on Ir(111) surfaces. This encouraged us to see what happens to Fe magnetism on Rh(111) substrate by performing non-collinear total energy calculations of flat spin spirals, which are the general solution to the classical Heisenberg model, along the high symmetry line $\overline{\Gamma}$-$\overline{\mathrm{K}}$-$\overline{\mathrm{M}}$-$\overline{\Gamma}$

in the hexagonal 2DIBZ. If the nearest neighbor interactions are weak, then higher order interactions will play a crucial role to stabilize the magnetic ground state of the system, and must not be ignored. This leads to a lifting of the degeneracy in Heisenberg model for linear combinations of two different spin spirals, $\mathbf{Q}_{3\overline{\Gamma K}/4}$ and $\mathbf{Q}_{\overline{\mathrm{M}\Gamma}/2}$. Then we could calculate the higher order interactions from the total energy difference between $\mathbf{Q}$ and a superposition of $\pm\mathbf{Q}$. The superposition of $\pm\mathbf{Q}$ is mapped to real space by 4 atoms per unit cell will double-RW-AFM order. Instead of the FM ground state from collinear calculations, we found that the higher order interactions do stabilize a collinear double-RW-AFM ground state constructed from $\mathbf{Q}$s along the high symmetry line $\overline{\mathrm{M}}$-$\overline{\Gamma}$ for Fe monolayer on the Rh(111) substrate. We also studied Fe on Tc by performing non-collinear calculations and found that Fe monolayer has a 120° Néel ground state on Tc(0001), which is different from the RW-AFM ground state that would be predicted by collinear calculations using 2 atoms per unit cell.

At the end of the chapter we compared our non-collinear results for Fe monolayer on $4d$-TMs. Due to geometrical effects along the high symmetry line $\overline{\mathrm{M}}$-$\overline{\Gamma}$, the strongly polarized $4d$ substrate will break the degeneracy of the $\mathbf{Q}_{3\overline{\Gamma K}/4}$ and $\mathbf{Q}_{\overline{\mathrm{M}\Gamma}/2}$ in Heisenberg model. This lead us to modify the model Hamiltonian by adding a term which depends on the substrate Stoner parameter and the induced moments of the substrates.

Chapter 6

Co MCA from monolayers to atomic chains

In chapter 4, we presented the calculated magnetocrystalline anisotropy (MCA) for $3d$-TMs monolayers on Rh(001) substrate (sec. 4.2.3). Among the $3d$-TMs monolayers on Rh(001), we found the largest out-of-plane (in-plane) MCA values for Fe (Co). This was consistent with the theoretical prediction that the MCA strongly changes its easy axis, between out-of- and in-plane, with the band filling for the late $3d$-,$4d$- and $5d$-TMs on (001) substrates[86]. In this sense we expect the same trend to happen on hexagonal surfaces.

After showing the structural relaxations of Co on Ru, Rh, and Pd, we will compare them with the Fe results, we will also show the calculated MCA results for Fe and Co monolayers on Ru, Rh and Pd substrates. Furthermore, we will show a MCA calculation of a Cobalt atomic chain on the Rh(664) step edge, and compare the results with Co/Pt(664)[151].

6.1 Relaxations and magnetic order:

We calculated the structural FM relaxations of Co monolayer on Ru(0001), Rh(111) and Pd(111) substrates, in the same way as explained in subsec. (4.3.1) with the same numerical parameters. From figure 6.1, we compare the FM relaxations of Fe and Co, Δd_{12} and Δd_{23}, and the optimized interlayer distances. We see that the Co FM relaxations, Δd_{12}, are stronger on the same substrate compared to the Fe monolayer. This can be referred to the smaller GGA bulk lattice constant calculated for fcc Co, 3.54 Å[152] as compared to fcc high spin (HS) FM Fe, 3.65 Å[153], which leads to a stronger mismatch for Co-$4d$ lattice, therefore stronger relaxations for Co are expected. The relaxation of the $4d$(I) interface layer, Δd_{23}, modifies the optimized interlayer distance, d_{12}, conserving the same trend of Δd_{12}. The smallest difference between Co and Fe FM relaxations occurs for Pd, which indicates that smallest hybridization are expected on Pd, which will not affect substantially the Co or Fe magnetic properties. This has been confirmed in last chapter were Fe monolayer did not change its FM ground state on Pd(111).

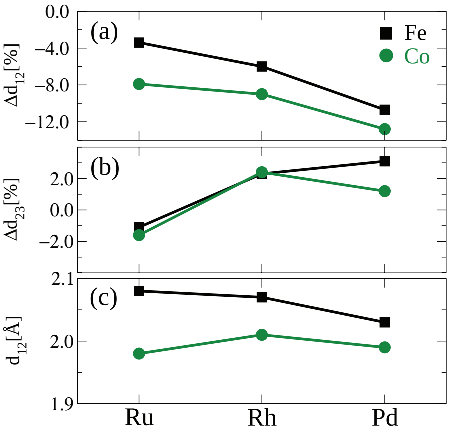

Figure 6.1: $3d$ and $4d$(I) FM relaxations, Δd_{12} (a) and Δd_{23} (b), of Co (Fe) on hexagonal $4d$ substrates are presented by solid green circles (black squares) connected by solid line. The corresponding changes are given with respect to the $4d$ substrates bulk interlayer spacing, which is 2.15, 2.21 and 2.28 Å for Ru, Rh and Pd, respectively. (c) The optimized $3d$-$4d$ interlayer distance d_{12} for Fe and Co on hexagonal $4d$ substrates.

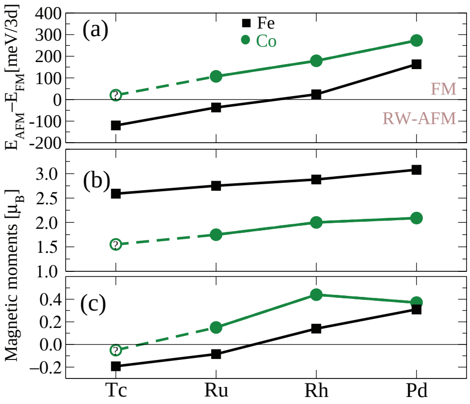

Figure 6.2: (a) Total energy differences between RW-AFM and FM configuration are presented by solid circles (squares) for Co (Fe) monolayer on Ru, Rh, Pd hexagonal substrates, positive (negative) values indicate that the FM (RW-AFM) is favorable. (b) The $3d$ magnetic local moments are denoted by green circles (black squares) for the Co (Fe) monolayer. And (c) $4d$ substrates' interface layer induced moments.

To investigate the magnetic order, we performed collinear calculations to obtain the total energy differences between RW-AFM and FM configurations (Fig. 6.2) of Co monolayer on Ru, Rh, and Pd hexagonal substrates. Co monolayers remain always FM on $4d$ hexagonal substrates, with a tendency towards a RW-AFM phase transition as we tune the substrate from Pd (+275 meV/Co) to Ru (+107 meV/Co). The same trend was observed in the last chapter for an Fe monolayer, but the phase transition occurs earlier on Ru(0001). We expect a Co monolayer to remain FM on Tc(0001), but with lower energy difference than on Ru. This increases the possibility of higher order interactions to stabilize a complex magnetic ground state of a Co monolayer on Tc(0001), analogous to Fe on Rh(111), where the energy difference was close to a phase transition with +24 meV/Fe atom. This agrees with the c(2×2)-AFM ground state of Co monolayers on W(001)[7], although Co/W(001) has a square lattice but, it supports our results of the last chapter, where it was found that the band filling can control the ground state even for strong ferromagnets like cobalt.

6.2 MCA of Co monolayer on $4d$ substrates:

In this section we will show the calculated MCA for Co monolayers on hexagonal $4d$-TM substrates. We will compare Co to Fe results, to see the effect to the $3d$ band filling on the $3d$-monolayer MCA on the same substrate. We tested the convergence of the MCA of Co and Fe on Rh(111) and found converged results for 2118 k-points in the full 2DBZ, using force theorem[128] to calculate the energy difference between the two spin quantization axes, in- and out-of-plane, starting from the same self consistent scalar-relativistic potential.

In figure 6.3, we compare the supported with unsupported monolayers results, using the $4d$-lattice constant. considering the Fe MCA value for Fe on Ru(0001) (Rh(111)), we have to keep in mind that it is calculated for FM configuration, and we know from last chapter that Fe has a 120° Néel (double-$\mathbf{Q}_{\overline{\mathrm{M}}}/2$) ground state. From Fe FM MCA results, we only can see the effect of the $3d$ band filling on the same $4d$ substrate. We notice that for the Co the large in-pane MCA value of the UML was suppressed by the $4d$ substrate by about 0.5 meV/Co change towards the out-of-plane direction, while the Fe MCA was not much affected by adding the $4d$ substrate.

This is also clearly seen in the orbital moment anisotropy (OMA), were Co OMA is driven towards an out-of-plane, larger orbital moments in the out-of-plane direction. This shows the consistency of our results with the assumption that the MCA of transition-metal monolayers is driven by the orbital moments anisotropy[55]. On Ru(0001) (Rh(111)), cobalt has an out-of-plane magnetization with +0.17 (+0.40) meV/Co atom, where it has an in-plane magnetization on Pd(111) with −0.05 meV/Co atom. To see the relaxation effect on MCA, we used force theorem to analyze how does MCA depends on the interlayer distance between Co and Rh(I), as shown in figure 6.4. We chose Co/Rh(111) as an example, because we did the k-point convergence test also for Rh(111) substrate. From figure 6.4, we see that MCA is enhanced by decreasing the interlayer distance till Co monolayer reaches the relaxed position. From the force theorem (FT) results, it increased from +0.25 to +0.40

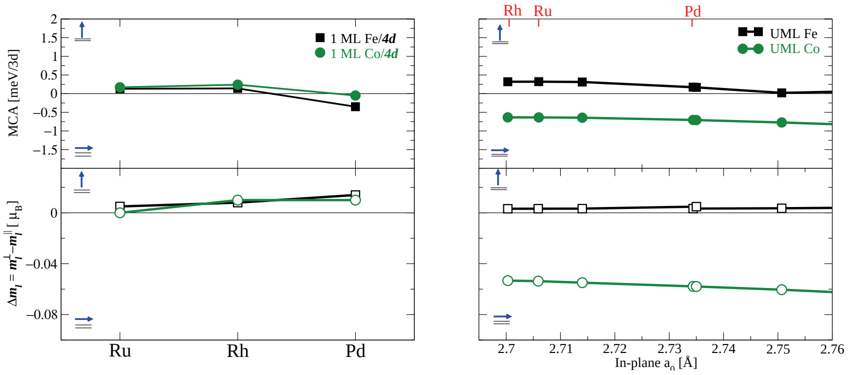

Figure 6.3: Top: Magneto-crystalline anisotropy (MCA) presented by solid circles (squares) for 1 ML Co (Fe) on Ru(0001), Rh(111) and Pd(111) (left) compared with UML results with different lattice constants in (right). Bottom: orbital moments anisotropy (OMA) presented by open circles (squares) (bottom). Positive MCA means an out of plane and negative MCA means in-plane magneto-crystalline anisotropy. All calculations assuming FM order.

meV/Co atom, which is similar to the self consistent increase, from 0.12 to 0.25 meV/Co. This shows the importance of relaxations for MCA calculations. Using FT, we also calculated the Co contribution, by switching of the spin-orbit coupling in the Rh atoms. This gives us an indication about the hybridization and crystal field effect of the substrate.

Also, from figure 6.4, we see again the Co MCA increased with relaxing the structure. We also notice that the crystal field leads the out-of-plane MCA already for the unrelaxed structure, but with increasing relaxation, it becomes even more dominant. The decrease of the absolute value of MCA as compared to the UML agrees with the fact that electron delocalization and crystal field effects compete with the intra-atomic Coulomb interactions, responsible for Hund's rules, causing a substantial or total decrease of **S** and quenching of **L**[42].

Because Ir has similar nature like Rh but with large spin orbit coupling parameter, we also calculated the relaxations and the magnetic order and MCA for Co monolayer on Ir(111). We found that Co/Ir(111) relaxations with respect to the Ir calculated GGA bulk lattice constant 3.86Å, are very similar to what was obtained for Co/Rh(111) (see fig. 6.1). We also found that Co prefers FM ground state by +137 meV/Co on Ir(111) substrate, with $\Delta d_{12} = -9.6\%$ and $\Delta d_{23} = +1.7\%$ relaxations . Also we found that a Co monolayer has an out-of-plane magnetization on the Ir(111) with an anisotropy of +0.40 (0.44) meV/Co using force theorem (self consistent). From the self consistent results, we see that the MCA of Co/Rh(111) is about 0.20 meV/Co atom less than for Co/Ir(111). This difference reflects the strength of Ir spin-orbit coupling parameter. If we compare the

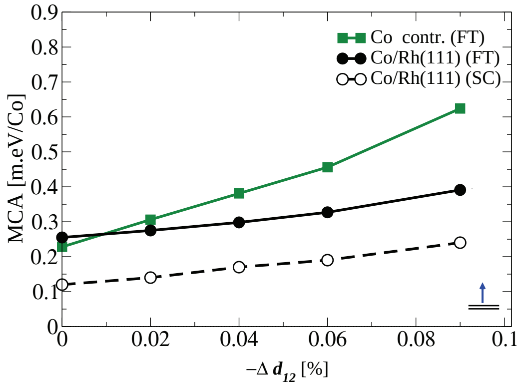

Figure 6.4: MCA of Co/Rh(111) as a function of the Co-Rh(I) relaxation, $-\Delta d_{12}$; using the Force Theorem (FT) or self consistent (SC). The Co-contribution (green) was relaxed using the FT.

Co OMA $(m_l^{\perp} - m_l^{\parallel})$ between both Rh(111) and Ir(111) substrates, we find the same MCA trend, where Co OMA is +0.013 μ_B for Co/Rh(111) and +0.021 μ_B for Co/Ir(111).

To study the MCA from an experimental point of view, 5*d*-TMs are usually used as substrates, due to their large spin orbit coupling parameter, which leads to large orbital moments and then large MCA values as it was explained in section (3.4). From our MCA study of the Co monolayer on 4*d*-TMs substrates we can speculate by the 5*d*-TMs substrates effect. It is computationally very expensive to study the 5*d*-TMs as substrates, so we have chosen 4*d*-TMs, since they have a similar chemical trend, as was shown above for Co/Rh(111) and Co/Ir(111). This will provide a complete picture to experimentalists about which 5*d*-TM will produce an interesting Co or Fe MCA results. For example, in the case of Pd(111), Fe and Co have both an small in-plane MCA, −0.05 meV/Co atom and −0.30 meV/Fe atom, therefore one would expect that the probability of having an out-of-plane magnetization is very high on Pt(111), because Pt has larger spin-orbit coupling parameter than Pd. This interpretation is consistent with what was experimentally done by Moulas *et al.* [154] to investigate the magnetic anisotropy energy (MAE) of Fe_xCo_{1-x} monolayer thick film on a Pt(111) substrate, starting from zero Fe concentration. i. e. a pure Co monolayer, and ending with a pure Fe monolayer. They found that the magnetic anisotropy energy shows minima for pure Fe or Co monolayers, with small out-of-plane values. For thicker films one has to keep in mind that the shape anisotropy gets increasingly important and leads to more negative values of the MAE.

6.3 Co atomic chain on Rh(664):

Up to now, we were always dealing with two dimensional magnetic monolayers on non-magnetic substrates. We know, from Stoner model (sec. 3.1), that reducing the dimensionality of the system will lead to an enhancement of the magnetic moment, where non magnetic materials may become magnetic in low dimensions[86]. We also know, from section (3.4) that the magnetic anisotropy is affected by lowering the dimensionality of they system, because of considerably enhanced orbital moments. After studying 2D monolayers magnetic properties, it will be also interesting to go to one dimensional systems, especially to study their magnetic anisotropy, which is one important quantity due to its role of stabilizing magnetic properties at finite temperature. Experimentally, it is more comfortable to investigate atomic chains on step-edges than on flat surfaces. For atomic chains, it is sometimes possible to evaporate the magnetic metal they want to study, and then it will be naturally assembled as an atomic-chain at the step-edge. Many theoretical and experimental studies were performed to investigate the magnetic properties of atomic chains deposited on step surfaces, especially, with the arrival of advanced Scanning Tunneling Microscope (STM) techniques, in combination with X-Ray Magnetic Circular Dichroism (XMCD) to study the magnetic properties of low dimensional systems. Therefore it became possible to arrange atoms in chains along steps of suitable substrates and to analyze their properties[39, 40]. This opened the door to study the magnetic properties of metallic chains on step-edges. For example, ferromagnetism was observed in one-dimensional mono-atomic metal chains[41], and a giant magnetic anisotropy of single cobalt atoms and nanoparticles[42], an oscillatory magnetic anisotropy in one-dimensional atomic wires of different thickness[43]. In-plane magnetocrystalline anisotropy was observed on Fe/Cu(111) nanostructures grown on stepped surfaces[44, 45], and observation of spin and charge collective modes in one-dimensional metallic chains[40]. The spin and orbital magnetization was investigated in self-assembled Co clusters on Au(111) step-edge. A strong magnetic surface anisotropy of ultrathin Fe was observed on curved Pt(111)[46] and finally spin and orbital magnetization was explored in self-assembled Co clusters on Au(111)[47].

Because of our data base on Co monolayers on Rh(111), we will complete the picture by studying a Co atomic-chain on a Rh step-edge. We have seen that a Co monolayer has an out-of-plane MCA on Rh(111), and induces large Rh out-of-plane orbital moments (+0.13 μ_B). In this section we will show our results of Co atomic-chain on Rh step edge, obtained from DFT calculations using GGA exchange correlation potentials. To justify our results we will compare them to a previous theoretical study that was preformed on Co/Pt(664)[151].

6.3.1 Theoretical model and relaxation results:

Theoretically, step surfaces can be simulated by a vicinal (111) surface with p-atomic rows terrace width. Two types, A-type and B-type, of closed packed steps can be formed on an fcc(111) surface. In the A-type, the step-edge atoms and the surface atoms of the lower terrace form a square unit cell (like on a fcc (001) surface), while they form a triangle, as on fcc(111) surface, in B-type step. These types of steps are called ⟨001⟩ or ⟨111⟩ microfaceted for A- and B-type, respectively. An example of B-type is a (p, p, $p-2$) surface which consists of terraces with a width of p full atomic wires. For example, a Co wire on a B-type step edge can be modeled by Rh(111) surface which is cut in a way that produces Rh terraces with 6-atomic rows, i. e. a Rh(664) surface with each Rh-edge atom is replaced by Co, as illustrated in figure 6.5.

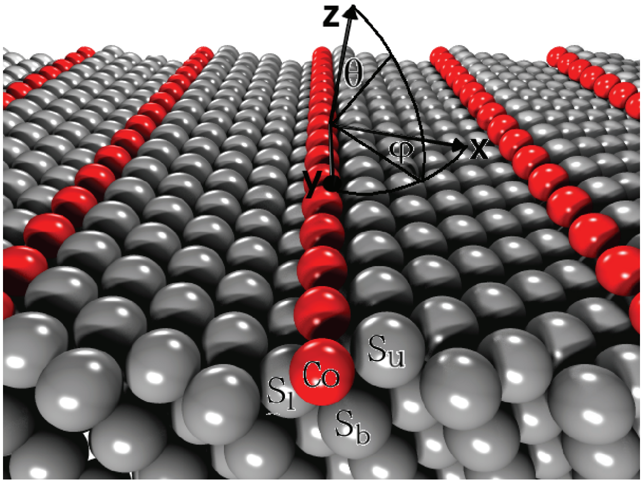

Figure 6.5: A Rh(664) surface (S) atoms shown as gray spheres, the step-edge atoms are replaced by Co atoms represented as smaller red spheres. The three surface atoms that are nearest neighbors to the step-edge Co atom are indicated: in the upper terrace $\mathrm{S_u}$, the lower terrace $\mathrm{S_l}$ and in the direction of the bulk $\mathrm{S_b}$. The angles θ and φ characterizing the direction of the spin-quantization axis are indicated with respect to the terrace normal.

We performed calculations with ab initio full-potential linearized augmented plane wave (FLAPW) method, as implemented in the `FLEUR` code[50]. The calculations are based on GGA[69]. In our simulations of the Co atomic chain on Rh(664) surface, we used symmetric film geometry (Fig. 6.5) with 45 atoms per unit cell. We used the Rh in-plane lattice constant, 2.70 Å, and the six topmost interlayer distances were relaxed by force calculations. We used about 90 basis functions/atom with a muffin-tin radius of 1.22 Å for the Co chain atoms and 1.28 Å for the Rh atoms. The irreducible part of the surface Brillouin zone was sampled with 42 $\mathbf{k}_{\parallel}$ points.

In table 6.1, we show the relaxation results of the Co atoms in a chain decorating the Rh(664) step edge calculated with respect to the ideal atom spacing in bulk Rh. From these results we notice that the Co relaxations with the upper terrace Rh atoms Co-Rh$_u$ are smaller by factor of one half than the similar Co-Rh$_\mathrm{l}$ and Co-Rh$_\mathrm{b}$ relaxations towards the lower atoms (c. f. fig.6.5). By that we expect a stronger Co hybridization with the lower terrace and the bulk Rh atoms. If we compare Co/Rh(664) relaxation results to what

Table 6.1: GGA Relaxations in percent of the ideal bulk value of the nearest-neighbor bond length of the step-edge Co atom on Rh(664) surface, compared to what was calculated for Co/Pt(664)[151]. The positions of the nearest-neighbor Rh atoms are indicated in Fig. 6.5.

Bond direction	Co-S_u	Co-S_b	Co-S_l
Co/Rh(664)	-2.6	-7.8	-7.5
Co/Pt(664)	-7.3	-13.3	-7.4

was calculated for Co chain on Pt(664)[151] (Tab. 6.1), we see that Co-Rh_u and Co-Rh_b relaxations are smaller than in the case of Pt by factor of one half. This can be related to the larger Co-Pt lattice mismatch (10%), as compared to Co-Rh (7%). Because the Co-Rh_l and Co-Pt_l relaxations are similar, we expect that there are stronger Co-Pt_u and Co-Pt_b hybridization than for Co-Rh_u and Co-Rh_b.

6.3.2 Magnetocrystalline anisotropy:

We applied force theorem to calculate the magnetocrystalline anisotropy energy (MCA), starting from a self-consistent calculation, where spin-orbit coupling was included, with 156 $k_{\|}$ points were sampled in the full 2DBZ. We calculated MCA for different directions of the spin-quantization axis with respect to the terrace surface normal ($\theta = 0$,$\varphi = 0$). The calculated MCA results are shown in left side of figure 6.6, while we show a three dimensional representation of MCA values on the right side of the figure.

As seen in figure 6.6(a), we scanned the plane perpendicular to the wire ($\theta, \varphi = 0$), and found that the easy axis lies in the plane of the terrace surface, ($\theta = 90, \varphi = 0$), by -0.30 meV/Co atom lower than the terrace surface normal. Then we calculated MCA for all directions in the plane of the terrace ($\theta = 90, \varphi$) with respect to the surface normal, and found that Co prefer to magnetize perpendicular to the chain axes ($\theta = 90, \varphi = 0$). If we look to Co orbital moments (Fig. 6.6.b), we see that largest Co orbital moments are ate angle pointing ($-75°$,0) with respect to the terrace normal, with μ_L =0.139 μ_B and 0.03 μ_B OMA with respect to the surface normal orbital moments. On the other hand, the sum of Rh orbital moments is largest at (60°,0) from the terrace normal. Accordingly, the predicted MCA easy axis should lie in the middle of these extremes, which is very close to the terrace plane.

From these results we see that we got similar MCA value for the Co chain on Rh(644) (-0.40 meV/Co atom) as for the two dimensional Co monolayer on Rh(111) surface (sec. 6.2), but with an in-plane easy axis. This is surprising, since we know that reducing the dimensionality can lead to an effective enhancement of the MCA values[86]. A Similar theoretical study was performed by Baud *et. al* on Co chains on Pt(664) surface[151]. They predicted a Co MCA value in good agreement with the experiment[151], but the easy axis was too much tilted from the terrace normal (82°), as compared to an out-of-plane experimental MCA easy axis, pointing 43° from the terrace normal[41, 43]. Baud *et al.* referred their wrong prediction of the Co magnetization easy axis to the strongly reduced Co orbital moments due to relaxations, since their unrelaxed calculations showed full agreement with

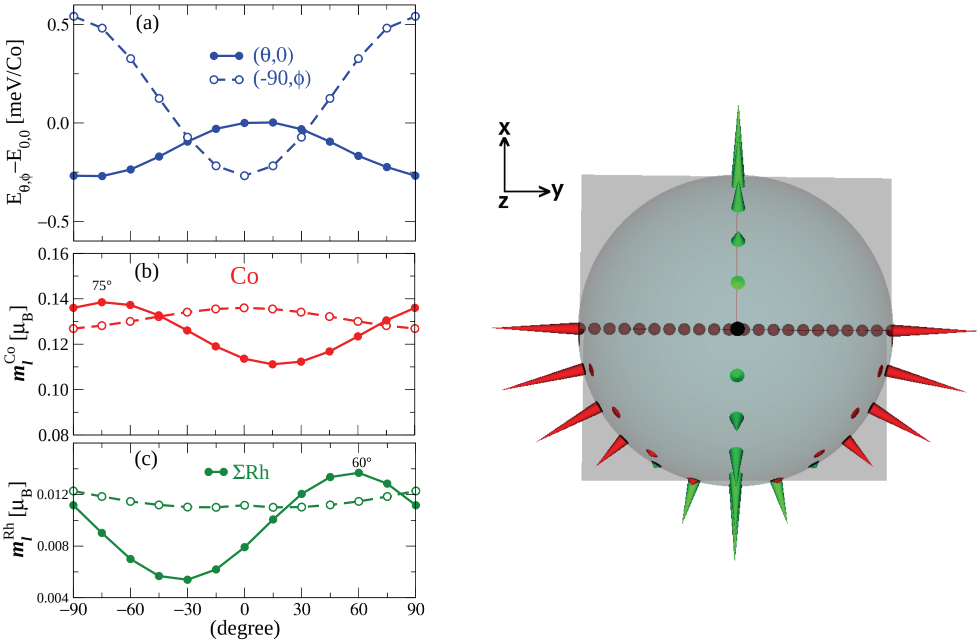

Figure 6.6: Left: Energy of the relaxed Co decorated Rh step edge as a function of the spin-quantization axis SQA calculated with the force theorem (a), Co orbital moments (b), and the sum of all Rh orbital moments (c). Full lines correspond to a variation of the SQA in the xz plane (perpendicular to the wire) (see Fig. 6.5), dashed lines correspond to a variation in the xy plane (terrace plane). Right: A 3D plot of the MCA values simulated to be proportional to a size of green (red) cone for negative (positive) energies with respect to the terrace surface normal energy (black solid circle).

the experimental results. In our case, Co/Rh(664) was not experimentally investigated, we can't verify our results. Instead we compare our relaxed MCA results to the Co/Pt(664) relaxed results to find out some connection which might lead us to a reasonable understanding of some chemical trends and the substrate effect on the Co atomic chain MCA, as we did for the two dimensional case in last section (6.2).

From our MCA calculations at the high symmetry points, $(0,0)$, $(90,0)$, and $(90,90)$, we retrieved the spin and orbital moments of Co atoms and their Rh neighboring atoms, then we compare them to Co/Pt(664) results from Ref. [151], as shown in table 6.2. As expected, Co spin moments increased from 1.97 μ_B on Rh to 2.10 μ_B on Pt, with increasing the d-band filling. We find larger Rh surface induced spin moments than of Pt, although Rh has smaller magnetic susceptibility ($+102 \times 10^{-6}\, cm^3\, mol^{-1}$) than Pt ($+193 \times 10^{-6}\, \mathrm{cm}^3\, \mathrm{mol}^{-1}$)[155]. Additionally, the large induced Rh spin and orbital moments did not compensate Co spin and orbital moments, as Pt spin and orbital moments did. Furthermore, we see that the

Table 6.2: Spin (μ_S) and orbital moments (μ_L) for the atoms in the relaxed Co/Rh(664) and Co/Pt(664) structures. The orbital moments for the spin-quantization axis perpendicular to the vicinal surface ($\theta, \varphi = 0, 0$), parallel to the surface, but perpendicular to the Co wire ($\theta, \varphi = \pi/2, 0$), and parallel to the Co wire ($\theta, \varphi = \pi/2, \pi/2$) is given. The moments for the surface (S) atoms nearest to the Co atom in the upper terrace marked as $\mathrm{S_u}$, in the bulk $\mathrm{S_b}$ and on the lower terrace $\mathrm{S_l}$ are given, as well as the sum of all S moments in the film ($\sum$S).

	Rh(664)				Pt(664)			
	μ_S (μ_B)	μ_L (μ_B)			μ_S (μ_B)	μ_L (μ_B)		
Atom		$0, 0$	$\frac{\pi}{2}, 0$	$\frac{\pi}{2}, \frac{\pi}{2}$		$0, 0$	$\frac{\pi}{2}, 0$	$\frac{\pi}{2}, \frac{\pi}{2}$
Co	1.97	0.114	0.136	0.127	2.10	0.093	0.101	0.060
$\mathrm{S_u}$	0.305	0.013	0.024	0.020	0.239	0.047	0.066	0.083
$\mathrm{S_b}$	0.227	0.009	0.002	0.005	0.220	0.045	0.044	0.054
$\mathrm{S_l}$	0.255	0.009	0.014	0.011	0.231	0.047	0.059	0.064
$\sum$S	0.515	0.008	0.011	0.012	0.210	0.240	0.257	0.257

difference between $\mathrm{Rh_u}$ (0.305 μ_B) and $\mathrm{Pt_u}$ (0.239 μ_B) induced moments is quit larger than for the other Rh and Pt surface atoms neighboring the Co. The explanation might be hidden behind the small inward relaxations of Co-$\mathrm{Rh_u}$ (see tab. 6.1), since the other Co-$\mathrm{Rh_l}$ and Co-$\mathrm{Rh_b}$ relaxations are large as in all Co-Pt, with even very similar induced moments. On the other hand, we find larger Co and $\sum$Rh orbital moments (μ_L) in the terrace plane ($\frac{\pi}{2}, 0$) and ($\frac{\pi}{2}, \frac{\pi}{2}$), than the surface normal $(0, 0)$ orbital moments. The same occurs for Co/Pt(664). Again we notice that, the largest Co and Rh (Pt) orbital moments are those with smallest relaxations Co-$\mathrm{Rh_u}$ and Co-$\mathrm{Pt_u}$. This is a very strong indication that relaxations are very important as was stressed in Ref. [151].

If we compare the Co OMA on Rh(664), we find that it is the same value (0.03 μ_B) as for Co on Pt(664). This is considerably small compared to the experimental Co/Pt(997) OMA value[41], but consistent with our Co MCA results. For Pt case this was inconsistent with the calculated Co large MCA value (2.0 meV/Co atom). To clarify that, we compare Co/Rh(664) MCA results to Co/Pt(664) in the plane of the magnetization easy axis, $(\theta, 0)$, as shown in figure 6.7.

From this comparison, we see that our MCA results for Co/Rh(664) predict the same easy axis as predicted for Co/Pt(664), but with one order of magnitude smaller MCA value. This is expected since Pt has larger spin-orbit coupling parameter than Rh. On the other hand, since we used the same method, numerical parameters, and code, we trace back our larger calculated Co orbital moments to the smaller relaxations of Co-$\mathrm{Rh_u}$ and Co-$\mathrm{Rh_b}$ compared to Co-$\mathrm{Pt_u}$ and Co-$\mathrm{Pt_b}$, while Co-$\mathrm{Rh_l}$ relaxations were similar to Co-$\mathrm{Pt_l}$. This supports the conclusion that relaxing the structure will decrease Co orbital moments which may lead to change the magnetization easy axis, which was the reason behind the deviation of the calculated easy axis for a Co atomic chain on Pt(664) as compared to the experimental observations[151].

As a summary of this chapter, we have analyzed Co magnetic properties as two dimensional monolayer on $4d$-TMS hexagonal substrates. In comparison to Fe, we found that

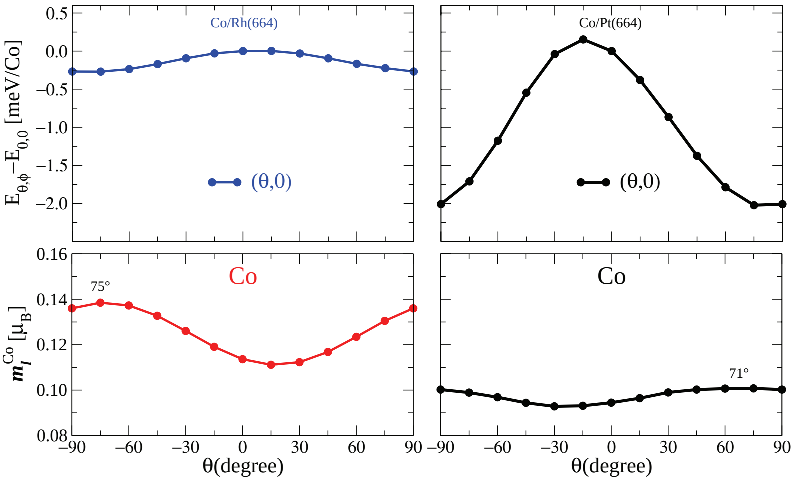

Figure 6.7: Comparison between the results of relaxed Co decorated Rh (left) and Pt (right) step edges.

Co might lose its FM, as for Fe, if we tune the substrate from the late through the early transition metals hexagonal substrates. We calculated the magnetocrystalline anisotropy of Co and Fe monolayer on 4d-TMs hexagonal substrates. We found that Fe MCA is not strongly affected by adding the substrate as Co. This lead us to chose Co, as a case of study, to analyze the MCA of Co atomic chain on microfaceted Rh$\langle 111\rangle$. We compared our results to previous study of Co chain on Pt$\langle 111\rangle$, and found that relaxations play a crucial role to determine a consistent magnetization easy axis with the experimental results, since strong relaxations lead to strong reduction of the theoretical Co orbital moments.

Summary and conclusions

As a conclusion of this thesis, we employed the full-potential linearized augmented plane-wave (FLAPW) method to report a systematic density-functional (DFT) study of the magnetic properties of the $3d$ transition-metal (V, Cr, Mn, Fe, Co and Ni) monolayers deposited on the Rh(001) and Rh(111) substrates. In order to get a better understanding of the magnetic phases which could become realistically possible we have mapped in part the *ab initio* result onto model Hamiltonians, predominantly the Heisenberg model. In some instances the model was amended by a local term describing the Stoner enhanced magnetic polarization of the substrate. From the values and sign of the intersite exchange interaction we have drawn conclusions on the possible magnetic structure. For Fe on Rh(111) we predicted a novel magnetic phase, a double-row-wise antiferromagnetic (double-row-AFM) structure along the $[11\bar{2}]$ direction.

At first we scanned the magnetic phase space by restricting ourselves to collinear magnetic states, the results of which are outlined in Chapter 4. Performing collinear calculations for the ferromagnetic (FM) and antiferromagnetic (AFM) state, we relaxed our structures using atomic force calculations, and compared the relaxations between both states on both Rh surfaces. We found, all monolayer films are magnetic. The size of the local magnetic moments across the transition-metal series follows Hund's rule with a maximum magnetic moment of 3.77 μ_B for Mn. The largest induced magnetic moment of about 0.46 μ_B was found for Rh atoms adjacent to the Co-film on Rh(001). When relaxations are included, we predict a ferromagnetic ground state for V, Co and Ni, while Cr, Mn and Fe deposited on the Rh(001) substrate favor a $c(2 \times 2)$ antiferromagnetic state, a checkerboard arrangement of up and down magnetic moments. To gain an understanding of the $c(2 \times 2)$ AFM state of Fe/Rh(001), we analyzed this result with respect to the trends of the magnetic order of $3d$ monolayers on other $4d$ substrates, such as Pd(001) and Ag(001). The magnetic anisotropy energies of these ultrathin magnetic films on the Rh(001) are calculated for the FM and the AFM states. With the exception of V and Cr, the easy axis of the magnetization is predicted to be in the film plane. The Rh(111) substrate did not change the magnetic ground state except for Fe, where it changed from AFM on Rh(001) to FM on Rh(111). This change deserved a more detailed analysis which is presented in Chapter 5.

The FM ground state of Fe monolayer on Rh(111) could not be explained from the nonmagnetic density of states and the Stoner model. Total-energy calculations show that the energy difference to the AFM state is rather small and the magnetic structure might be rather subtle. To shed more light onto the magnetism of hexagonal Fe monolayers on (111) oriented $4d$ substrates, and by recalling the fact that the triangular lattice of the hexagonal structure gives rise to topological frustration in case of antiferromagnetic intersite exchange interactions, and thus may cause very complicated magnetic structures, we have extended the search for the magnetic ground state to non-collinear magnetic structures. The results are explained in Chapter 5 and can be summarized as following: The ground state of Fe on Tc(0001) and Fe on Ru(0001) is the 120° Néel structure, Fe monolayers on Rh(111) exhibits a double-RW-AFM state and Fe on Pd and Ag(111) are FM.

In more detail, at first, we performed structural relaxations for the Fe and the first $4d$ metal layer to optimize the Fe-Rh interlayer distance. We performed total-energy calculations to obtain the Fe ground state on Tc, Rh, and Pd substrates within the subspace of collinear magnetic states, and compared our results with previous collinear calculations concerned with the ground state of Fe on Ru, Re, Ir, Pt, Os, to develop a complete picture of the effect of the (111) oriented substrate on the Fe ground state. We found that $4d$-TMs and $5d$-TMs substrates produce similar collinear results for the respective monolayer. Using total-energy differences, we found that the ground state of Fe among the collinearly constraint magnetic phases is ferromagnetic on hexagonal surfaces of fcc substrates (Rh, Pd, Ir, Pt) and row-wise antiferromagnetic (RW-AFM) on hcp substrates (Tc, Ru, Re, Os). For a Fe monolayer on Ru and Rh (Os and Ir) we found, however, only a small total-energy difference between FM and RW-AFM order, which indicates that on these substrates, Fe is very close to a phase transition. From experiments and non-collinear DFT calculations, the Fe monolayer was found to have a Néel ground state on Ru(0001) [57] and a complex magnetic ground state on Ir(111) [27, 28] surfaces. This encouraged us to see what happens to the magnetism of Fe on the Rh(111) substrate by performing non-collinear total-energy calculations of flat spin spirals along the high-symmetry lines $\overline{\Gamma}$-$\overline{\mathrm{K}}$-$\overline{\mathrm{M}}$-$\overline{\Gamma}$ in the hexagonal Brillouin zone. If the nearest neighbor interactions are weak, then higher order interactions may play a crucial role in stabilizing new magnetic ground state of the system, and thus must not be ignored. The calculations prove that this is indeed the case for Fe on Rh(111). For both wavevectors $\mathbf{Q}_{3\overline{\Gamma K}/4}$ and $\mathbf{Q}_{\overline{\mathrm{M}\Gamma}/2}$, the right and left rotating spiral have the same energy and according to the Heisenberg model also the linear superposition of the left and right spiral. DFT calculations show that this is not the case. Instead, from the total-energy difference between the state described by $\mathbf{Q}$ and by a superposition of $\pm\mathbf{Q}$, the higher order interactions are calculated. The superposition of $\pm\mathbf{Q}$ is mapped to real space by a 4-atom unit-cell hosting a double-row-wise (double-RW-AFM) order. Instead of the FM ground state obtained from collinear calculations, we found that the higher order interactions do stabilize an unexpected collinear double-RW-AFM ground state, constructed from $\mathbf{Q}$s along the high-symmetry line $\overline{\mathrm{M}}$-$\overline{\Gamma}$, a structure not considered before.

Due to geometrical effects along the high-symmetry line $\overline{\mathrm{M}}$-$\overline{\Gamma}$, the strongly polarized $4d$ substrate will break the degeneracy of the $\mathbf{Q}_{3\overline{\Gamma K}/4}$ and $\mathbf{Q}_{\overline{\mathrm{M}\Gamma}/2}$ in the Heisenberg model. To capture this effect we extended the Heisenberg model by adding a term which depends on the substrate Stoner parameter and the induced moments of the substrates. The double-RW-AFM structure is unique, as any attempt to find magnetic structures with lower energy such as the triple-row-wise AFM structure failed.

The last chapter, Chapter 6 , of the thesis, describes the analysis of the magnetic properties of Co as two-dimensional monolayer and as single atomic chain on hexagonally terminated $4d$-TMs substrates. Co was selected because of its well-known large magnetic anisotropy in case of other substrates such as Pt. We found that Co, similar to Fe, might change its magnetic state from the FM to the AFM order, if the substrate moves across the $4d$ transition-metal series from late to the early ones. We calculated the magnetocrystalline anisotropy of the FM Co and Fe monolayers on hexaganally terminated $4d$-TMs substrates. We found that the magnetocrystalline anisotropy of Co is much more effected by the presence of the substrate than Fe. As a case of study, the MCA of a Co atomic chain on microfaceted Rh$\langle 111 \rangle$ is analyzed. We compared our results to the previous study of Co chains on Pt$\langle 111 \rangle$ [151], and found that relaxations play a crucial role in order to determine an easy axis of the magnetization consistent with the experimental results, because strong relaxations lead to strong reduction in the Co orbital moments, which influences decisively the direction of the magnetization's easy axis. Including the relaxations we found that the easy axis of the magnetization changes from out-of-plane in case of a monolayer to in-plane for the atomic chain.

Appendix

Heisenberg model on Bravais lattice:

The classical Heisenberg Hamiltonian of two localized spins, $\mathbf{M}_i$ and $\mathbf{M}_j$, on lattice sites i and$j$, can be written as

$$H = \sum_{i,j} -J_{ij}\mathbf{M_i} \cdot \mathbf{M_j} \tag{A-1}$$

with the assumption that the magnetic atoms have spin, with the same magnitude, on all lattice sites

$$\mathbf{M}_i^2 = M^2, \text{ for all } i. \tag{A-2}$$

By using Fourier transforms, it becomes very convenient to express any quantity on a periodic lattice with boundary conditions. Therefore, spins which are localized on N lattice sites can be described by their reciprocal lattice vectors ($\mathbf{q}$) and real space coordinate ($\mathbf{R}_i$) of lattice site i:

$$\mathbf{M}_i = \sum_{\mathbf{q}} \mathbf{M_q} e^{i\mathbf{qR_i}} \tag{A-3}$$

then, the inverse Fourier transform is given by

$$\mathbf{M_q} = \frac{1}{N}\sum_{i} \mathbf{M}_i e^{-i\mathbf{qR_i}} \tag{A-4}$$

Since $\mathbf{M}_i$ is real, then the Fourier components of the spins fulfill the equation

$$\mathbf{M_q} = \mathbf{M_{-q}}^* \tag{A-5}$$

If we replace the real spins $\mathbf{M}_i$ in equation (A-1) by their Fourier components (eq.A-3), the Heisenberg Hamiltonian becomes

$$\begin{aligned} H &= \sum_{i,j} -J_{ij} \sum_{\mathbf{q},\mathbf{q'}} \mathbf{M_q} \cdot \mathbf{M_{q'}} e^{i\mathbf{q}\mathbf{R_i}} e^{i\mathbf{q'}\mathbf{R_j}} \\ &= \sum_{i,j} -J_{ij} \sum_{\mathbf{q},\mathbf{q'}} \mathbf{M_q} \cdot \mathbf{M_{q'}} e^{i(\mathbf{q}+\mathbf{q'})\mathbf{R_i}} e^{i\mathbf{q'}(\mathbf{R_j}-\mathbf{R_i})} \\ &= -N \sum_{\mathbf{q}} \mathbf{M_q} \cdot \mathbf{M_{-q}} \left(\sum_{\delta} J_{0\delta} e^{-i\mathbf{q}\mathbf{R}_\delta} \right) \end{aligned} \tag{A-6}$$

where, the relation $\sum_i e^{i(\mathbf{q}+\mathbf{q'})\mathbf{R_i}} = N\delta_{\mathbf{q},-\mathbf{q'}}$ holds for a sum over all lattice sites, $\mathbf{R}_\delta = \mathbf{R_j} - \mathbf{R_i}$ and the exchange constants are defined to be real quantities with

$$J(\mathbf{q}) = \sum_{\delta} J_{0\delta} e^{-i\mathbf{q}\mathbf{R}_\delta} = J(-\mathbf{q}) = J(\mathbf{q})^* \tag{A-7}$$

then, equation (A-6) will become

$$H = -N \sum_{\mathbf{q}} J(\mathbf{q}) \mathbf{M_q} \cdot \mathbf{M_{-q}} \tag{A-8}$$

Minimizing the energy (eq. A-6) under the condition that all lattice sites have the same spin magnitude (eq. A-2) will lead to determination of the magnetic ground state for N independent equations. This is equivalent to a system of N equations with Fourier spin components

$$\sum_{\mathbf{q}} \mathbf{M_q} \cdot \mathbf{M_{-q}} = M^2 \tag{A-9}$$

and

$$\sum_{\mathbf{q}} \mathbf{M_q} \cdot \mathbf{M_{q'-q}} = 0, \text{ with } \mathbf{q'} \neq 0 \tag{A-10}$$

Which means that all $\mathbf{M_q}$ vanish except for $\mathbf{M_Q}$ and $\mathbf{M_{-Q}}$, where $\pm\mathbf{Q}$ maximize $J(\mathbf{Q})$ and the lowest energy is then given by

$$E = -NM^2 J(\mathbf{Q}) \tag{A-11}$$

The spin structure which corresponds to $\mathbf{M_Q}$ and $\mathbf{M_Q}$ can be covered by introducing the real and imaginary parts, $\mathbf{R_Q}$ and $\mathbf{I_Q}$:

$$\mathbf{M_Q} = \mathbf{R_Q} + i\mathbf{I_Q},\ \mathbf{M_{-Q}} = \mathbf{R_Q} - i\mathbf{I_Q} \tag{A-12}$$

Then, using eq. (A-9) and (A-10), we obtain

$$\mathbf{M_Q} \cdot \mathbf{M_{-Q}} = \mathbf{R_Q^2} + \mathbf{I_Q^2} = M^2 \tag{A-13}$$

$$\mathbf{M_Q} \cdot \mathbf{M_Q} = \mathbf{R_Q^2} - \mathbf{I_Q^2} + 2i\mathbf{R_Q} \cdot \mathbf{I_Q} = 0 \tag{A-14}$$

From equation (A-14), $\mathbf{R_Q}$ and $\mathbf{I_Q}$ are perpendicular ($\mathbf{R_Q} \cdot \mathbf{I_Q} = 0$) and have the same magnitude ($\mathbf{R_Q^2} = \mathbf{I_Q^2} = M^2/2$).

If we now insert eq. (A-12) into eq. (A-3), the spins on the lattice sites can be written in the following form

$$\mathbf{M_i} = 2(\mathbf{R_Q} \cos(\mathbf{Q} \cdot \mathbf{R_i}) - \mathbf{I_Q} \sin(\mathbf{Q} \cdot \mathbf{R_i})) \tag{A-15}$$

which means that the fundamental solution of the Heisenberg model on a Bravais lattice are helical spin structures. Since the spin-orbit coupling terms are not included in the Hamiltonian, the plane can be assumed to be spanned by the two, $\mathbf{R_Q}$ and $\mathbf{I_Q}$, vectors to be the xy-plane. This leads to spin helix rotation around the z-axis in the xy-plane in the direction of $\mathbf{Q}$ and then one can rewrite equation (A-15) for one spin in a matrix form as

$$\begin{aligned} \mathbf{M_i} &= M\{\cos(\mathbf{Q} \cdot \mathbf{R_i}), \sin(\mathbf{Q} \cdot \mathbf{R_i}), 0\} \\ &= M \begin{pmatrix} \cos(\mathbf{Q} \cdot \mathbf{R_i}) \\ \sin(\mathbf{Q} \cdot \mathbf{R_i}) \\ 0 \end{pmatrix} \end{aligned} \tag{A-16}$$

Model Hamiltonian on 2D hexagonal lattice:

The geometry of the two-dimensional hexagonal lattice is shown in fig. 6.8. The real space is presented by the primitive vectors $\mathbf{a}_1$ and $\mathbf{a}_2$ with their reciprocal primitive vectors $\mathbf{b}_1$ and $\mathbf{b}_2$. According to the shown coordination frames, the primitive vectors of the real and reciprocal lattice can be written in terms of Cartesian coordinates:

$$\begin{aligned} \mathbf{a_1} &= a(1,0), \qquad & \mathbf{a_2} = a(\frac{1}{2}, \frac{\sqrt{3}}{2}) \\ \mathbf{b_1} &= \frac{2\pi}{a}(1, \frac{-1}{\sqrt{3}}), \qquad & \mathbf{b_2} = \frac{2\pi}{a}(0, \frac{2}{\sqrt{3}}) \end{aligned} \tag{A-17}$$

where a is the in-plane lattice constant, i.e. the nearest-neighbor distance. Figure 6.8 shows the real and reciprocal two-dimensional hexagonal Bravais lattice, containing the Wigner Seitz cell. The IBZ is limited by the high symmetry lines which connect the symmetry points $\overline{\Gamma}$, $\overline{\mathrm{K}}$ and $\overline{\mathrm{M}}$. A real space spin configuration that correspond to the high symmetry points can be constructed from the knowledge of the two-dimensional BZ. The simplest case to start from is the $\overline{\Gamma}$-point ($\mathbf{q} = \frac{2\pi}{a}(0,0)$), which represent one lattice site in real space ($\mathbf{R} = a(0,0)$). Using equation (A-16), we obtain that the spins on all lattice sites have the same direction ($\mathbf{M}_i = M$). This means that $\overline{\Gamma}$-point corresponds to the ferromagnetic solution. If we choose the $\overline{\mathrm{M}}$-point, we will have six possibilities (Tab. 6.3). As an example

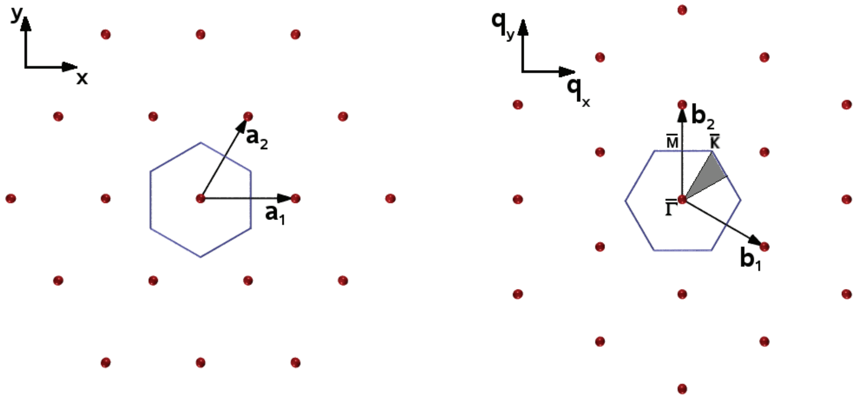

Figure 6.8: The real (left) and reciprocal (right) two-dimensional hexagonal Bravais lattice, containing the Wigner Seitz cell. The IBZ (marked in gray) is limited by the high symmetry lines which connect the symmetry points $\overline{\Gamma}$, $\overline{\mathrm{K}}$ and $\overline{\mathrm{M}}$.

we take the $\mathbf{q} = \frac{2\pi}{a}(0, 1/\sqrt{3})$ point, which corresponds to two real space lattice sites $\mathbf{R_1} = a(1/2, \sqrt{3}/2)$ and $\mathbf{R_2} = a(0, \sqrt{3})$, i. e. nearest neighbor sites will be included. Using equation (A-16), we get $\mathbf{M}_1 = M$ and $\mathbf{M}_2 = -M$ leading to a RW-AFM real space spin structure. In the same procedure, any $\overline{\mathrm{K}}$-point will correspond to three real space spin lattice sites. For example, the point $\mathbf{q} = \frac{2\pi}{a}(\frac{2}{3}, 0)$ corresponds to $\mathbf{R_1} = a(1, 0)$, $\mathbf{R_2} = a(2, 0)$ and $\mathbf{R_3} = a(3, 0)$), then the next nearest neighbor sites are included. Using equation (A-16), we get $\mathbf{M_1} = M\{\cos(\frac{4\pi}{3}), \sin(\frac{4\pi}{3}), 0\}$, $\mathbf{M_2} = M\{\cos(\frac{8\pi}{3}), \sin(\frac{8\pi}{3}), 0\}$ and $\mathbf{M_3} = M\{\cos(\frac{12\pi}{3}), \sin(\frac{12\pi}{3}), 0\}$, which corresponds to the 120° Néel state. All high symmetry points of the two-dimensional hexagonal lattice are presented in Cartesian coordinates in units of $\frac{2\pi}{a}$.

Table 6.3: Cartesian coordinates of the high symmetry points of the two-dimensional hexagonal lattice in units of $2\pi/a$.

symmetry point	coordinates $(\frac{2\pi}{a})$
$\overline{\Gamma}$	$(0, 0)$
$\overline{\mathrm{M}}$	$(0, 1/\sqrt{3}), (0, -1/\sqrt{3})$
	$(1/2, 1/(2\sqrt{3})), (-1/2, -1/(2\sqrt{3}))$
	$(1/2, -1/(2\sqrt{3})), (-1/2, 1/(2\sqrt{3}))$
$\overline{\mathrm{K}}$	$(2/3, 0), (1/3, 1/\sqrt{3}), (1/3, -1/\sqrt{3})$
	$(-2/3, 0), (-1/3, -1/\sqrt{3}), (-1/3, 1/\sqrt{3})$

A linear combination of two or three single-$\mathbf{q}$s will also correspond to a real space spin structure satisfying equation (A-5) on all lattice sites with spin $\mathbf{M_{q_i}} = A\hat{\mathbf{x}} + B\hat{\mathbf{y}} + C\hat{\mathbf{z}}$. Since the product of $\mathbf{Q_i} \cdot \mathbf{R_j}$ is a multiple of π, then $\cos(\mathbf{Q_i} \cdot \mathbf{R_j}) = \pm 1$ and the new spin on the lattice sites j can be written

$$\mathbf{M_j} = \sum_{i,j=1,1}^{3,N} \mathbf{M_{q_i}} \{\cos(q_i \cdot R_j), \sin(q_i \cdot R_j), 0\} \tag{A-18}$$

with $\mathbf{M^2_{q_i}} = M^2$, (A-9) and (A-10) $\mathbf{q} = \frac{2\pi}{a}(0, 1/(2\sqrt{3}))$ and $q = \frac{2\pi}{a}(0, -1/(2\sqrt{3}))$ ($\frac{\overline{\Gamma\mathrm{M}}}{2}$), or $q = \frac{2\pi}{a}(0, 1/(2\sqrt{3}))$ and $q = \frac{2\pi}{a}(0, -1/(2\sqrt{3}))$ ($\frac{3}{4}\overline{\Gamma\mathrm{K}}$), will correspond to four distinct real space lattice sites.

Energetics of the high symmetry states:

The energetics of the magnetic states on the two-dimensional hexagonal lattice can be described within the Heisenberg model, using the Fourier transform of the exchange constants $\mathbf{J}(\mathbf{q})$ according to equation (A-19). This can be done by expanding the vector $\mathbf{q}$ into the primitive vectors of the reciprocal lattice, $\mathbf{q} = q_1\mathbf{b_1} + q_2\mathbf{b_2}$. Then, up to the seventh nearest neighbor, $\mathbf{J}(\mathbf{q})$ can be written as

$$\begin{aligned}
J(\mathbf{q}) \;=\; & -M^2[2J_1[\cos(2\pi q_1) + \cos(2\pi q_2) + \cos(2\pi(q_1 - q_2))] \\
+\; & 2J_2[\cos(2\pi(q_1 + q_2)) + \cos(2\pi(2q_1 - q_2) + \cos(2\pi(-q_1 + 2q_2))] \\
+\; & 2J_3[\cos(4\pi q_1) + \cos(4\pi q_2) + \cos(2\pi(2q_1 - 2q_2))] \\
+\; & 2J_4[\cos(2\pi(3q_1 - q_2)) + \cos(2\pi(2q_1 + q_2)) + \cos(2\pi(3q_1 - 2q_2)) \\
& + \cos(2\pi(q_1 + 2q_2)) + \cos(2\pi(-q_1 + 3q_2)) + \cos(2\pi(2q_1 - 3q_2))] \\
+\; & 2J_5[\cos(6\pi q_1) + \cos(6\pi q_2) + \cos(2\pi(3q_1 - 3q_2))] \\
+\; & 2J_6[\cos(2\pi(2q_1 - 4q_2)) + \cos(2\pi(4q_1 - 2q_2) + \cos(2\pi(2q_1 + 2q_2))] \\
+\; & 2J_7[\cos(2\pi(-q_1 + 4q_2)) + \cos(2\pi(q_1 + 3q_2)) + \cos(2\pi(3q_1 + q_2)) \\
& + \cos(2\pi(4q_1 - q_2)) + \cos(2\pi(4q_1 - 3q_2)) + \cos(2\pi(3q_1 - 4q_2))]
\end{aligned} \tag{A-19}$$

By that one can write the energies of all relevant magnetic states within the Heisenberg model. Along the high symmetry line $\overline{\Gamma}$-$\overline{\mathrm{K}}$-$\overline{\mathrm{M}}$, the $\mathbf{q} = q(\mathbf{b_1} + \frac{1}{2}\mathbf{b_2})$ holds ($q_1 = q$,$q_2 = \frac{1}{2}q$). The $\overline{\Gamma}$-point is at $q = 0$, the $\overline{\mathrm{K}}$-point is at $q = \frac{2}{3}$ and the $\overline{\mathrm{M}}$-point is at $q = 1$. By that one can express the energy along the high symmetry line $\overline{\Gamma}$-$\overline{\mathrm{K}}$-$\overline{\mathrm{M}}$, using eq. (A-19), up to the seventh nearest neighbor exchange constants

$$
\begin{aligned}
E(q) = \quad -M^2(\quad & 2J_2 + 2J_6 \\
& + \cos(\pi q)[4J_1 + 4J_5] \\
& + \cos(2\pi q)[2J_1 + 4(J_3 + B_1 M^2) + 4J_7] \\
& + \cos(3\pi q)[4J_2 + 4J_5] \\
& + \cos(4\pi q)[2(J_3 + B_1 M^2) + 4J_4] \\
& + \cos(5\pi q)[4J_4 + 4J_7] \\
& + \cos(6\pi q)[2J_5 + 4J_6] \\
& + cos(7\pi q)[4J_7])
\end{aligned}
\tag{A-20}
$$

for each $q \in [0, 1]$. On the other hand, the model Hamiltonian along $\overline{\mathrm{M}}$-$\overline{\Gamma}$ differs from what we have in equation. (A-20) since $\mathbf{q} = q(0\mathbf{b_1} + \frac{1}{2}\mathbf{b_2})$. Using eq. (A-19), it will have the following form:

$$
\begin{aligned}
E(q) = \quad -M^2(\quad & 2J_1 + 2(J_3 + B_1 M^2) + 2J_5 \\
& + \cos(\pi q)[4J_1 + 4J_2 + 4J_4 + 4J_7] \\
& + \cos(2\pi q)[2J_2 + 4(J_3 + B_1 M^2) + 4J_4 + 2J_6] \\
& + \cos(3\pi q)[4J_4 + 4J_5 + 4J_7] \\
& + \cos(4\pi q)[2J_6 + 4J_7])
\end{aligned}
\tag{A-21}
$$

for each $q \in \left[1, \frac{\sqrt{3}+1}{\sqrt{3}}\right]$. By that one can write the model Hamiltonian for any q-point on the high symmetry line of the irreducible Berillouin zone. Since double- and multi-Q points will be degenerate with their original single-$\mathbf{Q}$ and equations (A-20) and (A-21) will remain unchanged.

Biquadratic interaction:

The biquadratic interaction Hamiltonian has the form

$$
H_{biq} = -\sum_{ij} B_{ij} (M_i \cdot M_j)^2 \tag{A-22}
$$

and the first order biquadratic constant proportional with the $J_1(\mathbf{q})$ in equation (A-19)

$$
B(\mathbf{q}) = 2B_1(\cos(4\pi q_1) + \cos(4\pi q_2) + \cos(4\pi(q_1 - q_2)) + ... \tag{A-23}
$$

then for the $\overline{\Gamma}$-$\overline{\mathrm{K}}$-$\overline{\mathrm{M}}$ line, it becomes

$$
B(\mathbf{q}) = \cos(2\pi q)\,[4B_1] + \cos(4\pi q)\,[2B_1] \tag{A-24}
$$

and

$$B(\mathbf{q}) = 2B_1(1 + 2\cos(2\pi q)) \tag{A-25}$$

for the $\overline{\mathrm{M}}$-$\overline{\Gamma}$ line. Using equations (A-24) or (A-25), the biquadratic interactions for the high symmetry points are summarized below:

$$\begin{aligned}
E_{\text{biq,FM}} &= -6B_1M^4 \\
E_{\text{biq,RW-AFM}} &= -6B_1M^4 \\
E_{\text{biq,Néel}} &= -\frac{3}{2}B_1M^4 \\
E_{\text{biq,2Q}} &= -2B_1M^4 \\
E_{\text{biq,3Q}} &= -\frac{2}{3}B_1M^4
\end{aligned} \tag{A-26}$$

Then the single-$\mathbf{Q}$ total energy becomes

$$E(\mathbf{q}) = -NM^2(J(\mathbf{q}) - M^2B(\mathbf{q})) \tag{A-27}$$

noting that $M^2B(\mathbf{q})$ is always coupled with J_3 and they can't be decoupled.

The 4–spin interaction:

The 4–spin interaction Hamiltonian, on four lattice sites, has the form

$$H_{4-spin} = -\sum_{ijkl} K_{ijkl}[(M_i \cdot M_j)(M_k \cdot M_l) + (M_j \cdot M_k)(M_l \cdot M_i) - (M_i \cdot M_k)(M_j \cdot M_l)] \tag{A-28}$$

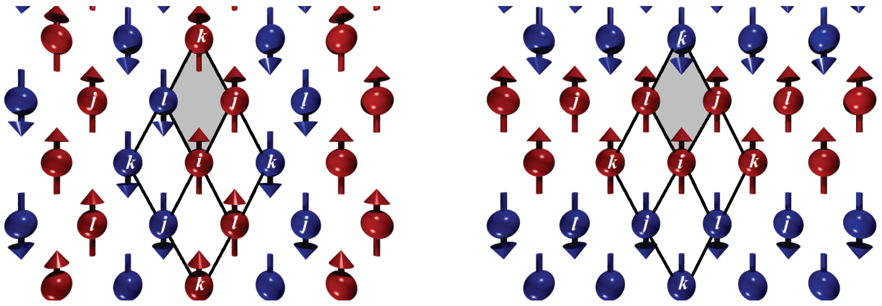

Figure 6.9: Schematic representation of the first order 4–spin interaction, for $2\mathbf{Q}_{\frac{3}{4}\overline{\Gamma K}}$ (left) and $2\mathbf{Q}_{\frac{\overline{M\Gamma}}{2}}$ (right), on $ijkl$ lattice sites. For better view, only four diamonds (out of twelve) are shown, and the related lattice sites, to the total twelve diamonds, are only labeled.

For a 2D hexagonal lattice, the 4–spin interaction represents the interaction between four spins on one diamond. Because there are twelve diamonds surrounding each lattice site; the first order 4–spin interaction will minimize the Hamiltonian by $-12K_1M^4$ for any single-$\mathbf{Q}$ on the high symmetry line.

Using eq. (A-28), one can find that the 4–spin interaction minimizes the Hamiltonian by $-4K_1M^4$ for both double-$\mathbf{Q}$ states, $2\mathbf{Q}_{\frac{3}{4}\overline{\Gamma K}}$ and $2\mathbf{Q}_{\frac{\overline{M\Gamma}}{2}}$ (see Fig. 6.9).

By this, the 4–spin interaction lefts the degeneracy between the single- and double-$\mathbf{Q}$ by $8K_1^4$.

Bibliography

[1] A. J. Freeman and A. Q. Wu. Electronic structure theory of surface, interface and thin-film magnetism. *J. Magn. Magn. Mater*, 100:497, 1991.

[2] T. Asada and G. Bihlmayer and S. Handschuh and S. Heinze and Ph. Kurz and S. Blügel. Magnetism of chromium at surfaces, at interfaces and in thin films. *J. Phys.: Condens. Matter*, 11:9347, 1999.

[3] S. Blügel. Strong ferromagnetism of 3d–metal overlayers on Pd(001). *Europhys. Lett.*, 7:743, 1988.

[4] S. Blügel, M. Weinert and P. H. Dederichs. Ferromagnetism and antiferromagnetism of 3d-metal overlayers on metals. *Phys. Rev. Lett.*, 60:1077, 1988.

[5] S. Blügel and P.H. Dederichs. Ferromagnetism and antiferromagnetism of 3d–metal overlayers on noble metal substrates. *Europhys. Lett.*, 9:597, 1989.

[6] J. E. Ortega and F. J. Himpsel. Inverse photoemission from V, Cr, Mn, Fe, and Co monolayers on Ag(100). *Phys. Rev. B*, 47:16441, 1993.

[7] P. Ferriani, S. Heinze, G. Bihlmayer and S. Blügel. Unexpected trend of magnetic order of 3d transition-metal monolayers on W(001). *Phys. Rev. B*, 72:024452, 2005.

[8] R. Wu and A. J. Freeman. Magnetic properties of Fe overlayers on W(001) and the effects of oxygen adsorption. *Phys. Rev. B*, 45:7532, 1992.

[9] X. Qian and W. Hübner. First-principles calculation of structural and magnetic properties for Fe monolayers and bilayers on W(110). *Phys. Rev. B*, 60:16192, 1999.

[10] D. Spišák and J. Hafner. Diffusion of Fe atoms on W surfaces and Fe/W films and along surface steps. *Phys. Rev. B*, 70:195426, 2004.

[11] A. Kubetzka, P. Ferriani, M. Bode, S. Heinze, G. Bihlmayer, K. von Bergmann, O. Pietzsch, S. Blügel and R. Wiesendanger. Revealing Antiferromagnetic Order of the Fe Monolayer on W(001): Spin-Polarized Scanning Tunneling Microscopy and First-Principles Calculations. *Phys. Rev. Lett.*, 94:087204, 2005.

[12] P. Ferriani, K. von Bergmann, E. Y. Vedmedenko, S. Heinze, M. Bode, M. Heide, G. Bihlmayer, S. Blügel and R. Wiesendanger. Atomic-Scale Spin Spiral with a Unique Rotational Sense: Mn Monolayer on W(001). *Phys. Rev. Lett.*, 101:027201, 2008.

[13] P. Ferriani, K. von Bergmann, E. Y. Vedmedenkoand, S. Heinze, M. Bode, M. Heide, G. Bihlmayer, A. Kubetzka, S. Blügel and R. Wiesendanger. Atomic-Scale Spin Spiral with Unique Rotational Sense: Mn Monolayer on W(001). *Phys. Rev. Lett.*, 102:019901(E), 2009.

[14] P. Ferriani, I. Turek, S. Heinze, G. Bihlmayer and S. Blügel. Magnetic Phase Control in Monolayer Films by Substrate Tuning. *Phys. Rev. Lett.*, 99:187203, 2007.

[15] T. Kachel, W. Gudat, C. Carbone, E. Vescovo, S. Blügel, U. Alkemper, W. Eberhardt. Ferromagnetic order in ultrathin Rh layers on Fe(100). *Phys. Rev. B*, 46:12888, 1992.

[16] G. Shirane, R. Nathans and C. W. Chen. Magnetic Moments and Unpaired Spin Densities in the Fe-Rh Alloys. *Phys. Rev.*, 134:A1547, 1964.

[17] V. L. Moruzzi and P. M. Marcus. Antiferromagnetic-ferromagnetic transition in FeRh. *Phys. Rev. B*, 46:2864, 1992.

[18] K. Nakada and H. Yamada. Fermi surface and antiferromagnetism of FeRh. *Journal of Magnetism and Magnetic Materials*, 310:1046, 2007.

[19] C. Egawa, Y. Tezuka, S. Oki and Y. Murata. Structures of ultra-thin Fe overlayers on a Rh(001) surface. *Surface Science*, 283:338, 1993.

[20] A. M. Begley, S. K. Kim, F. Jona and P. M. Marcus. Low-energy electron diffraction study of the growth of ultrathin films of face-centred cubic Co on Rh(001). *J. Phys.: Condens. Matter*, 5:7307, 1993.

[21] K. Hayashi, M. Sawada, A. Harasawa, A. Kimura and A. Kakizaki. Structure and magnetism of Fe thin films grown on Rh(001) studied by photoelectron spectroscopy. *Phys. Rev. B*, 64:054417, 2001.

[22] K. Hayashi, M. Sawada, H. Yamagami, A. Kimura and A. Kakizaki. Magnetic dead layers induced by strain at fct Fe/Rh(001) interface. *J. Phys. Soc. Japan*, 73:2550, 2004.

[23] K. Hayashi, M. Sawada, H. Yamagami, A. Kimura and A. Kakizaki. Magnetic dead layers in Fe films induced by a lattice mismatch at an interface. *Physica B: Condensed Matter*, 351:324, 2004.

[24] C. Hwang, A. K. Swan and S. C. Hong. Suppression of ferromagnetic order of Fe overlayers on the Rh(001) surface. *Phys. Rev. B*, 60:14429, 1999.

[25] D. Spišák and J. Hafner. Structural, magnetic, and chemical properties of thin Fe films grown on Rh(100) surfaces investigated with density functional theory. *Phys. Rev. B*, 73:155428, 2006.

[26] M. Bode, M. Getzlaff and R. Wiesendanger. Spin-Polarized Vacuum Tunneling into the Exchange-Split Surface State of Gd(0001). *Phys. Rev. Lett.*, 81:4256, 1998.

[27] K. von Bergmann, S. Heinze, M. Bode, G. Bihlmayer, S. Blügel and R. Wiesendanger. Observation of a Complex Nanoscale Magnetic Structure in a Hexagonal Fe Monolayer. *Phys. Rev. Lett.*, 96:167203, 2006.

[28] K. von Bergmann, S. Heinze, M. Bode, G. Bihlmayer, S. Blügel and R. Wiesendanger. Complex magnetism of the Fe monolayer on Ir(111). *New Journal of Physics*, 9:396, 2007.

[29] D. Wortmann, S. Heinze, P. Kurz,, G. Bihlmayer and S. Blügel. Resolving complex atomic-scale spin structures by spin-polarized scanning tunneling microscopy. *Phys. Rev. Lett.*, 86:4132, 2001.

[30] S. Heinze, P. Kurz, D. Wortmann, G. Bihlmayer and S. Blügel. Complex magnetism in ultra-thin films: atomic-scale spin structures and resolution by the spin-polarized scanning tunneling microscope. *Appl. Phys. A*, 75:25, 2002.

[31] Ph. Kurz, G. Bihlmayer, K. Hirai and S. Blügel. Three-Dimensional Spin Structure on a Two-Dimensional Lattice: Mn/Cu(111). *Phys. Rev. Lett.*, 86:1106, 2001.

[32] Y. Tsunoda. Spin-density wave in cubic γ-Fe and γ-$\mathrm{Fe}_{100-x}\mathrm{Co}_x$ precipitates in Cu. *J. Phys.: Condens. Matter*, 1:10427, 1989.

[33] L. Nordström and A. Mavromaras. Magnetic ordering of the heavy rare earths. *Europhys. Lett.*, 49:775, 2000.

[34] O.N. Mryasov, A.N. Lichtenstein, L.M. Sandratskii and V.A. Gubanov. Magnetic structure of FCC iron. *J. Phys. C.:Solid State Phys.*, 3:7683, 1991.

[35] M. Uhl and L.M. Sandratskii and J. Kübler. Electronic and magnetic states of γ-Fe. *J. Magn. Magn. Mater.*, 103:314, 1992.

[36] M. Takahashi. Half-filled Hubbard model at low temperature. *J. Phys. C.:Solid State Phys.*, 10:1289, 1977.

[37] A. H. MacDonald, S. M. Girvin and D. Yoshioka. t/U expansion for the Hubbard model. *Phys. Rev. B*, 37:9756, 1988.

[38] Philipp Kurz. Non-Collinear Magnetism at Surfaces and in Ultrathin Films. *PhD thesis*, 2000.

[39] A. Dallmeyer, C. Carbone, W. Eberhardt, C. Pampuch, O. Rader, W. Gudat, P. Gambardella and K. Kern. Electronic states and magnetism of monatomic *Co* and *Cu* wires. *Phys. Rev. B*, 61:R5133, 2000.

[40] P. Segovia, D. Purdie, M. Hengsberger and Y. Baer. Observation of spin and charge collective modes in one-dimensional metallic chains. *Nature*, 402:504, 1999.

[41] P. Gambardella, A. Dallmeyer, K. Maiti, M. C. Malagoli, W. Eberhardt, K. Kern and C. Carbone. Ferromagnetism in one-dimensional monatomic metal chains. *Nature Mat.*, 416:301, 2002.

[42] P. Gambardella, S. Rusponi, M. Veronese, S. S. Dhesi, C. Grazioli, A. Dallmeyer, I. Cabria, R. Zeller, P. H. Dederichs, K. Kern, C. Carbone and H. Brune. Giant Magnetic Anisotropy of Single Cobalt Atoms and Nanoparticles. *Science*, 300:1130, 2003.

[43] P. Gambardella, A. Dallmeyer, K. Maiti, M.C. Malagoli, S. Rusponi, P. Ohresser, W. Eberhardt, C. Carbone and K. Kern. Oscillatory Magnetic Anisotropy in One-Dimensional Atomic Wires. *Phys. Rev. Lett.*, 93:077203, 2004.

[44] C. Boeglin, S. Stanescu, J. P. Deville, P. Ohresser and N. B. Brookes. In-plane magnetocrystalline anisotropy observed on Fe/Cu(111) nanostructures grown on stepped surfaces. *Phys. Rev. B*, 66:014439, 2002.

[45] P. Ohresser, G. Ghiringhelli, O. Tjernberg, N. B. Brookes and M. Finazzi. Magnetism of nanostructures studied by x-ray magnetic circular dichroism: Fe on Cu(111). *Phys. Rev. B*, 62:5803, 2000.

[46] Ruihua Cheng, S. D. Bader and F. Y. Fradin. Strong magnetic surface anisotropy of ultrathin Fe on curved Pt(111). *Phys. Rev. B*, 77:024404, 2008.

[47] H. A. Dürr, S. S. Dhesi, E. Dudzik, D. Knabben, G. van der Laan, J. B. Goedkoop and F. U. Hillebrecht. Spin and orbital magnetization in self-assembled Co clusters on Au(111). *Phys. Rev. B*, 59:R701, 1999.

[48] Hohenberg, P. and Kohn, W. Inhomogeneous electron gas. *Phys. Rev.*, 136:B864, 1964.

[49] E. Wimmer and H. Krakauer and M. Weinert and A. J. Freeman. Full-potential self-consistent linearized-augmented-plane-wave method for calculating the electronic structure of molecules and surfaces: O_2 molecule. *Phys. Rev. B*, 24:864, 1981.

[50] The Jülich full-linearized augmented plane waves (FLAPW) code family:. `http://www.flapw.de`.

[51] S.H. Vosko and J. P. Perdew. Stoner Model in DFT. *Can. J. Phys.*, 53:1385, 1975.

[52] O. Gunnarsson. Exchange intergral and Stoner Model. *J. Phys. F: Met. Phys.*, 6:587, 1976.

[53] J.F. Janak. Exchange intergral and Stoner Model. *Phys. Rev. B*, 16:255, 1977.

[54] U.K. Poulsen and J. Kollár and O.K. Andersen. Stoner Model in DFT. *J. Phys. F: Met. Phys.*, 6:L241, 1976.

[55] P. Bruno. Tight-binding approach to the orbital magnetic moment and magnetocrystalline anisotropy of transition-metal monolayers. *Phys. Rev. B*, 39:865, 1989.

[56] Ph. Kurz, F. Forster, L. Nordström, G. Bihlmayer and S. Blügel. Ab initio treatment of noncollinear magnets with the full-potential linearized augmented plane wave method. *Phys. Rev. B*, 69:024415, 2004.

[57] Björn Hardrat. Magnetische Ordnung und Austauschwechselwirkung in Fe Monolagen auf hexagonalen Übergangsmetalloberflächen. *Master thesis*, 2008.

[58] E. Schrödinger. An undulatory theory of the mechanics of atoms and molecules. *Phys. Rev.*, **28**:1049, 1926.

[59] L. H. Thomas. The calculation of atomic fields. *Mathematical Proceedings of the Cambridge Philosophical Society*, 23:542, 1927.

[60] E. Fermi. Un metodo statistico per la determinazione di alcune priorieta dell'atome. *Rend. Accad. Naz. Lincei*, 6:602, 1927.

[61] W. Kohn and L. J. Sham. Self-Consistent Equations Including Exchange and Correlation Effects. *Phys. Rev.*, 140:1133, 1965.

[62] U. von. Barth and L. Hedin. A local exchange-correlation potential for the spin polarized case. i. *J. Phys. C.:Solid State Phys.*, 5:1629, 1972.

[63] R. G. Parr and W. Yang. *Density-Functional Theory of Atoms and Molcules.* Oxford University Press, New York, 1989.

[64] P .A .M. Dirac. Note on exchange phenomena in the thomas-fermi atom. *Proc. Cambridge Phil. Roy. Soc.*, 26:376, 1930.

[65] S. H. Vosko, L. Wilk and M. Nusair. Accurate spin-dependent electron liquid correlation energies for local spin density calculations: a critical analysis. *Can. J. Phys.*, 58:1200, 1980.

[66] J. P. Perdew and A. Zunger. Self-interaction correction to density-functional approximations for many-electron systems. *Phys. Rev. B*, 23:5048, 1981.

[67] L. A. Cole and J. P. Perdew. Calculated electron affinities of the elements. *Phys. Rev. A*, 25:1265, 1982.

[68] J. Perdew and Y. Wang. Accurate and simple analytic representation of the electron–gas correlation energy. *Phys. Rev. B*, 45:13244, 1992.

[69] J. Perdew and K. Burke and M. Ernzerhof. Generalized Gradient Approximation Made Simple. *Phys. Rev. Lett.*, 77:3865, 1996.

[70] V. I. Anisimov and F. Aryasetiawan and A. I. Lichtenstein. First-principles calculations of the electronic structure and spectra of strongly correlated systems: the LDA+ U method. *J. Phys.: Condens. Matter*, 9:767, 1997.

[71] C. G. Broyden. A class of methods for solving nonlinear simultaneous equations. *Mathematics of Computation*, 19:577, 1965.

[72] Richard M. Martin. *Eletcronic Structure, Basic Theory and Practical Methods.* Cambridge University Press, Cambridge, 2004.

[73] J. C. Slater. Wavefunction in a periodicd potential. *Phys. Rev.*, 51:864, 1937.

[74] P.W. Atkins. *Molecular Quantum Mechanics.* Oxford University Press, Oxford, 1983.

[75] K. H. Weyrich. Full-potential linear muffin-tin orbital method. *Phys. Rev. B*, 37:10269, 1988.

[76] O.K. Andersen. Linear methods in band theory. *Phys. Rev. B*, 12:3060, 1975.

[77] D. Singh. *Planewaves, Pseudopotentials and the LAPW Method.* Kluwer Academic Publishers, Boston/Dordrecht/London, 1994.

[78] D.R. Hamann. Semiconductor charge densities with hard-core and soft-core pseudopotentials. *Phys. Rev. Lett.*, 212:662, 1979.

[79] H. Krakauer and M. Posternak and A.J. Freeman. Linearized augmented plane-wave method for the electronic band structure of thin films. *Phys. Rev. B*, 19:1706, 1979.

[80] W. Ning and C. Kailai and W. Dingsheng. Work Function of Transition-Metal Surface with Submonolayer Alkali-Metal Coverage. *Phys. Rev. Lett.*, 56:2759, 1986.

[81] D.D. Koelling and B.N. Harmon. A technique for relativistic spin-polarized calculations. *J. Phys. C.:Solid State Phys.*, 10:3107, 1977.

[82] E.M. Rose. *Relativistic Electron Theory.* Wiley, New York, 1961.

[83] C. Herring. *Magnetism.* edited by G. Rado and H. Suhl, Academic, New York, 1966.

[84] N.W. Ashcroft and N.D. Mermin. *Solid State Physics.* Holt-Saunders Japan LTD., 1976.

[85] Mathias Getzlaff. *Fundamentals of Magnetism.* Springer, 2007.

[86] S. Blügel and G. Bihlmayer. *Handbook of Magnetism and Advanced Magnetic Materials*, page Magnetism of Low Dimensions: Theory. Ed. H. Kronmüller and S. Parkin, J. Wiley & Sons, Ltd, 2007.

[87] K. Terakura and N. Hamada and T. Oguchi and T. Asada. Local and non-local spin susceptibilities of transition metals. *J. Phys. F: Met. Phys.*, 12:1661, 1982.

[88] W. Brinkman and R. Elliot. Theory of spin-space groups. *Proc. R. Soc. A*, 294:343, 1966.

[89] J. Kübler, K.H. Höck, J. Sticht and A.R. Williams. Density functional theory of non-collinear magnetism. *J. Phys. F: Met. Phys.*, 18:469, 1988.

[90] L.M. Sandratskii and P.G. Guletskii. Energy band structure of bcc iron at finite temperatures. *J. Magn. Magn. Mater.*, 79:306, 1989.

[91] J. Sticht, K.H. Höck and J. Kübler. Non-collinear itinerat magnetism: the case of Mn_3Sn. *J. Phys.: Condens. Matter*, 1:8155, 1989.

[92] L.M. Sandratskii. Symmetry analysis of electronic states for crystals with spiral magnetic order. I. general properties. *JPCM*, 3:8565, 1991.

[93] H. J. G. Draaisma and W. J. M. Jonge. Surface and volume anisotropy from dipoledipole interactions in ultrathin ferromagnetic films. *J. Appl. Phys.*, 64:3610, 1988.

[94] I. V. Solovyev, A. I. Liechtenstein and K. Terakura. Is hund's second rule responsible for the orbital magnetism in solids? *Phys. Rev. Lett.*, 80:5758, 1988.

[95] O. Eriksson, M. S. S. Brooks and B. Johansson. Orbital polarization in narrow-band systems: Application to volume collapses in light lanthanides. *PRB*, 41:7311, 1991.

[96] L.M. Sandratskii. Noncollinear magnetism in itinerant-electron systems: theory and application. *Advances in Physics*, 47:91, 1998.

[97] L.M. Sandratskii. Energy band structure calculations for crystals with spiral magnetic structure. *Phys. Status Solidi B*, 136:167, 1986.

[98] L.M. Sandratskii and P.G. Guletskii. Symmetrised method for the calculation of the band structure of noncollinear magnets. *J. Phys. F: Met. Phys.*, 16:L43, 1986.

[99] J. Kübler, K.H. Höck, J. Sticht and A.R. Williams. Local spin-density functional theory of noncollinear magnetism. *J. Appl. Phys.*, 63:3482, 1988.

[100] O.N. Mryasov, A.I. Lichtenstein, L.M. Sandratskii and V.A. Gubanov. Spiral-spin-density-wave states in fcc iron: Linear-muffin-tin-orbital band-structure approach. *Phys. Rev. B*, 45:12330, 1992.

[101] L. Nordström and D.J. Singh. Noncollinear intra-atomic magnetism. *Phys. Rev. Lett.*, 76:4420, 1996.

[102] J. Topping. On the mutual potential energy of a plane network of doublets. *Proc. R. Soc. A*, A 114:67, 1927.

[103] L. Szunyogh, B. Újfalussy, P. Weinberger. Magnetic anisotropy of iron multilayers in Au(001): First-principles calculations in terms of the fully relativistic spin-polarized screened KKR method. *Phys. Rev. B*, 51:9552, 1995.

[104] P. P. Ewald. Die berechnung optischer und elektrostatischer gitterpotentiale. *Ann. Physik*, 64:253, 1921.

[105] G. van der Laan. Microscopic origin of magnetocrystalline anisotropy in transition metal thin films. *J. Phys.: Condens. Matter*, 10:3239, 1998.

[106] M. S. S. Brooks. Calculated ground state properties of light actinide metals and their compounds. *Physica B*, 130:6, 1985.

[107] I. V. Solovyev. Orbital polarization in itinerant magnets. *Phys. Rev. Lett.*, 95:267205, 2005.

[108] O. Hjortstam, J. Trygg, J. M. Wills, B. Johansson and O. Eriksson. Calculated spin and orbital moments in the surfaces of the 3d metals Fe, Co, and Ni and their overlayers on Cu(001). *Phys. Rev. B*, 53:9204, 1996.

[109] B. Nonas, I. Cabria, R. Zeller, P. .H. Dederichs, T. Huhne and H. Ebert. Strongly Enhanced Orbital Moments and Anisotropies of Adatoms on the Ag(001) Surface. *Phys. Rev. Lett.*, 86:2146, 2001.

[110] J. Stöhr. Exploring the microscopic origin of of magnetic anisotropies with X-ray magnetic circular dichroism XMCD. *J. Magn. Magn. Mater.*, 200:470, 1999.

[111] N. M. Rosengaard and B. Johansson. Finite-temperature study of itinerant ferromagnetism in Fe, Co, and Ni. *Phys. Rev. B*, 55:14975, 1997.

[112] S. V. Halilov, H. Eschrig, A. Y Perlov and P. M. Oppeneer. Adiabatic spin dynamics from spin-density-functional theory: Application to Fe, Co, and Ni. *Phys. Rev. B*, 58:293–302, 1998.

[113] A. I. Liechtenstein, M. I. Katsnelson, V. P. Antropov and V. A. Gubanov. Local spin density functional approach to the theory of exchange interactions in ferromagnetic metals and alloys. *J. Magn. Magn. Mater.*, 67:65, 1987.

[114] M. Pajda, J. Kudrnovský, I. Turek, V. Drchal and P. Bruno. Ab initio calculations of exchange interactions, spin-wave stiffness constants, and Curie temperatures of Fe, Co, and Ni. *Phys. Rev. B*, 64:174402, 2001.

[115] N. D. Mermin and H. Wagner. Absence of Ferromagnetism or Antiferromagnetism in One- or Two-Dimensional Isotropic Heisenberg Models. *Phys. Rev. Lett.*, 17:1133, 1966.

[116] Herbert B. Callen. Green Function Theory of Ferromagnetism. *Phys. Rev.*, 130:890, 1963.

[117] R. P. Erickson and D. L. Mills. Anisotropy-driven long-range order in ultrathin ferromagnetic films. *Phys. Rev. B*, 43:11527, 1991.

[118] Peter Mohn. *Magnetism in the solid state.* Springer, 2006.

[119] X. L. Nie, S. Heinze, G. Bihlmayer and S. Blügel. Ferromagntism and antiferromagnetism of 3*d* transtion metal monolayers on w(110). 2007.

[120] Dwight E. Gray, Coordinating editor. *American Institute of Physics handbook.* Mcgraw-Hill (Tx), New York, 1972.

[121] W. Oed, B. Dötsch, L. Hammer, K. Heinz and K. Müller. A LEED investigation of clean and oxygen covered Rh(100). *Surface Science*, 207:55, 1988.

[122] A. M. Begley, S. K. Kim, F. Jona and P. M. Marcus. Surface relaxation of Rh(001). *Phys. Rev. B*, 48:12326, 1993.

[123] M. Methfessel, D. Hennig and M. Scheffler. Trends of the surface relaxations, surface energies, and work functions of the 4d transition metals. *Phys. Rev. B*, 46:4816, 1992.

[124] S. Handschuh and S. Blügel. Magnetic exchange coupling of 3d metal monolayers on Fe(001). *Solid State Commun.*, 10:633, 1998.

[125] C. Rau, C. Liu, A. Schmalzbauer, and G. Xing. Ferromagnetic order at (100) $p(1\times1)$ surfaces of bulk paramagnetic vanadium. *Phys. Rev. Lett.*, 57:2311, 1986.

[126] C. Rau, G. Xing and M. Robert. Ferromagnetic order and critical behavior at surfaces of ultrathin V(100) p(1×1) films on Ag(100). *J. of Vac. Sci. & Tech. A*, 6:579, 1988.

[127] M. Stampanoni and A. Vaterlaus and D. Pescia and M. Aeschlimann and F. Meier and W. Dürr and S. Blügel. Lack of evidence for ferromagnetism in the vanadium monolayer on Ag(001). *Phys. Rev. B*, 37:10380, 1988.

[128] M. Weinert, R. E. Watson and J. W. Davenport. Total-energy differences and eigenvalue sums. *Phys. Rev. B*, 32:2115, 1985.

[129] R. Wu, L. Chen and A. J. Freeman. First principles determination of magnetostriction in bulk transition metals and thin films. *J. Magn. Magn. Mater.*, 170:103, 1997.

[130] O. Le Bacq, O. Eriksson, B. Johansson, P. James and A. Delin. First-principles calculations of the magnetic anisotropy energy of Fe-V multilayers. *Phys. Rev. B*, 65:134430, 2002.

[131] L. M. Sandratskii, E. Şaşioğlu and P. Bruno. Exchange interactions and Néel temperature of a Fe monolayer on W(001): A first-principles study. *Phys. Rev. B*, 73:014430, 2006.

[132] M. Bode, M. Heide, K. von Bergmann, P. Ferriani, S. Heinze, G. Bihlmayer, A. Kubetzka, O. Pietzsch, S. Blügel and R. Wiesendanger. Chiral magnetic order at surfaces driven by inversion asymmetry. *Nature Mat.*, 6:813, 2007.

[133] M. Albrecht; M. Maret, J. Köhler, B. Gilles, R. Poinsot,J. L. Hazemann, J. M. Tonnerre, C. Teodorescu and E. Bucher. Weak ferromagnetism of Cr films on Ru(0001). *Phys. Rev. Lett.*, 85:5344, 2000.

[134] F. El Gabaly, S. Gallego, C. Muñoz, L. Szunyogh, P. Weinberger, C. Klein, A. K. Schmid, K. F. McCarty and J. de la Figuera. Spin reorientation for Co films on Ru(0001). *Phys. Rev. Lett.*, 96:147202, 2006.

[135] C. Liu and S. D. Bader. Magnetism of thin Fe films on Ru(0001). *Phys. Rev. B*, 41:553, 1990.

[136] S. , M. Piecuch and J. F. Bobo. Growth and magnetism of Fe films on Ru(0001) and Ir(111). *Phys. Rev. B*, 46:4909, 1992.

[137] D. Repetto, T. Y. Lee, S. Rusponi, J. Honolka, K. Kuhnke, V. Sessi, U. Starke, H. Brune, P. Gambardella, C. Carbone, A. Enders and K. Kern. Growth of Fe films on Pt(111). *Phys. Rev. B*, 74:054408, 2006.

[138] Y. Zhang and W. Yang. Comment on "Generalized Gradient Approximation Made Simple". *Phys. Rev. Lett.*, 80:890, 1998.

[139] E. Bauer. Growth of thin films. *J. Phys.: Condens. Matter*, 11:9365, 1999.

[140] D. Tian, H. Li, F. Jona and P. M. Marcus. Study of the growth of Fe on Ru(0001) by low-energy electron diffraction. *Solid State Commun.*, 80:783, 1991.

[141] G. Bihmayer, M. Heide and S. Blügel. Magnetism in low dimentional overlayers, wires and adatoms. *Poster*, 2000.

[142] G. H. Wannier. Antiferromagnetism. The Triangular Ising Net. *Phys. Rev.*, 79:357, 1950.

[143] D. H. Lee, J. D. Joannopoulos, J. W. Negele and D. P. Landau. Symmetry analysis and monte carlo study of a frustrated antiferromagnetic planar (XY) model in two dimensions. *Phys. Rev. B*, 33:450, 1986.

[144] M. F. Collins and O. A. Petrenko. Triangular antiferromagnets. *Can. J. Phys.*, 75:605, 1997.

[145] H. Kawamura. Universality of phase transitions of frustrated antiferromagnets. *J. Phys.: Condens. Matter*, 10:4707, 1998.

[146] L. Capriotti, A. E. Trumper and S. Sorella. Long-range Néel order in the triangular heisenberg model. *Phys. Rev. Lett.*, 82:3899, 1999.

[147] L. Capriotti, A. Cuccoli, V. Tognetti, P. Verrucchi and R. Vaia. Thermodynamics of the quantum easy-plane antiferromagnet on the triangular lattice. *Phys. Rev. B*, 60:7299, 1999.

[148] L. Nordheim. The electron theory of metals. *Ann. Phys.* , 9:607, 1931.

[149] M. Ležaić, Ph. Mavropoulos, J. Enkovaara, G. Bihlmayer and S. Blügel. Thermal Collapse of Spin Polarization in Half-Metallic Ferromagnets. *Phys. Rev. Lett.*, 97:026404, 2006.

[150] Private discussion with Dr. G. Bihlmayer (2009).

[151] S. Baud, Ch. Ramseyer, G. Bihlmayer and S. Blügel. Relaxation effects on the magnetism of decorated step edges: Co/Pt(664). *Phys. Rev. B*, 73:104427, 2006.

[152] M. Körling and J. Häglund. Cohesive and electronic properties of transition metals: The generalized gradient approximation. *Phys. Rev. B*, 45:13293, 1992.

[153] M. Körling and J. Ergon. Gradient-corrected ab initio calculations of spin-spiral states in fcc-Fe and the effects of the atomic-spheres approximation. *Phys. Rev. B*, 54:R8293, 1996.

[154] G. Moulas, A. Lehnert, S. Rusponi, J. Zabloudil, C. Etz, S. Ouazi, M. Etzkorn, P. Bencok, P. Gambardella, P. Weinberger and H. Brune. High magnetic moments and anisotropies for Fe_xCo_{1-x} monolayers on Pt(111). *Phys. Rev. B*, 78:214424, 2008.

[155] Fermi national accelerator laboratory (USA). Magnetic susceptibility of the elements and inorganic compunds. `http://www-d0.fnal.gov/hardware/cal/lvps_info/engineering/elementmagn.pdf`.

[156] T. Loucks. *Augmented Plane Wave Method.* Benjamin, New York, 1967.

[157] J. Stöhr. *Numerische Mathematik 1.* Springer-Verlag, Berlin, 1994.

[158] J.C. Slater. *Advances in Quantum Chemistry,* 1:35, 1964.

[159] D. Liberman and J.T. Waber and D.T. Cramer. *Phys. Rev.*, 137:A27, 1965.

[160] P. M. Marcus. Variational methods in the computation of energy bands. *Int. J. Quantum Chem. Suppl.*, 1:567, 1967.

[161] O. Jepsen and O.K. Andersen. The electronic structure of h.c.p. Ytterbium. *Solid State Commun.*, 9:1763, 1971.

[162] D.J. Chadi and Marvin L. Cohen. Special points in the brillouin zone. *Phys. Rev. B*, 8:5747, 1973.

[163] R.V. Kasowski. Band Structure of NiS as Calculated Using a Simplified Linear-Combination-of-Muffin-Tin-Orbitals Method. *Phys. Rev. B*, 8:1378, 1973.

[164] S.L. Cunningham. Special k-points in 2 Dimensions. *Phys. Rev. B*, 10:4988, 1974.

[165] D.D. Koelling and G.O. Arbman. Use of energy derivative of the radial solution in an augmented plane wave method: application to copper. *J. Phys. F: Met. Phys.*, 5:2041, 1975.

[166] S.P. Singhal. Dielectric matrix for aluminum. *Phys. Rev. B*, 12:564, 1975.

[167] A. J. Appelbaum and D. R. Hamann. The electronic structure of solid surfaces. *Rev. Mod. Phys.*, 48:479, 1976.

[168] T. Takeda. The scalar relativistic approximation. *Z. Physik. B*, 32:43, 1978.

[169] J.H. Wood and A.M. Boring. Improved pauli hamiltonian for local-potential problems. *Phys. Rev. B*, 18:2701, 1978.

[170] H. Gollisch and L. Fritsche. Relativistic one-particle equation for electron states of heavy metals. *Phys. Stat. sol(b)*, 86:145, 1978.

[171] M. Weinert. Solution of Poisson's equation: beyond Ewald-type methods. *J. Math. Phys.*, 22:2433, 1981.

[172] M. Weinert and E. Wimmer and A.J. Freeman. Total-energy all-electron density functional method for bulk solids and surfaces. *Phys. Rev. B*, 26:4571, 1982.

[173] R. Feder and F. Rosicky and B. Ackermann. Relativistic multiple scattering theory of electrons by ferromagnets. *Z. Physik. B*, 52:31, 1983.

[174] R. Feder and F. Rosicky and B. Ackermann. Relativistic multiple scattering theory of electrons by ferromagnets (erratum). *Z. Physik. B*, 53:244, 1983.

[175] G.A. Benesh and J.E. Inglesfield. Green s-function FLAPW. *J. Phys. C.:Solid State Phys.*, 17:1595, 1984.

[176] D. Singh. Simultaneous solution of diagonalization and self–consistency problems for transition–metal systems. *Phys. Rev. B*, 40:5428, 1989.

[177] G.W. Fernando. Iterative approaches to electronic structure with augmented bases. *Phys. Rev. B*, 41:903, 1990.

[178] J.M. Soler and A.R. Williams. Forces in APW. *Phys. Rev. B*, 42:9728, 1990.

[179] R. Yu and D. Singh and H. Krakauer. All-electron and pseudopotential force calculations using the linearized-augmented-plane-wave method. *Phys. Rev. B*, 43:6411, 1991.

[180] R. Wu and A.J. Freeman. An efficient step–forward way to solve the Schrödinger eigenvalue equation in self–consistent calculations. *Comput. Phys. Commun.*, 76:58, 1993.

[181] A.B. Shick and V. Drchal and J. Kudrnovský and P. Weinberger. Electronic structure and magnetic properties of random alloys: fully relativistic spin-polarized linear muffin-tin-orbital method. *Phys. Rev. B*, 54:1610, 1996.

[182] R. Richter, J. G. Gay and J. R. Smith. Spin separation in a metal overlayer. *Phys. Rev. Lett.*, 54:2704, 1985.

[183] B. T. Jonker, K. H. Walker, E. Kisker, G .A. Prinz and C. Carbone. Spin-polarized photoemission study of epitaxial Fe(001) films on Ag(001). *Phys. Rev. Lett.*, 57:142, 1986.

[184] B. Heinrich, K. B. Urquhart, A. S. Arrott, J. F. Cochran, K. Myrtle and S. T. Purcell. Ferromagnetic-resonance study of ultrathin bcc Fe(100) films grown epitaxially on fcc Ag(100) substrates. *Phys. Rev. Lett.*, 59:1756, 1987.

[185] N. C. Koon, B. T. Jonker, F. A. Volkening, J. J. Krebs and G. A. Prinz. Direct Evidence for Perpendicular Spin Orientations and Enhanced Hyperfine Fields in Ultrathin Fe(100) Films on Ag(100). *Phys. Rev. Lett.*, 59:2463, 1987.

[186] M. Stampanoni, A. Vaterlaus, M. Aeschlimann and F. Meier. Magnetism of epitaxial bcc iron on Ag(001) observed by spin-polarized photoemission. *Phys. Rev. Lett.*, 59:2483, 1987.

[187] W. Drube and F .J. Himpsel. Minority-spin states for V and Mn on Ag(111) by inverse photoemission. *Phys. Rev. B*, 35:4131, 1987.

[188] S. D. Bader and E. R. Moog. Magnetic properties of novel epitaxial films. *J. Appl. Phys.*, 61:3729, 1987.

[189] T. Beier, D. Pescia, M. Stampanoni, A. Vaterlaus and F. Meier. Ground state magnetic properties of ultrathin fcc Fe and Co films on Cu(001) surfaces. *Appl. Phys. A*, 47:73, 1988.

[190] R. Germar, W. Dürr, J. W. Krewer, D. Pescia1 and W. Gudat. Layer-by-layer growth of metal overlayers. *Appl. Phys. A*, 47:393, 1988.

[191] R. F. Willis, J. A. C. Bland, and W. Schwarzacher. Ferromagnetism in ultrathin metastable films of fcc Fe, Co, and Ni. *J. Appl. Phys.*, 63:4051, 1988.

[192] J. P. Perdew and K. Burke and M. Ernzerhof. Generalized Gradient Approximation Made Simple. *Phys. Rev. Lett.*, 77:3865, 1996.

[193] J. S. Kouvel and C. C. Hartellius. Fermi surface and antiferromagnetism of FeRh. *J. Appl. Phys.*, 33:1343, 1962.

[194] Cho, Jun-Hyung and Scheffler, Matthias . Surface Relaxation and Ferromagnetism of Rh(001). *Phys. Rev. Lett.*, 78:1299, 1997.

[195] J.F. Janak and A. R. Williams. Giant internal magnetic pressure and compressibility anomalies. *Phys. Rev. B*, 14:4199, 1976.

[196] O. K. Andersen, J. Madsen, U. K. Poulsen, O. Jepsen and J. Kollár. Magnetic ground state properties of transition metals. *Physica B+C*, 86-88:249, 1977.

[197] Masao Shimizu. Forced Magnetostriction, Magnetic Contributions to Bulk Modulus and Thermal Expansion and Pressure Dependence of Curie Temperature in Iron, Cobalt and Nickel. *J. Phys. Soc. Japan*, 44:792, 1978.

[198] C. Chappert, A. Fert and F. Nguyen van Dau. The emergence of spin electronics in data storage. *Nature Mat.*, 6:813, 2007.

[199] C. F. Hirjibehedin, C. P. Lutz and A. J. Heinrich. Spin coupling in engineered atomic structures. *Science*, 312:1021, 2006.

[200] S. Lounis, P. H. Dederichs and S. Blügel. Magnetism of Nanowires Driven by Novel Even-Odd Effects. *Phys. Rev. Lett.*, 101:107204, 2008.

[201] J. Honolka, K. Kuhnke, L. Vitali, A. Enders, K. Kern, S. Gardonio, C. Carbone, S. R. Krishnakumar, P. Bencok, S. Stepanow and P. Gambardella. Absence of local magnetic moments in Ru and Rh impurities and clusters on Ag(100) and Pt(997). *Phys. Rev. B*, 76:144412, 2007.

[202] N. Néel, J. Kröger, R. Berndt, T. O. Wehling, A. I. Lichtenstein, and M. I. Katsnelson. Controlling the Kondo Effect in CoCuN Clusters Atom by Atom. *Phys. Rev. Lett.*, 101:266803, 2008.

[203] C. Iacovita, M. V. Rastei, B. W. Heinrich, T. Brumme, J. Kortus, L. Limot, and J. P. Bucher. Visualizing the spin of individual cobalt-phthalocyanine molecules. *Phys. Rev. Lett.*, 101:116602, 2008.

[204] T. Asada and S. Blügel. Total Energy Spectra of Complete Sets of Magnetic States for fcc-Fe Films on Cu(100). *Phys. Rev. Lett.*, 79:507, 1997.

[205] P. E. A. Turchi, A. Gonis, V. Drchal and J. Kudrnovsky. First-principles study of stability and local order in substitutional Ta-W alloys. *Phys. Rev. B*, 64:085112, 2001.

[206] H. E. Hoster, A. Bergbreiter, P. M. Erne, T. Hager, H. Rauscher and R. J. Behm. $\mathrm{Pt}_x\mathrm{Ru}_{1-x}$/Ru(0001) surface alloys-formation and atom distribution. *Phys. Chem. Chem. Phys.*, 10:3812, 2008.

[207] B. N. Engel, M. H. Wiedmann, A. R. Van Leeuwen and Ch. M. Falco. Anomalous magnetic anisotropy in ultrathin transition metals. *Phys. Rev. B*, 48:9894, 1993.

[208] B. Voigtländer, G. Meyera and Nabil M. Amer. Epitaxial growth of Fe on Au(111): a scanning tunneling microscopy investigation. *Surface Science*, 255:L529, 1991.

[209] G. Lugert, W. Robl, L. Pfau, M. Brockmann and G. Bayreuther. Magnetic anisotropy and film structure in ultrathin Fe films on Au(111). *J. Magn. Magn. Mater.*, 121:498, 1993.

[210] F. J. A. den Broeder, D. Kuiper, H. C. Donkersloot and W. Hoving. A comparison of the magnetic anisotropy of [001] and [111] oriented Co/Pd Multilayers. *Appl. Phys. A*, 49:507, 2004.

Acknowledgement

I don't know how to describe my happiness of finishing my PhD successfully at one of the most outstanding highly equipped worldwide research centers. Additionally, being graduated from one of the highest ranked German Universities, the RWTH-Aachen University, I would say, the one who I owe for such great success in my life is my supervisor Prof. Dr. Stefan Blügel. Apart from accepting me to be one of his students, he always was very helpful, open minded, smiling, and most important full of scientific thoughts and ideas, which I learned from and helped me to have good progress during my PhD. In the name of my family, I would like to thank also his wife for her nice gifts she presented to our little daughter.

I can't forget my dear advisor, Dr. Gustav Bihlmayer, who was never busy when I needed his help! I learned many things from his fruitful discussions. Dear Gustav, please forgive me for being disturbed by correcting my PhD thesis during the nice time with your Family in Spain! You are really amazing!

I would like also to acknowledge Dr. Daniel Wortmann, who was the first one I shared office with when I came to Jülich. He was always helpful during the time learning how to use the FLEUR code. I like his smiley face and opened chest, and most important is his nice way of simplifying the problems.

JProf. Dr. Stefan Heinze and Dr. Paolo Ferriani for the nice collaborations we had.

My X and current PhD students colleagues: Simon Woodford, Manfred Niesert, Markus Betzinger, Alexander Thieß, Martin Schlipf, Andreas Dolfen, Andreas Gierlich and Björn Hardrat from Hamburg University: I really was very happy to know you guys, I really had fun with all of you and enjoyed of being your colleague in the same group! Björn: it was nice collaborations we had since we published one famous Ironic article out of that!

Postdocs and Scientific staff: Samir, thanks for the povray file! Predrag: thanks for the vtk, Python, and of course the chocolates and biscuit I always finished! Marcus Heide: thanks for your help of finding strange complex structure on the high symmetry line! Ersoy: Thank you very much for your guide to read nice books in physics. Marjana, Phivos and Yuriy you are really very nice team who I like. Nicolae: try to minimize washing your eyes, we need them for the next Science paper!

I acknowledge our great secretary "Mrs Ute Winkler" who (I don't know how) could and still can manage all the above mentioned people plus the other members of our large group' official stuff! You are really great Ute!

The last, but most one, who I would like to thank is my dear mother for her prayers and patience for being alone till I finish the task I came for. I also thank my lovely wife, who really helped me during my PhD study with her warm feelings and support.

Schriften des Forschungszentrums Jülich
Reihe Schlüsseltechnologien / Key Technologies

1. **Soft Matter**
   From Synthetic to Biological Materials
   Lecture manuscripts of the 39th IFF Spring School March 3 – 14, 2008
   Jülich, Germany
   edited by J.K.G. Dhont, G. Gompper, G. Nägele, D. Richter, R.G. Winkler (2008), c. 1000 pages
   ISBN: 978-3-89336-517-3

2. **Structural analysis of diblock copolymer nanotemplates using grazing incidence scattering**
   by D. Korolkov (2008), III, 167 pages
   ISBN: 978-3-89336-522-7

3. **Thermal Nonequilibrium**
   Thermal forces in fluid mixtures
   Lecture Notes of the 8th International Meeting on Thermodiffusion,
   9 – 13 June 2008, Bonn, Germany
   edited by S. Wiegand, W. Köhler (2008), 300 pages
   ISBN: 978-3-89336-523-4

4. **Synthesis of CMR manganites and ordering phenomena in complex transition metal oxides**
   by H. Li (2008), IV, 176 pages
   ISBN: 978-3-89336-527-2

5. **Neutron Scattering**
   Lectures of the JCNS Laboratory Course held at the Forschungszentrum Jülich and the research reactor FRM II of TU Munich
   edited by R. Zorn, Th. Brückel, D. Richter (2008), ca. 500 pages
   ISBN: 978-3-89336-532-6

6. **Ultrafast Magnetization Dynamics**
   by S. Woodford (2008), 130 pages
   ISBN: 978-3-89336-536-4

7. **Role of Surface Roughness inTribology: from Atomic to Macroscopic Scale**
   by C. Yang (2008), VII, 166 pages
   ISBN: 978-3-89336-537-1

8. **Strahl- und Spindynamik von Hadronenstrahlen in Mittelenergie-Ringbeschleunigern**
   von A. Lehrach (2008), II, 171 Seiten
   ISBN: 978-3-89336-548-7

9. **Phase Behaviour of Proteins and Colloid-Polymer Mixtures**
   by C. Gögelein (2008), II, 147 pages
   ISBN: 978-3-89336-555-5

10. **Spintronics – From GMR to Quantum Information**
    Lecture Notes of the 40th IFF Spring School March 9 – 20, 2009
    Jülich, Germany
    edited by St. Blügel, D. Bürgler, M. Morgenstern, C. M. Schneider,
    R. Waser (2009), c. 1000 pages
    ISBN: 978-3-89336-559-3

11. **ANKE / PAX Workshop on SPIN Physics**
    JINR, Dubna, Russia / June 22. – 26, 2009
    Org. Committee: A. Kacharava, V. Komarov, A. Kulikov, P. Lenisa, R. Rathmann,
    H. Ströher (2009), CD-ROM
    ISBN: 978-3-89336-586-9

12. **Entwicklung einer Nanotechnologie-Plattform für die Herstellung Crossbar-basierter Speicherarchitekturen**
    von M. Meier (2009), 135 Seiten
    ISBN: 978-3-89336-598-2

13. **Electronic Oxides –**
    Correlation Phenomena, Exotic Phases and Novel Functionalities
    Lecture Notes of the 41st IFF Spring School March 8 – 19, 2010
    Jülich, Germany
    edited by St. Blügel, T. Brückel, R. Waser, C.M. Schneider (2010), ca. 1000 pages
    ISBN: 978-3-89336-609-5

14. **4th Georgian-German School and Workshop in Basic Science**
    Tbilisi, Georgia / May 3 – 7, 2010
    Org. Committee: E. Abrosimova, R. Botchorishvili, A. Kacharava, M. Nioradze,
    A. Prangishvili, H. Ströher (2010); CD-ROM
    ISBN: 978-3-89336-629-3

15. **Neutron Scattering**
    Lectures of the JCNS Laboratory Course held at Forschungszentrum Jülich and the research reactor FRM II of TU Munich
    edited by Th. Brückel, G. Heger, D. Richter, G. Roth and R. Zorn (2010),
    ca 350 pages
    ISBN: 978-3-89336-635-4

16. **Ab *initio* investigations of magnetic properties of ultrathin transition-metal films on *4d* substrates**
    by A. Al-Zubi (2010), II, 143 pages
    ISBN: 978-3-89336-641-5

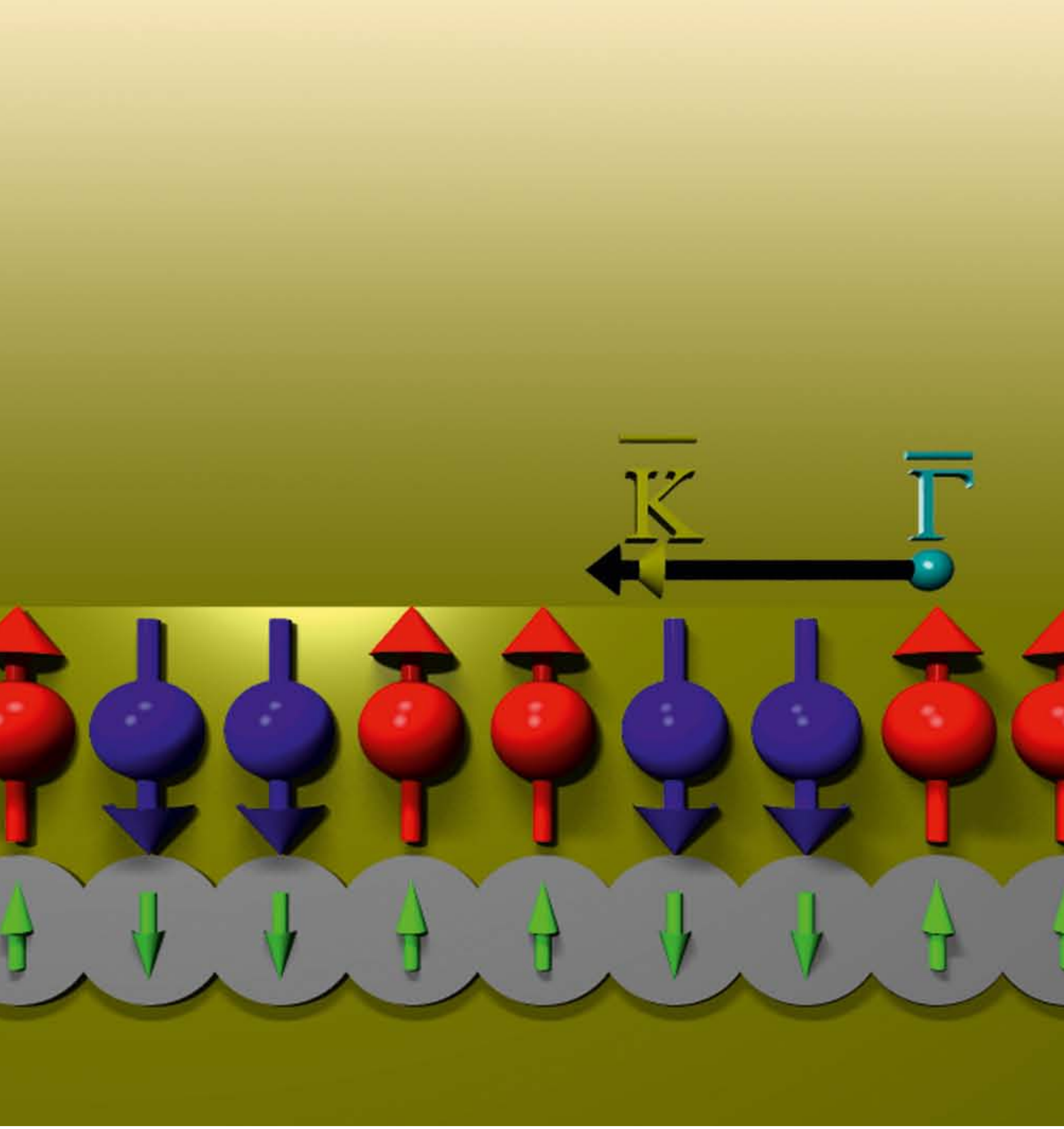

Schlüsseltechnologien / Key Technologies
Band | Volume 16
ISBN 78-3-89336-641-5

JÜLICH
FORSCHUNGSZENTRUM